$\mathbf{J/\psi}$ production in $\mathbf{\sqrt{s_{NN}} = 5.02}$ TeV Pb–Pb collisions

Dissertation

zur Erlangung des Doktorgrades

der Naturwissenschaften

vorgelegt beim Fachbereich Physik

der Johann Wolfgang Goethe-Universität

in Frankfurt am Main

von

Pascal Raisig geb. Dillenseger

aus Frankfurt am Main

Frankfurt am Main 2019

(D 30)

Vom Fachbereich Physik der

Johann Wolfgang Goethe-Universität als Dissertation angenommen.

Dekan:

Prof. Dr. Michael Lang

Gutachter:

Prof. Dr. Harald Appelshäuser

Prof. Dr. Christoph Blume

Datum der Disputation:

Zusammenfassung

Eines der zentralen Ziele der aktuellen Forschung im Bereich der Kernphysik ist es, die physikalischen Gesetze für Materie unter extremen Bedingungen zu verstehen. Motiviert werden solche Untersuchungen von dem Interesse, Phänomene wie Neutronensterne, welche relevant für die Synthese von schweren Elementen wie Gold sind, oder den Urknall, also den Ursprungspunkt des Universums, besser zu verstehen. Während innerhalb von Neutronensternen vor allem eine sehr hohe baryonische Dichte (μ_b) herrscht, dominieren extrem hohe Temperaturen die Bedingungen kurz nach dem Urknall. Schwerionenkollisionen ermöglichen es, vergleichbare baryonische Dichten oder Temperaturen im Labor zu erzeugen. Der Large Hadron Collider (LHC), ein Teilchenbeschleuniger mit 27 km Umfang, betrieben vom Conseil Européen pour la Recherche Nucléaire (CERN), lässt Bleikerne bei zuvor unerreichten Schwerpunktsenergien kollidieren. Dabei werden in dem Kollisionsvolumen Temperaturen von etwa 300 MeV erreicht, was mehreren Terakelvin entspricht. Ausgehend von der Quantenchromodynamik (QCD) zur Beschreibung der starken Wechselwirkung folgt aus Gitterrechnungen, dass oberhalb einer kritischen Temperatur von $T_c \gtrsim 160$MeV ein Phasenübergang von hadronischer Materie in das sogenannte ***Quark-Gluon Plasma*** (QGP) stattfinden sollte. Entsprechend den kurz nach dem Urknall vorherrschenden Temperaturen sollte die existente Materie im Zustand eines QGPs gewesen sein. Um also unter anderem den Urknall besser verstehen zu können, ist es eine elementare Grundlage, das QGP und die physikalischen Gesetze, denen Materie im Zustand des QGP folgt, genauestens zu erforschen.

Vor etwas mehr als 30 Jahren veröffentlichten T. Matsui und H. Satz ihre Idee, dass die vorübergehende Existenz einer QGP-Phase die Produktion von J/ψ-Mesonen in Schwerionenkollisionen verstärkt unterdrückt gegenüber der Produktion ohne QGP Phase, also beispielsweise in Proton-Proton Kollisionen. Dieses Phänomen kann nach Matsui und Satz zum Existenznachweis eines Phasenübergangs zwischen hadronischer Phase und QGP verwendet werden, welcher zum damaligen Zeitpunkt experimentell noch nicht nachgewiesen war. Eine solche anormale Unterdrückung von J/ψ-Mesonen konnte dann in zentralen Pb−Pb Kollisionen am Super Proton Synchrotron (SPS) und in ebenfalls zentralen Au−Au Kollisionen am Relativistic Heavy-Ion Collider (RHIC) gemessen werden. Als physikalische Messgrößen, um eine solche Unterdrückung zu untersuchen, wird der sogenannte *nuclear modification factor* (R_{AA}) verwendet. Dieser spiegelt das Verhältnis zwischen der Produktion von J/ψ in Kern−Kern und in Nukleon−Nukleon Kollisionen wider, wobei die Produktion von J/ψ in Nukleon−Nukleon Kollisionen mit der geometrisch abgeschätzten mittleren Anzahl von Nukleon−Nukleon Kollisionen in den Kern−Kern Kollisionen skaliert wird.

Charm- Anti-Charm-Quark Paare werden selbst bei Kollisionsenergien, wie sie am LHC erzeugt werden, nur durch harte Interaktionen zu Beginn der Kollision erzeugt. Dabei ist, aufgrund der Partonen-Verteilung in den kollidierenden Protonen, der dominierende Prozess die Fusion von Gluonen. Der Ansatz von T. Matsui und H. Satz beruht auf zwei Besonderheiten der starken Wechselwirkung gegenüber den restlichen elementaren Wechselwirkungen. Zum einen treten keine freien Ladungen

der starken Wechselwirkung auf, da das Potential zwischen zwei stark wechselwirkenden Teilchen mit ihrem Abstand, im Gegensatz zu den Potentialen der anderen elementaren Kräfte, zunimmt. Dadurch unterliegen stark wechselwirkende Teilchen dem sogenannten *confinement*, das bedeutet, sie werden in nach außen gegenüber der starken Wechselwirkung neutrale Hadronen gebunden. In der QCD als beschreibende Theorie der starken Wechselwirkung gibt es drei Ladungszustände. Sie werden als sogenannten Farbladungen blau, grün und rot bezeichnet, dabei existiert zusätzlich zu jedem dieser Ladungszustände noch ein Antizustand. Ein farbneutraler Zustand wird entweder durch die Kombination aller drei verschiedenen Farbladungen, bzw. Antifarbladungen, zu einem gebunden Objekt, oder durch die Bindung eines Teilchens mit einem Antiteilchen, welches die entsprechende Antifarbe als Ladung trägt, gebildet. Zum anderen zeigt die starke Wechselwirkung eine Besonderheit, die unter anderem bei sehr hohen Temperaturen auftritt, also den Bedingungen, bei denen ein möglicher Phasenübergang von hadronischer Materie zum QGP stattfinden sollte. Sehr kurze Distanzen bzw. hohe Impulsüberträge führen, aufgrund der Form des Potentials und des Verlaufs der Kopplungskonstanten der QCD als Funktion des Impulsübertrags, bei Prozessen der starken Wechselwirkung zur sogenannten asymptotischen Freiheit, auch als *deconfinement* bezeichnet. Im QGP können sich Quarks und Gluonen quasi-frei bewegen, dadurch sollte nach Matsui und Satz das anziehende Potential zwischen Charm- und Anti-Charm-Quark von vielen leichten Quarks abgeschirmt werden. Dieser Prozess wird als *Debye-Screening* bezeichnet, welches dann verhindert, dass das Charm- und Anti-Charm-Quark sich zu einer J/ψ-Resonanz binden. Stattdessen kommt es im weiteren Verlauf der Kollision zu einer Bindung mit einem der zahlreich vorkommenden leichten Quarks, was dann zu der anormalen Unterdrückung führt. Wie bereits erwähnt, wurde eine solche anormale Unterdrückung der J/ψ-Produktion am SPS und am RHIC bei Schwerionenkollisionen mit Schwerpunktsenergien im maximal dreistelligen GeV Bereich gemessen.

Ungefähr zehn Jahre vor den ersten Schwerionenkollisionen am LHC wurde prognostiziert, dass bei Schwerpunktsenergien im TeV Bereich ein weiterer Prozess, welcher der anormalen Unterdrückung entgegen wirkt, einsetzt und in der J/ψ-Produktion bei LHC Energien eine relevante Rolle spielt. Durch die erhöhte Schwerpunktsenergie steigt die Produktionswahrscheinlichkeit für Charm-Quarks stark an, sodass die quasi-freien Charm-Quarks mit nicht verschwindender Wahrscheinlichkeit eine Bindung mit einem weiteren quasi-freien Charm-Quark anstatt eines leichten Quarks eingehen können. Somit wird die prinzipiell unterdrückte Produktion von J/ψ-Mesonen erhöht. Dabei wird von J/ψ *regeneration* durch sogenannte *(re)combination* gesprochen. Messungen der J/ψ-Produktion in Pb$-$Pb Kollisionen bei $\sqrt{s_{\mathrm{NN}}} = 2.76$ TeV konnten bestätigen, dass der *regeneration*-Prozess eine relevante Rolle oberhalb einer gewissen Schwerpunktsenergie spielt. Die unterschiedlichen Produktionsprozesse ergeben unterschiedliche Verteilungen der kinematischen Eigenschaften der produzierten J/ψ-Mesonen. Daher ermöglicht eine präzise Messung der kinematischen Eigenschaften detaillierte Rückschlüsse auf die J/ψ-Produktion und damit auf das Verhalten der starken Wechselwirkung unter extremen Bedingungen.

Mit dem *A Large Ion Collider Experiment (ALICE)* ist es möglich J/ψ-Mesonen im Zerfallskanal in Elektron-Positron Paare im mittleren Rapiditätsbereich ($|\eta| < 0.9$) selbst bei verschwindendem Transversalimpuls (p_{T}) zu rekonstruieren. ALICE wurde explizit für die Untersuchung von Schwerionenkollisionen am LHC und damit für die Erforschung des Quark-Gluon Plasma (QGP) entwickelt. Neben der Rekon-

struktion im dielektronischen Zerfallskanal können J/ψ, welche mit Vorwärts gerichteter Rapidität zerfallen, im dimyonischen Zerfallskanal rekonstruiert werden. Dort ermöglichen Absorber die Trennung der Myonen von anderen geladenen Teilchen. Die Selektion von Elektronen und Positronen bei mittlerer Rapidität erfolgt durch verschiedene Techniken zur Teilchenidentifizierung. Ein zentraler Detektor dabei ist die *Time Projection Chamber* (TPC). Ionisierende Strahlung deponiert abhängig von der Ladung und der Geschwindigkeit der Strahlung Energie im Gasvolumen der TPC, dabei werden die Verteilungen der deponierten Energie von der Bethe-Bloch Gleichung beschrieben. Zusätzliche Informationen zur Identifizierung von Elektronen können der *Transition Radiation Detector* (TRD) und der *Time-Of-Flight detector* (TOF) liefern. Zur Rekonstruktion der Trajektorien der aus dem Kollisionsvolumen kommenden Teilchen wird neben der TPC noch das *Inner Tracking System* (ITS) verwendet. Für die Selektion von Elektronen aus J/$\psi \to e^+e^-$ Zerfällen werden neben der Teilchenidentifizierung auch zusätzlich topologische Kriterien verwendet, diese sortieren Elektronen aus anderen Zerfällen aus. Aufgrund der kurzen Lebensdauer von J/ψ-Mesonen müssen die Spuren der zugehörigen Elektronen ihren Ursprung in direkter Umgebung des Kollisionsvertex haben. Dementsprechend werden alle Spuren, deren Ursprung nicht in der Nähe des Kollisionsvertex liegt, aussortiert. Aus dem Ensemble der selektierten Elektron- und Positronkandidaten wird zur Rekonstruktion der J/ψ-Resonanz dann ein sogenanntes *opposite sign* Spektrum, also ein Spektrum, in dem alle Kandidaten mit entgegengesetzter elektrischer Ladung gepaart werden, erstellt. Auf der Basis dieser Methode können dann verschiedenste differenzielle Analysen der J/ψ-Produktion durchgeführt werden.

Eine solche differenzielle Analyse der J/ψ-Produktion ist die Messung des elliptischen Flusses ($v_2^{J/\psi}$) der produzierten J/ψ. Eine präzise Bestimmung des elliptischen Flusses von J/ψ ermöglicht Rückschlüsse auf die Zusammensetzung aus direkten und regenerierten J/ψ der gesamten produzierten J/ψ. Durch die Abhängigkeit vom kollektiven Verhalten des Mediums sind darüber hinaus auch Rückschlüsse auf die Kopplung der starken Wechselwirkung im QGP möglich. Solche c$\bar{\text{c}}$-Paare, die kurz nach der Erzeugung in einem harten Prozess die Bindung zu einer J/ψ-Resonanz eingehen und das Kollisionsvolumen weitgehend ohne Interaktion verlassen, werden als direkte J/ψ bezeichnet. Solche hingegen, deren Farbladung gegenüber dem initialen Partner zunächst im QGP abgeschirmt wird und die erst im weiteren Verlauf ein beliebiges (Anti-)Charm-Quark als Partner finden, werden dem sogenannten Regenerationsprozess zugeordnet. Charm- und Anti-Charm-Quarks von regenerierten J/ψ unterliegen vor der Bindung zur Resonanz vielfachen Wechselwirkungen mit dem QGP. Daraus folgt, dass ihre kinematischen Verteilungen im Gegensatz zu direkten J/ψ auch stark von kollektiven Effekten, wie dem elliptischen Fluss, beeinflusst werden. Allgemein entsteht der elliptische Fluss in Schwerionenkollisionen am LHC durch azimutale Asymmetrien des Kollisionsvolumens. Mit einer hydrodynamischen Beschreibung kann erklärt werden, wie die anfänglich räumlichen Asymmetrien sich in Asymmetrien des Phasenraums übertragen. Durch die zwangsläufige Interaktion von regenerierten J/ψ mit dem Medium müssen diese auch vom kollektiven elliptischen Fluss beeinflusst werden.

Die in dieser Arbeit vorgestellte Messung vom elliptischen Fluss von J/ψ, gemessen im dielektronischen Zerfallskanal in Pb$-$Pb Kollisionen mit einer Schwerpunktsenergie von $\sqrt{s_{\text{NN}}} = 5.02$ TeV, basiert auf der Bestimmung der Korrelation zwischen dem azimutalen Raumwinkel ($\Psi_{\text{ep.}}$) der Ereignisebene und der azimutalen Verteilung der produzierten J/ψ. Die Ereignisebene wird dabei aufgespannt durch die Strahlachse und die kurze Achse der Ellipse, die das Kollisionsvolumen beschreibt.

Bestimmt wird $\Psi_{\text{ep.}}$ mit Hilfe der allgemeinen Verteilung der Teilchen entlang des azimutalen Raumwinkels. Für die Messung von $v_2^{J/\psi}$ wurden zwei Methoden betrachtet und verglichen. Zum einen wurde die Anzahl der J/ψ in verschiedenen Intervallen des azimutalen Raumwinkels bestimmt und daraus $v_2^{J/\psi}$ errechnet, zum anderen wurde die mittlere Differenz zwischen $\Psi_{\text{ep.}}$ und dem azimutalen Raumwinkel der einzelnen J/ψ ($\varphi_{J/\psi}$) als Grundlage zur Ermittlung von $v_2^{J/\psi}$ verwendet.

Im Rahmen der vorliegenden Dissertation konnte zum ersten Mal in Pb−Pb Kollisionen bei $\sqrt{s_{\text{NN}}} = 5.02$ TeV ein Hinweis auf die Existenz von elliptischem Fluss von J/ψ ($v_2^{J/\psi}$) im mittleren Rapiditätsbereich beobachtet werden. Dabei wurde $v_2^{J/\psi}$ in drei verschiedenen Intervallen des Transversalimpulses (p_{T}) gemessen. Transportmodelle zeigen für J/ψ, die per Regenerationsprozess erzeugt werden, eine Anhäufung bei Transversalimpulsen um die 3 GeV/c. Dementsprechend wird der signifikanteste Wert für ein positives $v_2^{J/\psi}$ ebenfalls in diesem Bereich erwartet. Die Messung in dem diesen Bereich einschliessenden Intervall bestätigt diese Erwartung und weist im mittleren Rapiditätsbereich den signifikantesten Unterschied zwischen $v_2^{J/\psi}$ und 0 auf. Insgesamt wurde im Rahmen der Unsicherheiten eine gute Übereinstimmung zwischen der Vorhersage für den elliptischen Fluss des Transportmodels von Du und Rapp und der Messung beobachtet. Für die Übereinstimmung spielt die Komponente der regenerierten J/ψ im Transportmodell eine entscheidende Rolle, wodurch der Vergleich als weitere Bestätigung für die wichtige Rolle des Regenerationsprozess in der J/ψ-Produktion am LHC gesehen werden kann. Unglücklicherweise beschränken die statistischen Ungenauigkeiten der Messung die Möglichkeiten weitere Konklusionen im Vergleich mit den Modellen zu schließen. Wie wichtig weitere Messungen von $v_2^{J/\psi}$ in kleineren Intervallen des Transversalimpulses und mit erhöhter statistischer Präzision im mittleren Rapiditätsbereich ist, zeigt die Abweichung zwischen den Vorhersagen der Transportmodelle und der Messung in Vorwärtsrichtung bei Transversalimpulsen von $p_{\text{T}} \approx 6$ GeV/c. Der gemessene Wert für $v_2^{J/\psi}$ übersteigt hier klar die vorhergesagten Werte, was eventuell sogar auf einen fehlenden Produktionsprozess in den Modellen hinweisen könnte.

Neben weiteren Messperioden bei gleicher Kollisionsenergie könnten Verbesserungen in der Analyse der gemessenen Daten helfen, die statistischen Ungenauigkeiten zu reduzieren. Eine solche Option zur möglichen Reduktion statistischer Ungenauigkeiten bietet die Hinzunahme des Übergangsstrahlungsdetektors (TRD) von ALICE in das Schema zur Elektronen Selektion. Basierend auf dem Prinzip, dass geladene Teilchen beim Passieren von Übergängen zwischen Materialien mit unterschiedlicher elektrischer Permittivität mit von ihrer Geschwindigkeit abhängender Wahrscheinlichkeit sogenannte Übergangsstrahlung erzeugen, wurde der ALICE TRD unter anderem für die Trennung von Elektronen und Pionen mit Impulsen oberhalb von 3 GeV/c entwickelt. Im Frühjahr 2015 konnte der TRD vollständig installiert werden, sodass der komplette azimutale Raumwinkel und gleichzeitig der Pseudorapiditätsbereich $\eta < |0.84|$ abgedeckt wird. Vorherige Studien auf Basis von Pb−Pb Kollisionen bei $\sqrt{s_{\text{NN}}} = 2.76$ TeV mit noch unvollständigem TRD Detektor deuteten bereits an, dass die Ergänzung des Schemas zur Elektronen Selektion mit Informationen vom TRD das Potential hat, die Signifikanz von J/ψ-Messungen zu erhöhen.

Bisher basierte standardmäßig das verwendete Schema zur Identifizierung von Elektronen auf der Messung des Energieverlusts von Teilchen im Gasvolumen der Spurendriftkammer (TPC). Hierbei folgt der spezifische Energieverlust der Bethe-Bloch Funktion und ist von der Teilchengeschwindigkeit sowie der elektrischen Ladung abhängig. In Kombination mit der Messung des Teilchenimpulses ermöglicht

die Messung des spezifischen Energieverlusts also die Zuordnung von Teilchensorten zu Teilchenspuren. Allerdings beginnt der Verlauf der Bethe-Bloch Funktion bei Teilchengeschwindigkeiten von $\beta\gamma \approx 10^2 - 10^3$ zu saturieren und selbst große Variationen in der Geschwindigkeit führen lediglich zu marginalen Unterschieden des Energieverlusts. Dies bedeutet, dass in den relevanten Impulsbereichen mit steigendem Impuls vor allem die Trennung von Elektronen und Pionen auf Basis des spezifischen Energieverlusts in der TPC schwieriger wird. Während sich Elektronen sogar bei Impulsen unterhalb der durch die Kinematik eines $J/\psi \to e^+e^-$ Zerfalls vorgegebenen Untergrenzen bereits im saturierenden Bereich befinden, setzt für Pionen ab circa 0,3 GeV/c der *relativistic rise* ein, sodass oberhalb von 2-3 GeV/c ein relevanter überlapp des spezifischen Energieverlusts für Elektronen und Pionen entsteht, welcher die Selektion von Elektronen erschwert. Da das gesamte Spektrum von Teilchen erheblich mehr Pionen als Elektronen beinhaltet, müssen Teilchen, die nicht eindeutig als Elektron oder Pion identifiziert werden können, also solche aus dem zuvor erwähnten Überlappbereich, aus der Messung ausgeschlossen werden, um eine zu große Kontamination durch Pionen zu verhindern. Dadurch wird allerdings natürlich auch eine relevante Anzahl an Elektronen aussortiert. Die Messungen des TRD bieten weitere Informationen, um die Entscheidungsfindung bezüglich der Teilchensorte in diesem Impulsbereich zu verbessern. Um die vom TRD zur Verfügung stehenden Informationen optimal zu nutzen, wurde ein Konzept entwickelt, welches die Informationen vor allem in den kritischen Impulsbereichen der TPC anwendet. Prinzipiell basiert das Konzept zunächst auf dem Standardschema der Teilchenidentifizierung mit der TPC. Teilchenspuren, die von der TPC nicht eindeutig als Elektron bzw. Pion identifiziert werden können, werden mit Hilfe der Informationen vom TRD neu bewertet. Diese Erweiterung der Teilchenidentifizierung mit den TRD Informationen beinhaltet den großen Vorteil, dass kein Elektron des Standardschemas verloren geht. Es könnte somit nur dann zu einer schlechteren Signal-Extraktion führen, wenn signifikant mehr Hintergrund, vor allem durch vom TRD fälschlicherweise als Elektron identifizierte Pionen, dem Dielektronen-Spektrum hinzugefügt würden. Zu diesem Ansatz wurde im Rahmen dieser Arbeit eine Studie durchgeführt, welche die mögliche Verbesserung der J/ψ Rekonstruktion durch den Einsatz des TRD beleuchtet.

Zunächst wurde die allgemeine Akzeptanz von Teilchen im TRD untersucht und dann verknüpft mit den korrelierten Informationen zur Teilchensorte. Daraus lässt sich zur Evaluation der Fähigkeiten des TRD ableiten, wieviele Elektronen mit dem untersuchten neuen Konzept gewonnen werden können und in welchen Impulsbereichen diese liegen. Dabei ergibt sich das erwartete Verhalten, dass vor allem mit steigendem Impuls Elektronen vor dem Ausschluss bewahrt werden können. Im weiteren Verlauf der Studie wurde untersucht, inwiefern die durch den TRD ergänzten Elektronen die gemessene Anzahl an Signal- und Hintergrundpaaren und die daraus folgende Signifikanz der J/ψ-Resonanz beeinflussen. Dabei ergab sich, dass bei Betrachtung der Signifikanz sowohl als Funktion des Transversalimpulses als auch der Kollisionszentralität in nahezu allen p_{T}- und Zentralitätsintervallen eine Steigerung selbiger durch Hinzunahme des TRD erreicht werden konnte. Um letztendlich den Gewinn an Präzision durch den TRD benennen zu können, wird die Messung von $R_{\mathrm{AA}}^{J/\psi}$ mit und ohne TRD verglichen. Dazu wurde mit Hilfe von Monte Carlo Simulationen eine vollständige Korrektur der Messung des Signals als Funktion von Transversalimpuls und Rapidität durchgeführt, nachdem zuvor überprüft wurde, dass die Simulationen die durch die Hinzunahme des TRDs gewonnenen Elektronen korrekt abbilden. Detaillierte Vergleiche des Verhaltens der Spuren im TRD in Si-

mulationen und in Daten zeigen Abweichungen, beispielsweise bei der Anzahl der Lagen des TRD, die Signale einer Spur zuordnen können. Im Rahmen der statistischen Unsicherheiten und im Vergleich mit den Abweichungen des Standardschemas zwischen Daten und Simulationen ist das Verhalten der gewonnenen Elektronen als Funktion des Impulses in den Simulationen gut repräsentiert. Bei der Bestimmung von Akzeptanz und Effizienz ($\mathcal{A} \times \epsilon$) der Messung können die Beobachtungen aus der Analyse der Signifikanzen der J/ψ-Resonanz weiter bestätigt werden. Der ermittelte Korrektur-Faktor $(\mathcal{A} \times \epsilon)^{-1}$ ist mit dem TRD kleiner als ohne, es werden also auch in der Simulation mehr J/ψ mit dem TRD rekonstruiert als ohne. Auf der Grundlage der korrigierten J/ψ-Spektren wird dann $R_{\mathrm{AA}}^{\mathrm{J}/\psi}$ als Funktion der mittleren Anzahl der Nukleonen ($\langle N_{\mathrm{part}} \rangle$), welche an der Kollision teilgenommen haben, berechnet. Die Ergebnisse mit und ohne TRD sind im Rahmen der statistischen Unsicherheiten in guter Übereinstimmung, es kann also kein direkter systematischer Einfluss des TRD beobachtet werden. Im Vergleich der statistischen Unsicherheiten der Messung ergibt sich eine erhöhte Präzision durch die zusätzliche Verwendung der TRD-Informationen in jedem $\langle N_{\mathrm{part}} \rangle$-Intervall.

Zusammenfassend konnte im Rahmen dieser Arbeit ein erster Hinweis auf einen positiven elliptischen Fluss von J/ψ aus Pb−Pb Kollisionen bei einer Schwerpunktsenergie von $\sqrt{s_{\mathrm{NN}}} = 5.02$ TeV im mittleren Rapiditätsbereich beobachtet werden. Darüber hinaus konnte in einer ersten Studie gezeigt werden, dass der 2015 fertiggestellte ALICE TRD in der Lage ist die Selektion von Elektronen für die Analyse zu verbessern, sodass die statistische Präzision der Messung von $R_{\mathrm{AA}}^{\mathrm{J}/\psi}$ im J/$\psi \rightarrow e^+e^-$ Zerfallskanal unter zur Hilfenahme des TRD erhöht werden kann.

Contents

1 Introduction

In the Nature journal Vol. 127 from 1931, Lemaître published an article with the title: "The Beginning of the World from the Point of View of Quantum Theory.", which today is known as the foundation of the "Big Bang theory" [2]. In his article Lemaître proposes the idea that at every point of time the available amount of energy is distributed to all available quantum states. Within his approach the amount of total energy is constant while the number of quantum states starts with a unique quantum also quoted as "primeval atom" at the beginning of the universe and increases afterwards. 17 years later Fred Hoyle, who himself set up the contradictive "steady state theory", established the name Big Bang theory for Lemaîtres approach in a radio program [3].

Theories about the beginning of the universe were already developed far before Lemaître published his article, some already in the seventh and sixth century B.C. [4]. However the quest to understand the birth of the universe based on the Big Bang theory has an unprecedented large impact on scientific and philosophic researches of mankind in the 21st century. In 1984 the idea to build the Large Hadron Collider (LHC) at the Conseil Européen pour la Recherche Nucléaire (CERN) was put forward at a workshop in Lausanne, eight years later the "Evian meeting" took place, which had the topic: "Towards the LHC Experimental Programme." where the physics cases of the future LHC were presented [5]. Another 18 years later the first Pb−Pb collisions in the TeV collision-energy regime were induced at the crossing points of the LHC, providing scientists with data on matter under conditions closest to those from ***the Big Bang*** ever created by mankind [6]. One central goal of the analyses of this data is to obtain knowledge about the laws of physics under these extreme conditions, represented by the interactions of elementary particles. The existing knowledge about the elementary forces and particles is summarized in the standard model of particle physics, where the strong force has the largest impact on elementary particle interactions and the way matter is composed. In the 20th century ***Quantum Chromodynamics (QCD)*** were developed as a description for the strong force [7]. Similar to phase diagrams of macroscopic matter a QCD phase diagram that describes the state of elementary matter depending on temperature and the density matter is being explored. A sketch of the diagram is shown in figure 1.1 with the density of matter on the x-axis and the temperature on the y-axis, two quantities which, within a thermodynamical approach, in combination represent the energy density. In the diagram, the state of the matter that surrounds us in our daily life is found at low temperatures, marked as nuclear matter. With an increment of the energy density, a change of the state of matter is expected. While increased net baryonic densities lead towards the state of matter in neutron stars, a state compatible to the one of the early universe is expected at high temperatures. Thus, the exploration of the QCD phase diagram with experimental data from heavy-ion collisions at the LHC creating extremely hot temperatures will allow to further understand ***the beginning of the world***.

To further motivate the research of this thesis in detail and connect it to the investigation of the Big Bang, a small introduction to the standard model of particle

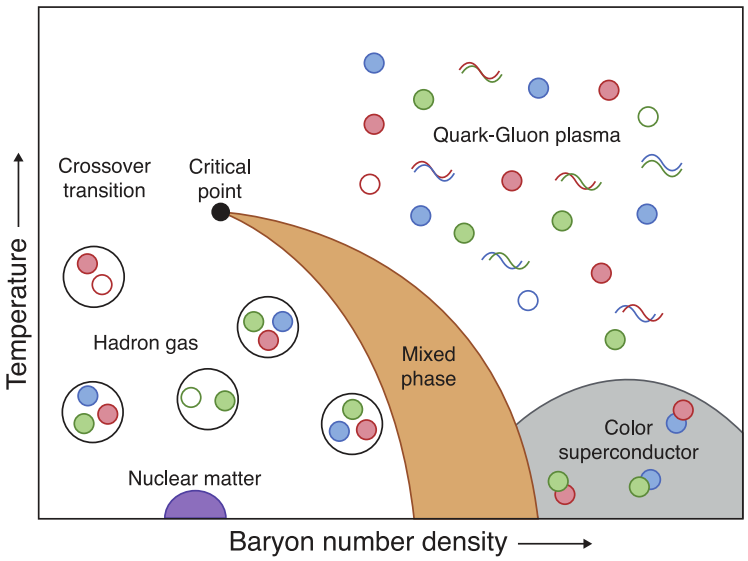

Figure 1.1: Sketch of the phase diagram of QCD matter [8].

physics and the theory of QCD will be given in the following. The focus of this introduction will be on the peculiarities of matter in the hot and dense areas of the QCD phase diagram.

1.1 Standard model of particle physics

The standard model of particle physics summarizes the discoveries and developments of the last decades in the field of elementary particles and forces. In the following, its basic principles will be described as baseline for the research of this thesis. Further details and information on the standard model can be found in a wide range of literature, for example in [9, 10].

Particles are divided into two categories according to their spin. Particles with half-integral spin are called fermions and those with an integral spin are called bosons. Fermions and bosons behave differently with respect to the spin-statistics theorem, which describes the symmetry of the wave function under interchange of two identical particles. Fermions are subject to the Fermi-Dirac statistics, while bosons are subject to the Bose-Einstein statistics. Following this observation, Pauli formulated his principle, which states that it is not possible that two or more fermions exist in the same quantum state, while for bosons this does not apply.

One keystone of the concept of the standard model are the twelve elementary particles, all of them fermions, i.e. six leptons (ℓ) and six quarks (q, Q). In addition, the quarks and leptons are sorted into three generations, each generation contains a quark with $q = \frac{2}{3}\ e$ and $q = -\frac{1}{3}\ e$ electrical charge, a neutrino and a lepton with $q = -e$ as electrical charge. Measurements observe a clear mass ordering from the first up to the third generation, only for the neutrinos this still has to be verified since the mass is not yet measured. A summary of the particles can be found in table 1.1. Every elementary particle has a complementary antiparticle with similar mass and spin, but opposite electrical charge and magnetic moment relative to the direction of the spin. In the standard model, all matter is composed of elementary particles, a particle consisting of quarks is called ***hadron***. Hadrons are distinguished by their baryon number (B), every quark (antiquark) has $B = \frac{1}{3}$ ($B = -\frac{1}{3}$). Those

I	II	III	Charge
	Quarks		
up	**charm**	**top**	
$m = 2.2^{+0.5}_{-0.4}$ MeV/c^2	$m = 1.275^{+0.025}_{-0.035}$ GeV/c^2	$m = 173.0^{+0.4}_{-0.4}$ GeV/c^2	$+\frac{2}{3}e$
down	**strange**	**bottom**	
$m = 4.7^{+0.5}_{-0.3}$ MeV/c^2	$m = 95^{+9}_{-3}$ MeV/c^2	$m = 4.18^{+0.04}_{-0.03}$ GeV/c^2	$-\frac{1}{3}e$
	Leptons		
e	$\boldsymbol{\mu}$	$\boldsymbol{\tau}$	
$m = 510.99$ keV/c^2	$m = 105.65$ MeV/c^2	$m = 1776.86 \pm 0.12$ MeV/c^2	$-e$
$\boldsymbol{\nu_e}$	$\boldsymbol{\nu_\mu}$	$\boldsymbol{\nu_\tau}$	
$m > 0$	$m > 0$	$m > 0$	0

Table 1.1: Elementary fermions (quarks and leptons) of the standard model [11].

hadrons with positive (negative) integer B are called ***baryons*** (antibaryons) and states with $B = 0$ are called ***mesons***.

Four elementary forces build the second keystone of the standard model. Interactions between particles are described by fields representing the forces with associated exchange particles, all of them bosons. In table 1.2 the forces and their quanta are listed. For interactions of elementary particles, the strong force is the most relevant force, with QCD (see section 1.1.2) giving the theoretical description. However, the strong force does not interact with all elementary particles, only quarks and gluons are subject to fields of the strong force. Thus, the electromagnetic force which interacts with all electrically charged particles, and the weak force which interacts with all particles also play an important role. Note that the $W^{\pm}$ and Z bosons are liste without a value for their parity, this results from the fact they are not an eigenstate of the parity operator. On the scale of elementary particle interactions gravitation has no significant influence.

1.1.1 Conservation laws

For the understanding of particle physics not only the forces and particles themselves are important, also the conservation laws need to be well understood. Reduced to its bottom line, Noether's theorem states that every fundamental symmetry leads to a corresponding conservation law [12]. Within particle physics and especially the standard model this means that certain observables are invariant. However, not all conservation laws apply similar to the different forces. In the following, those conservation laws linked to particle physics and relevant to understand the research of this thesis will be introduced.

Force	Exchange boson	J^P	m
strong	gluon, g	1^-	0
electromagnetic	photon, γ	1^-	0
weak	$W^\pm$	1	80.379 ± 0.012 GeV/c^2
	Z	1	91.1876 ± 0.0021 GeV/c^2
gravity	graviton	2^+	$< 6 \cdot 10^{-32}$ eV/c^2

Table 1.2: Elementary forces and their associated exchange particles [10, 11].

- Baryon conservation: The baryon number is invariant, thus the net amount of baryons, i.e. $n_\mathrm{B} - n_{\bar{\mathrm{B}}}$, before and after an interaction has to be the same.
- Flavor conservation: The quark flavor is invariant under the strong and electromagnetic force, however charged currents of the weak force, i.e. interactions where a $W^\pm$ is exchanged, change the flavor.
- Lepton conservation: The lepton number is invariant, within strong or electromagnetic interactions even the generation-wise lepton number is constant, e.g. $\mu \to e$ is not possible but $\mu \to e + \bar{\nu_e} + \nu_\mu$ is. Again charged weak currents are an exception and change lepton generations.

1.1.2 Quantum Chromodynamics

Based on the approach of the Quantum Electrodynamics (QED), which describes the electromagnetic force, Quantum Chromodynamics (QCD) was developed to describe the strong force. Analogous to the electrical charge in QED is the color charge for QCD. However, in contrast to the only positive or negative charge state in the QED, there are three color charge states (blue, green, red) and additionally the corresponding anticolor states. Phenomenologically the color charge was needed to describe the Δ^{++}, $|u\uparrow,\ u\uparrow,\ u\uparrow\rangle$ and the Δ^-, $|d\uparrow,\ d\uparrow,\ d\uparrow\rangle$ [13] with the quark model approach. Without additional degrees of freedom it would violate the Pauli-principle, the color charge solves this problem. A nice review of the historical development of the concept of color can be found here [14]. Color-charged objects are subject to the strong force, the potential between a quark and an antiquark follows this equation:

$$V_{\mathrm{q\bar{q}}} = -\frac{4}{3}\frac{\alpha_s}{r} + kr, \tag{1.1}$$

with r as the distance of the objects, α_s as the strong coupling and k in the order of magnitude of 1 GeV fm^{-1}. The first term is compatible with the Coulomb-potential from QED, but the second term shows a first peculiarity of the QCD. With increasing distance, the energy stored in the potential grows until it reaches the limit to create a new quark-antiquark pair. As a result of the shape of the potential, no free color-charged states can exist. This phenomenon is called ***confinement*** and up to now confirmed by experiment where no free color-charged objects have yet been observed. Another peculiarity of QCD is its exchange boson, the gluon. Contrary

to the photon, which has zero electrical charge, the gluon itself is color-charged and thus interacts with strong fields. This has to be taken into account when calculating the Lagrangian of the QCD:

$$\mathcal{L}_{\mathrm{QCD}} = -\frac{1}{4}\sum_{a=1}^{8} G^{a}_{\mu\nu} G^{a\mu\nu} + \sum_{f=1}^{6} [\bar{\mathbf{q}}_f \mathrm{i}\gamma^{\mu}(\delta_{\mu} + \mathrm{i}g\mathbf{G}_{\mu})\mathbf{q}_f - m_f \bar{\mathbf{q}}_f \mathbf{q}_f] \tag{1.2}$$

A consequence of the gluon self-interaction is a feature of the strong force which is quite important for hot and dense matter, the so-called ***asymptotic freedom***. With increasing momentum transfer ($Q \propto \frac{1}{r}$), the coupling in strong interactions decreases towards a state of quasi free color-charged objects. In figure 1.2 the course

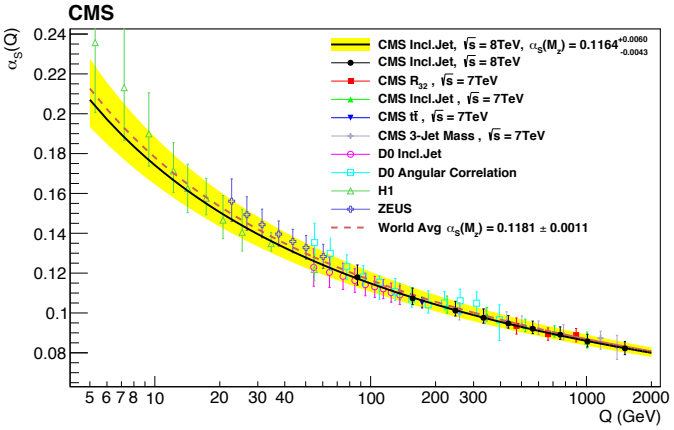

Figure 1.2: Strong coupling (α_s) displayed as function of the momentum transfer (Q) of the interaction. The markers and lines show results of experimental measurements combined with calculations from QCD perturbation theory. The red-dashed line represents the world average, which predicts a value of $\alpha_s(m_{Z^0}) = 0.1181 \pm 0.0011$ [15].4

of strong coupling (α_s) as function of Q is shown, a clear decrease of α_s with increase of Q is visible and underlined by the nice agreement of the data with QCD predictions. The dependence of α_s on the distance of the color-charged objects also translates into a dependence on the temperature and the density of QCD matter and thus an alteration of those quantities can potentially lead to a phase transition in the phase diagram of QCD matter (see figure 1.1). In the hot and dense region of heavy-ion collisions and the Big Bang, a phase transition to a state called ***Quark-Gluon Plasma (QGP)*** is expected. Clear hints for the existence of such a state have been observed [16, 17]. The QGP will be discussed in the next section (1.2).

1.2 Quark-Gluon Plasma

As introduced in section 1.1.2, the QGP is a state of matter reached under hot and dense conditions. Clear changes in the behavior of strongly interacting matter have been observed by several experiments [16, 17]. The quest for the next generation is a detailed analysis of the QGP and a fully quantified picture of the QCD phase diagram (figure 1.1). This means, understanding the Equation of State (EoS) in dependence of temperature (T) and net-baryon density (μ_b), based on experimental measurements. The predicted phases and the differences of the transitions are

sketched in figure 1.1. While at low T and high μ_b a color superconductor state might be reached [18], above a minimum temperature and sufficiently high energy density a transition into a QGP phase is expected, and for high temperatures this was already observed. However, the type of transition into the QGP seems to depend on the combination of T and μ_b during the phase transition. For μ_b larger than the one of a conjectured critical point (CP), theory predicts a first order phase transition, for μ_b smaller μ_b^{CP} a crossover-like transition is expected [19].

The tool to investigate the phase diagram of QCD are heavy-ion collisions. Varying the collision energies allows to explore different regions of T and μ_b. In the following section (1.3) the physics of heavy-ion collisions will be introduced, with a focus on collisions created by the LHC at CERN, which is currently reaching the highest collision energies and thus the hottest conditions [20].

1.3 Hot and dense matter from heavy-ion collisions

Heavy-ion collisions provide data to study the behavior of hot and dense matter in a rather well controlled environment. Figure 1.3 shows a sketch of the space-time

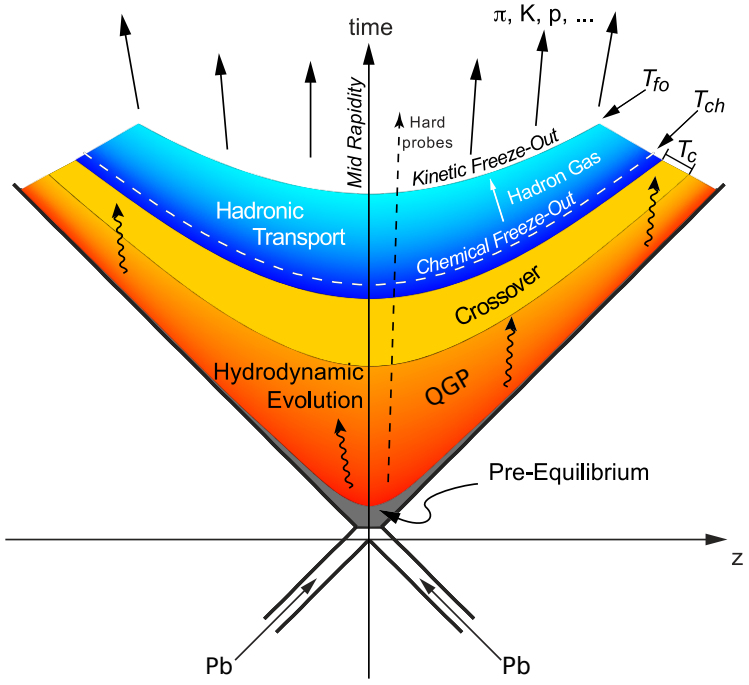

Figure 1.3: Space-time evolution of a high-energy heavy-ion collision. After a pre-equilibrium phase a QGP is established, followed by a crossover phase transition into a hadron gas at $T \approx T_{\mathrm{c}}$. When $T = T_{\mathrm{ch}}$ is reached, the chemical freeze-out takes place and the kinetic freeze-out at $T = T_{\mathrm{fo}}$. Figure adopted from [21].

evolution of a heavy-ion collision with a sufficiently high energy density for a phase transition into a QGP phase. On the x-axis is the space evolution along the beam-axis and on the y-axis the time. Less than one fm/c after the initial scatterings, the formation of a QGP takes place. The so-called fireball naturally starts then to expand and cool down until the critical temperature (T_{c}) for the phase transition into a hadron gas is reached. During the phase transition, which is observed as crossover transition under the conditions at the LHC, confinement is fully restored. Within the hadron gas, inelastic interactions are still able to modify the particle

composition. Due to the further decreasing temperature, those interactions vanish. The moment where no more inelastic interactions take place is called chemical freeze-out, and correspondingly the temperature at this point is the chemical freeze-out temperature (T_{ch}). Finally, the kinetic freeze-out is reached when no more elastic interactions between particles from the collision happen, and hence their kinematic description is frozen. The temperature correlated to this point of the collision is the so-called kinetic freeze-out temperature (T_{fo}). Depicted in figure 1.4 are T_{ch} and

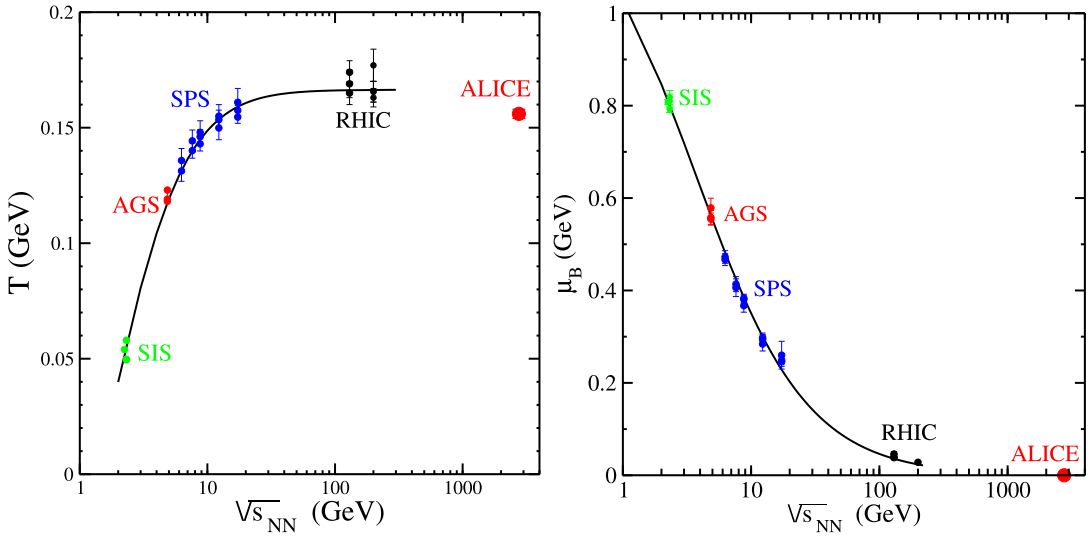

Figure 1.4: Temperature (T) (left) and net-baryon density (μ_b) (right) at the chemical freeze-out as function of the collision energy ($\sqrt{s_{\mathrm{NN}}}$), extracted from particle yields using the thermal-statistical model [22].

μ_b (also at the chemical freeze-out) as function of the collision energy ($\sqrt{s_{\mathrm{NN}}}$) as estimated by the thermal-statistical model from particle yield measurements [22]. The fact that varying $\sqrt{s_{\mathrm{NN}}}$ leads to different T_{ch} and μ_b allows the exploration of the phase diagram with heavy-ion collisions. As mentioned before, the LHC provides collisions in the TeV regime, reaching the highest temperatures ever created by mankind and thus creates the conditions closest to those of the early universe. In figure 1.4 $\sqrt{s_{\mathrm{NN}}} = 2.76$ TeV Pb−Pb collisions at the LHC are represented by the red markers labeled with ALICE, above Super Proton Synchrotron (SPS) collision energies a saturation of T_{ch} around 150-160 MeV is visible (left plot). With increasing $\sqrt{s_{\mathrm{NN}}}$, a decrease of μ_b towards zero is observed (right plot), which has its reason in the fast passing of the ions, very pictorially spoken all nucleons from the colliding ions have left the building when the chemical freeze-out takes place.

Providing heavy-ion collisions for experiments itself is similarly complicated like the research with the experiments. In section 3.1 a review of the LHC as part of the experimental setup for the research of this thesis is given.

1.3.1 Signatures of the quark-gluon plasma in heavy-ion collisions

The basic principle of a signature is a unique behavior under certain circumstances, thus an observable for a QGP signature has to show a different behavior in measurements where a QGP phase is expected compared to those where no QGP phase is expected. As reference for a hadron gas phase, nucleon-nucleon (pp) collisions are utilized. The results of those measurements can for example then be scaled via

the Glauber model to nucleus-nucleus (A−A) collisions, as if they would act like multiples of independent pp collisions [23]. Another step to investigate the hadron gas are nucleon-nucleus (p−A) collisions. In comparison with pp measurements, they should be able to highlight the effects of Cold-Nuclear-Matter (CNM), e.g. (anti-)shadowing due to modified Parton Distribution Functions (PDFs) in nuclear matter [24]. Finally, since a phase transition into an equilibrated QGP phase requires a certain volume at sufficiently high energy densities, also peripheral A−A collisions with only a small overlap of the nuclei provide a possibility to measure observables in a non-QGP phase. Several signatures for the existence of a QGP phase in A−A collisions have been developed in the past. A detailed discussion of signatures provided by charmonium measurements will be given in chapter 2, while a more complete review of the QGP and its signatures can for example be found in [25].

1.4 Outline of this work

As introduction for this thesis chapter 1 is supposed to give a short overview over the big picture of the research on the early universe done with heavy-ion collision, of which the analysis presented in this thesis is a part. The next chapter (2) introduces charmonia themselves, how they can be used to investigate the QGP and what we have learned from charmonium measurements so far. In chapter 3 the experimental apparatus is described, including the accelerator complex providing the heavy-ion collisions, the A Large Ion Collider Experiment (ALICE) and the framework and data sample used for the analysis. The main analysis of this work is the measurement of the elliptic flow of the J/ψ, it will be discussed in chapter 5.With statistical errors always leaving room for improvement in measurements of rare probes like charmonia, a new Particle IDentification (PID) scheme also utilizing the information from the ALICE Transition Radiation Detector (TRD) was developed and tested. This approach and its results will be reviewed in chapter 6. Finally, a summary and outlook in chapter 7 will conclude the thesis.

2 Charmonia and the quark-gluon plasma

In this chapter first of all the elementary properties of charmonia and how they are produced on the quark level will be described. Then the initial idea of Matsui and Satz, that a charmonium suppression in heavy-ion collisions is a signature for a QGP phase formation, will be introduced, followed by a review of the current status of the research on charmonia as observables in heavy-ion collisions.

2.1 Elementary properties and production of charmonia

Mesons built from heavy quark-antiquark pairs, where quark and antiquark have the same flavor, are called ***quarkonia***, i.e. $\mathbf{c\bar{c}} \longleftrightarrow$ ***charmonia***, $\mathrm{b\bar{b}} \longleftrightarrow$ bottomonia. With a typical formation time around 0.5 fm/c for quarkonia, top-quarks decay too fast to form bound states and thus "topomonia" do not exist. Charmonia are also called ***hidden/closed charm*** mesons since their net charm content is zero. As complementing counterpart, mesons with one (anti)charm quark and a light quark (u, d) are called ***open charm*** mesons. In 1974 the research group of Sam Ting and at the same time the group of Burton Richter reported on the measurement of a narrow resonance state with a mass of 3.1 GeV/c^2 [27, 28] named "J" by the group of Ting and "ψ" by the group of Richter. Since it turned out that Ting and Richter discovered the same state it is now called J/ψ. In table 2.1 the quantum numbers, Branching Ratios (B.R.s) and the feed-down fraction to the J/ψ are summarized for the J/ψ itself and those charmonia with a decay into a J/ψ. As a result of the fact that $m_{\mathrm{J}/\psi} < 2\ m_{\mathrm{D-meson}}$ the strong decay mode is suppressed due to the OZI-rule [30]. Hence, the J/ψ has a quite small resonance width and thus a long lifetime in comparison to other resonances. Not only the small width is induced by this fact, also the large B.R. of the leptonic decay channel is a result of the "forbidden" strong decay.

In high-energy hadron collisions, there are two leading processes for the heavy quark production. In figure 2.1, examples for these processes are depicted as Feynman diagrams. The left diagram shows a gluon fusion process and the right diagram

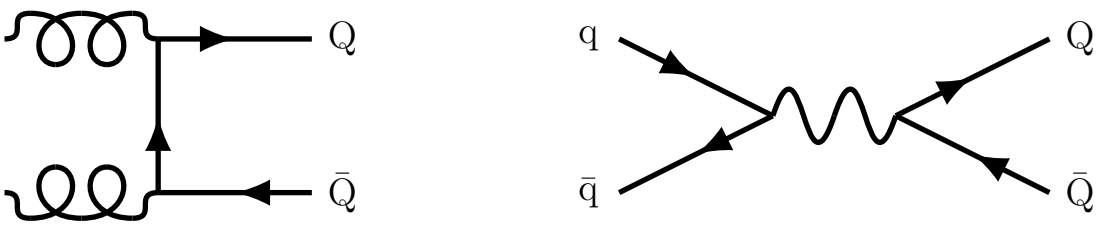

Figure 2.1: Feynman diagrams of the leading order heavy-quark production processes in hadron collisions.

Charmonium state	J/ψ(1S)	$\chi_{c0}(1P)$	$\chi_{c1}(1P)$	$\chi_{c2}(1P)$	ψ(2S)
J^{PC}	1^{--}	0^{++}	1^{++}	2^{++}	1^{--}
Mass (MeV/c^2)	3096.9	3414.7	3510.7	3556.2	3686.1
Decay width (MeV/c^2)	0.093	10.8	0.84	1.97	0.294
Feed-down $BR_{J/\psi+X}/BR_{tot}$ (%)	-	1.4	34.8	19.0	61.4
Binding energy (MeV/c^2) ($\Delta E \approx m_{D\bar{D}} - m_{c\bar{c}}$)	638	320	224	178	48
Average radius (fm)	0.50		0.72		0.90
Decay modes of the J/ψ			(branching ratio)		
J/$\psi \to$ hadrons			$(87.7 \pm 0.5)\%$		
J/$\psi \to e^+e^-$			$(5.94 \pm 0.06)\%$		
J/$\psi \to \mu^+\mu^-$			$(5.93 \pm 0.06)\%$		

Table 2.1: Quantum numbers and decay modes of charmonia with a J/ψ state in the decay chain [11, 29].

a Drell-Yan process. For colliding protons at LHC energies and a momentum transfer large enough for heavy-quark pair production, the corresponding Bjorken-x is in the range of $10^{-4} - 10^{-2}$. Hence, the PDF is gluon dominated and the prominent heavy-quark production process is gluon fusion. To understand quarkonia production in heavy-ion collisions, it is important to quantify the production of heavy quarks. This quantification is provided by the measurement of production cross sections (σ). Figure 2.2 depicts the charm (left) and bottom (right) quark production

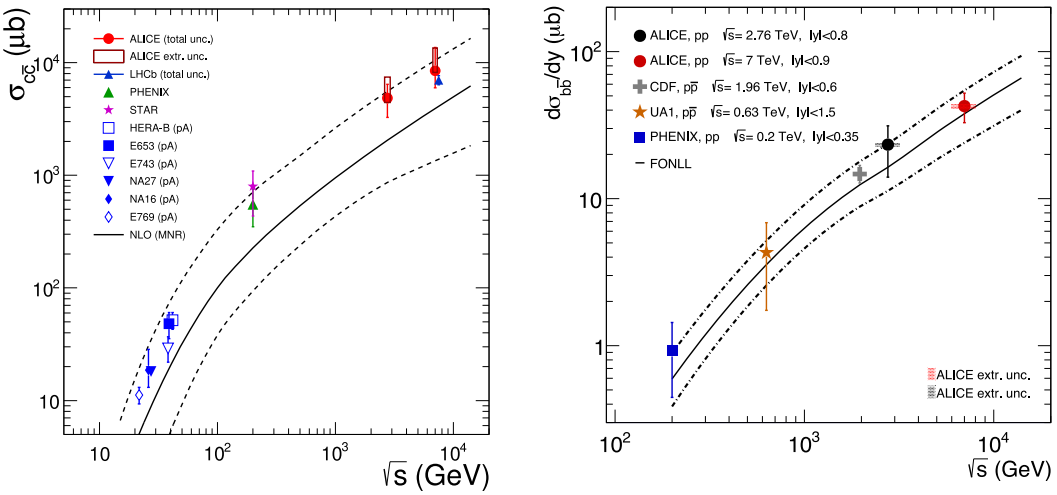

Figure 2.2: Charm (left) and bottom (right) quark production cross sections as function of the center-of-mass collision energy, for pp or p−A collisions scaled to single interactions, disregarding a potential nuclear matter effect. The dashed lines indicate the uncertainties of the NLO and respectively FONLL calculations [31].

cross-sections ($\sigma_{c\bar{c}}$, $\sigma_{b\bar{b}}$) as function of the center-of-mass collision energy, measured in pp and p−A collisions. The measurement in p−A collisions is scaled down to match the result of single pp collisions, disregarding potential CNM effects. A comparison to next-to-leading order QCD calculations is given in form of the drawn

band in the figures. For $\sigma_{c\bar{c}}$ an increment of a factor $\sim$ 10 between Relativistic Heavy-Ion Collider (RHIC) and LHC energies is observed.

After the initial production of a $Q\bar{Q}$ pair either a bound state of the produced quarks is formed or they couple with vacuum sea quarks. This factorization of the quarkonium production is part of almost all model approaches, which then differ in the hadronization part. A detailed description of quarkonium production in elementary interactions can be found in [31].

2.2 The initial idea: "J/ψ suppression by a quark-gluon plasma formation"

Even at LHC energies, only hard scatterings in the early stages of A−A collisions are able to provide enough energy to produce $c\bar{c}$ pairs. As a result, the quarks forming a J/ψ take part in the complete evolution of the collision, i.e. they are produced before a potential phase transition. The formation time (τ_f) of a J/ψ can be approximated utilizing the uncertainty principle and the mass splitting between the 1S and 2S states and it is in the region of $\tau_f \approx (m_{2S} - m_{1S})^{-1} \approx 0.3 - 0.4$ fm/c. As discussed in section 1.3 a phase transition is expected after $\sim$ 1 fm/c, thus it is in the same order of the formation of charmonia. In 1986 Matsui and Satz proposed the theory of "J/ψ suppression by a quark-gluon plasma formation" [26]. The underlying physics of their idea is an analogue to the ***Debye screening*** mechanism known from QED processes. According to Matsui and Satz, in a QGP the color charge responsible for the binding of the $c\bar{c}$ pair into a J/ψ should be screened by other quasi-free moving color charges of light quarks and gluons. Thus, the general quarkonia production should be suppressed compared to the production without a QGP phase. The strength of the screening can be quantified in an effective quark-antiquark potential which is dependent on the temperature of the medium [32]:

$$V_{q\bar{q}}(r,\ T) = -\frac{4}{3}\frac{\alpha_s}{r}\exp(-r\mu_D), \tag{2.1}$$

the Debye screening mass (μ_D) can be estimated via Lattice calculations, as being proportional to four times the temperature:

$$\mu_D \sim \frac{1}{r_D} \sim 4T. \tag{2.2}$$

Figure 2.3 visualizes the temperature dependence of the Debye radius. As function of T in units of T_c, the Debye radius (red line) and the energy density (blue line) is shown, with the expected dissociation temperature of a given charmonium resonance indicated by dashed lines.

An observable that quantifies this potential suppression is the so-called nuclear modification factor (R_{AA}):

$$R_{AA} = \frac{dN_{AA}}{N_{coll}\ \times\ dN_{pp}}. \tag{2.3}$$

It describes the ratio of the production of a given particle in A−A collisions (dN_{AA}) to the production in pp collisions (dN_{pp}), scaled with the expected amount of pp collisions in the observed A−A collisions (N_{coll}). The calculation of N_{coll} is based on the Glauber model [23], a geometrical model which associates the measured particle

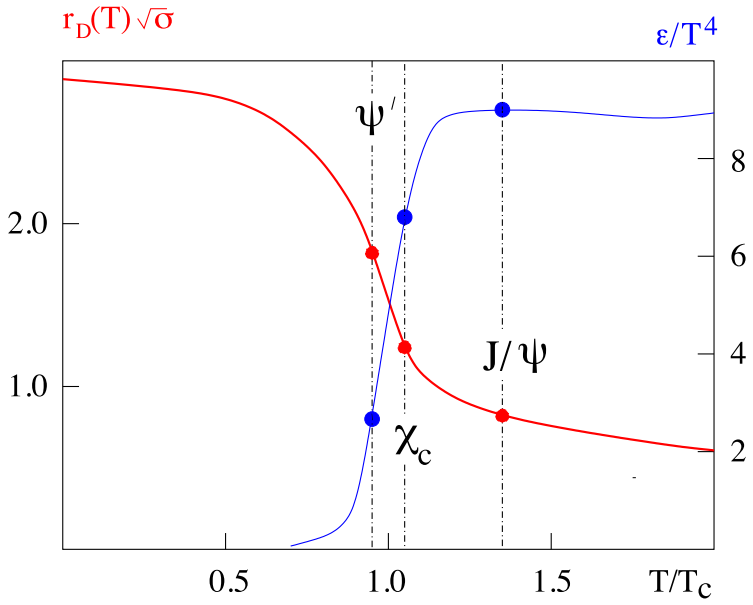

Figure 2.3: Debye radius (r_{D}) (red line) and energy density (ϵ/T^4) (blue line) as function of the temperature (T) in units of the critical temperature (T_{c}). Indicated by dashed lines are temperatures where given charmonia states should dissociate. [32]

multiplicity of an A−A collision via the impact parameter (b) of the collision with the number of binary pp collisions. The determination of the collision centrality within the ALICE experiment will be further discussed in section 4.3. In a naive approach the results of R_{AA} measurements could be interpreted in the following way:

$R_{\mathrm{AA}} = 1 \rightarrow$A − A collisions are a superposition of pp collisions,
$R_{\mathrm{AA}} > 1 \rightarrow$the nuclear medium produces an excess,
$R_{\mathrm{AA}} < 1 \rightarrow$a suppression due to the nuclear medium takes place.

Hence, according to Matsui and Satz, a phase transition into a QGP should result in a $R_{\mathrm{AA}}^{\mathrm{J}/\psi}$ below one. However, life is not that simple, for example counteracting effects could appear, such that even though R_{AA} equals one, a nuclear medium could have influenced the result. Additionally, the existence of nuclear matter around the hadronic collision is capable to influence the quarkonia production, resulting in the need of measurements of p−A collisions as important baseline to separate effects from CNM and a QGP phase.

2.3 Cold-Nuclear-Matter effects

In comparison to pp collisions the existence of surrounding nuclear matter in p−A and A−A collisions has an influence on the initial $\mathrm{c\bar{c}}$ pair production (initial state effects), as well as the charmonium formation (final state effects).

Initial state effects

The PDFs of nucleons are modified by surrounding nuclear matter. Depending on the momentum transfer, this leads to the so-called ***(anti-)shadowing effect***. With $x_{max,\ min} = \frac{m}{\sqrt{s_{\mathrm{NN}}}}\exp(\pm y)$ the distorted PDFs in nuclear matter cause a change of $\sigma_{\mathrm{c\bar{c}}}$

as function of rapidity (y) and transverse momentum (p_{T}) from pp to p−A collisions. As mentioned before, gluon fusion is the dominating process for the $\mathrm{Q\bar{Q}}$ production. However, the modification of the gluon density distributions is quite difficult to measure since there is no direct probe. Hence, up to now, the quantification of the (anti-)shadowing effect has large uncertainties due to the imprecise knowledge about the modifications of the gluon density distributions. [33]

A different approach to describe the influence of nuclear matter on the initial-stage $\mathrm{Q\bar{Q}}$ production is the Color Glass Condensate (CGC) model which incorporates the gluon saturation effect by accounting for the non-linear x evolution [34]. ***Multiple scattering*** of partons in the nuclear matter can occur either before or after the $\mathrm{c\bar{c}}$ production. Incoming partons are subject to collisional and radiative energy loss due to interactions with the nuclear matter. Hence, compatible kinematics of the final states require larger x for the initial partons producing the $\mathrm{c\bar{c}}$ pair in a hard scattering [35]. In particular the ***Cronin effect*** [36] describes a potential broadening of the p_{T} distribution of the partons, due to multiple scattering before the actual $\mathrm{c\bar{c}}$ production. However, the influence of the Cronin effect on the p_{T} spectrum of the produced J/ψ is not precisely known. Model calculations predict a potential enhancement of the J/ψ-p_{T} region between 3 and 10 GeV/c due to the appearance of the Cronin effect [31, 35].

Final state effects

After the initial $\mathrm{c\bar{c}}$ pair production, several CNM effects can influence the formation of a bound charm state. The ***comover*** effect describes a suppression of quarkonium production based on the excess of light-flavor mesons in nuclear matter. It leads to a non-negligible probability that the quarkonium state is not formed or dissociated due to interactions with co-moving light-flavor quarks or mesons. The $\mathrm{c\bar{c}}$ quarks then form open heavy-flavor mesons instead of hidden heavy-flavor bound states. [37, 38]

Furthermore, a reduced $\sigma^{\mathrm{J}/\psi}$ is expected because of inelastic interactions between the quarkonia states and the nuclear matter. The effect is quantified by the nuclear absorption cross-section (σ_{abs}) and the distance a given $\mathrm{c\bar{c}}$ pair has to pass through nuclear matter. Based on the Glauber model an average length (L) of nuclear matter traversed by the $\mathrm{c\bar{c}}$ state can be estimated [23]. Building ratios of $\sigma^{\mathrm{J}/\psi}$ measurements with heavy and light nuclei as targets for accelerated protons enable the extraction of the nuclear absorption cross-section for J/ψ ($\sigma^{\mathrm{J}/\psi}_{\mathrm{abs}}$) [39]. Figure 2.4 shows $\sigma^{\mathrm{J}/\psi}_{\mathrm{abs}}$ as function of $\sqrt{s_{\mathrm{NN}}}$ in the left panel. After an initial decrease of $\sigma^{\mathrm{J}/\psi}_{\mathrm{abs}}$ with the increase of $\sqrt{s_{\mathrm{NN}}}$, it seems to saturate between 2 and 4 mb. Depicted in the right panel of figure 2.4 is the production cross-section per target nucleon as function of L. The measured data is fitted by a full Glauber model calculation (line) and an approximation (dashed line), which describes the thickness of the nuclear matter based on the average density and length ($\langle \rho L \rangle$ approximation). From the measurements and comparisons to the Glauber model, the following proportionality can be extracted [23, 40]:

$$\sigma_{\mathrm{p-A}} \propto \sigma_{\mathrm{pp}} \cdot e^{-\sigma_{\mathrm{abs}} \langle \rho L \rangle} \tag{2.4}$$

The absorption due to nuclear matter surrounding the $\mathrm{c\bar{c}}$ production and charmonium formation process is also quoted as "***normal absorption***". More information on CNM effects and results of J/ψ measurements in p−A collisions can be found in [31, 39]. As summary of the CNM effects observed at the LHC, figure 2.5 depicts the nuclear modification factor for p−A collisions ($Q^{\mathrm{J}/\psi}_{\mathrm{pPb}}$) as function of the estimated

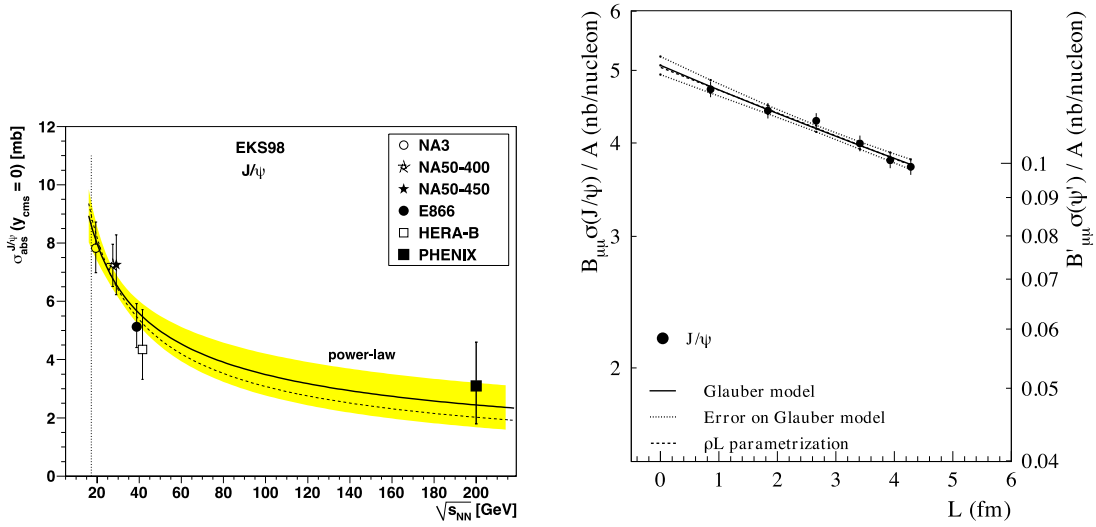

Figure 2.4: Left panel: the nuclear absorption cross-section for J/ψ($\sigma^{J/\psi}_{abs}$) as function of the collision energy ($\sqrt{s_{NN}}$) [31]. Right panel: J/ψ production cross-section normalized to the number of target nucleons as function of the length of traversed nuclear matter [40].

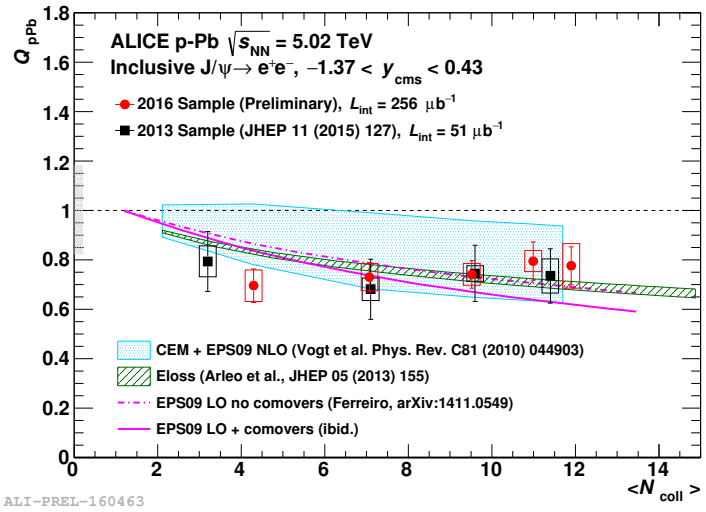

Figure 2.5: Nuclear modification factor for p−Pb collisions ($Q^{J/\psi}_{pPb}$) as function of the estimated number of collisions (N_{coll}), measured at mid-rapidity in $\sqrt{s_{NN}}$ = 5.02 TeV p−Pb collisions with ALICE, compared to several model approaches [41].

number of collisions (N_{coll}), measured at mid-rapidity in $\sqrt{s_{NN}}$ = 5.02 TeV p−Pb collisions with ALICE. A slight suppression of the J/ψ production is visible over the full N_{coll} range. The measured values are compatible with models based on different combinations of shadowing, CGC, comovers and parton energy loss due to multiple scattering [41]. From the measurements of p−Pb collisions a small "normal" suppression due to CNM effects of J/ψ production is expected also in Pb−Pb collisions at the LHC. Thus, those effects have to taken into account in analyses of the J/ψ production in Pb−Pb collisions at the LHC.

2.4 J/ψ measurements in heavy-ion collisions from SPS to LHC

2.4.1 Anomalous J/ψ suppression at SPS and RHIC

Taking the initial idea of Matsui and Satz and combining it with the correction for CNM effects, a suppression of J/ψ production should be visible in the ratio of the R_{AA} measured in A−A collisions over the estimated CNM-R_{AA} based on the measurements in p−A collisions. An anomalous suppression is observed by experiments at SPS and RHIC for charged particle multiplicities ($\frac{\mathrm{d}N}{\mathrm{d}\eta}$) larger than 300 measured at mid-rapidity. Figure 2.6 shows the results of those measurements

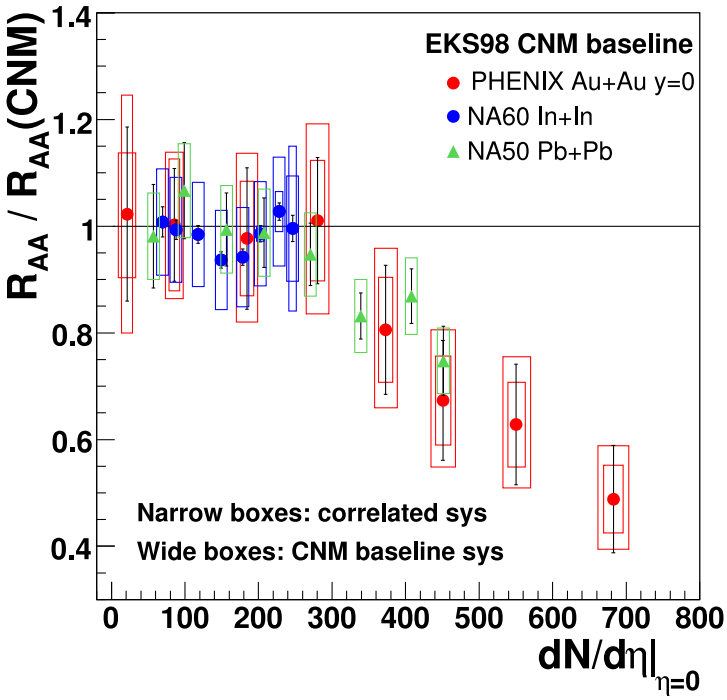

Figure 2.6: Ratio of R_{AA} measured in A−A collisions over the estimated CNM-R_{AA} as function of charged particle multiplicity ($\frac{\mathrm{d}N}{\mathrm{d}\eta}$) at mid-rapidity. The results of NA50 and NA60 correspond to $\sqrt{s_{\mathrm{NN}}} = 17.3$ GeV while the Phenix results have been measured at $\sqrt{s_{\mathrm{NN}}} = 0.2$ TeV. [42]

in which the suppression is observed. The correlation of the amount of suppression to the charged particle multiplicity indicates a (expected) dependence on the volume of the medium. Together with other observables, the suppression of J/ψ production measured at SPS and RHIC clearly supports the formation of a QGP in central Pb−Pb and Au−Au collisions above a certain collision energy. [42]

As follows from equation 2.1 and figure 2.3, the suppression of J/ψ production due to Debye screening should increase with temperature, thus the larger collision energies at the LHC ($\sqrt{s_{\mathrm{NN}}} \geq 2.76$ TeV), compared to SPS ($\sqrt{s_{\mathrm{NN}}} \leq 17.3$ GeV) and RHIC ($\sqrt{s_{\mathrm{NN}}} \leq 0.2$ TeV), should lead to an even stronger suppression. In figure 2.7 $R_{\mathrm{AA}}^{\mathrm{J}/\psi}$ is shown as function of the average number of collision participants (N_{part}), measured in $\sqrt{s_{\mathrm{NN}}} = 2.76$ TeV Pb−Pb and $\sqrt{s_{\mathrm{NN}}} = 0.2$ TeV Au−Au collisions at mid-rapidity (left) and forward rapidity (right). Peripheral collisions, represented by smaller N_{part} (< 50), seem to be subject to a comparable scale of suppression independent of the different collision energies. This is in agreement with the normal

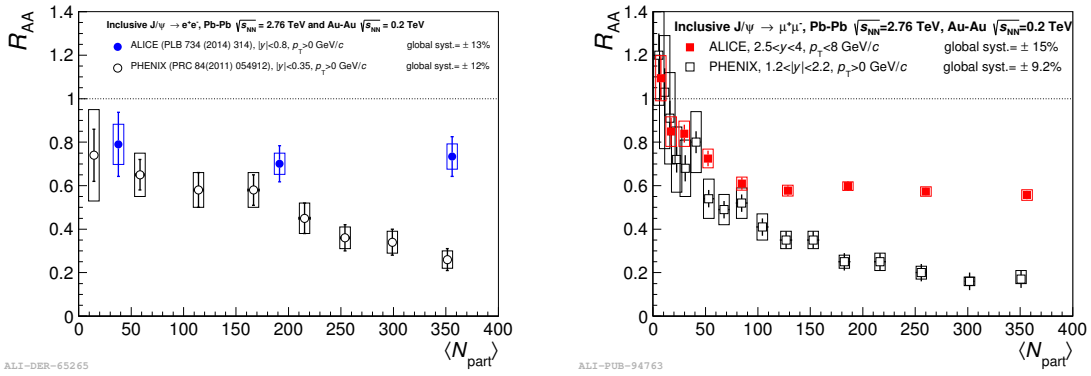

Figure 2.7: Comparison of the $R_{\mathrm{AA}}^{\mathrm{J}/\psi}$ measured in $\sqrt{s_{\mathrm{NN}}} = 2.76$ TeV Pb−Pb (blue/red) and $\sqrt{s_{\mathrm{NN}}} = 0.2$ TeV Au − Au collisions (black) at mid- (left) and forward rapidity (right) as function of the average number of collision participants (N_{part}) [43–45].

suppression expected due to CNM effects introduced in section 2.3. At more central collisions, despite the expectation of an increased suppression based on Debye screening, a significantly larger $R_{\mathrm{AA}}^{\mathrm{J}/\psi}$ is observed at LHC than at RHIC, independent of the rapidity (y) range of the measurement. Nonetheless, the general trend of a larger $R_{\mathrm{AA}}^{\mathrm{J}/\psi}$ at mid-rapidity compared to forward rapidity is still valid. However, this behavior was predicted by Braun-Munzinger and Stachel as well as Thews, Schroedter, and Rafelski in [46, 47] already ten years before the first collisions took place at the LHC. Phenomenologically the predictions are based on a ***(re)combination*** of dissociated, or previously uncorrelated $\mathrm{c\bar{c}}$-quarks enhancing measured J/ψ yields.

2.4.2 Enhanced J/ψ production due to (re)combination

Regeneration of quarkonia due to statistical (re)combination of heavy-quarks describes the probability, that a quasi-free single heavy quark finds another heavy quark to form a quarkonium bound state, instead of the open heavy-flavor state expected by the suppression approach of [26]. This effect has a strong dependence on $\sigma_{\mathrm{Q\bar{Q}}}$. Simplified, the more heavy quarks exist, the more likely it is that they find each other and form bound states. Thus, the rise of $\sigma_{\mathrm{Q\bar{Q}}}$ with $\sqrt{s_{\mathrm{NN}}}$ (see figure 2.2) should lead to an increase of the quarkonium production in heavy-ion collisions due to regeneration with $\sqrt{s_{\mathrm{NN}}}$. Within the regeneration picture, a simple approximation of the total J/ψ production in heavy-ion collisions is possible [48]:

$$N_{\mathrm{J}/\psi} \propto N_{\mathrm{c\bar{c}}}^2 / N_{\mathrm{ch}}. \tag{2.5}$$

In principle, this assumption should be valid for all heavy quarkonia. However, the regeneration mechanism does not only influence the number of produced J/ψ, also the distribution in phase space and the correlation to collective effects should differ between directly produced J/ψ and those created by (re)combination of $\mathrm{c\bar{c}}$ quarks. Whether the enhancement of the $R_{\mathrm{AA}}^{\mathrm{J}/\psi}$ at the LHC compared to RHIC is really due to the regeneration mechanism, or maybe something else is happening, should be visible in more differential measurements of the $R_{\mathrm{AA}}^{\mathrm{J}/\psi}$ and detailed comparisons to different model calculations.

2.4.3 Theoretical models for the J/ψ production at the LHC

There are several models that try to describe the J/ψ production in heavy-ion collisions. Those presented in comparisons to the data in section 2.4.4 and chapter 5 will be introduced here. All of them somehow include a production mechanism in their calculations based on the regeneration effect.

2.4.3a Statistical hadronization model:

Under the assumption that even at LHC energies almost all charm quarks are produced in early hard collisions, and that this initial amount of charm quarks is subject to conservation during a potential QGP phase, i.e. $N_{c\bar{c}}^{\text{initial}} \approx N_{c\bar{c}}^{\text{final}}$, the Statistical Hadronization Model (SHM) calculates the particle yields with respect to $N_{c\bar{c}}^{\text{initial}}$ at the phase boundary between a chemically equilibrated QGP and a hadron gas. Based on a grand canonical ensemble the model has T_{ch} and μ_b as free parameters and assumes that particles are produced according to their statistical weights at the phase boundary [49, 50]. Thus, within the SHM, all J/ψ are produced based on the combination of independent cc̄-quarks, and fully thermally equilibrated charm quarks should define the kinematical properties of the produced J/ψ [51]. A p_{T}

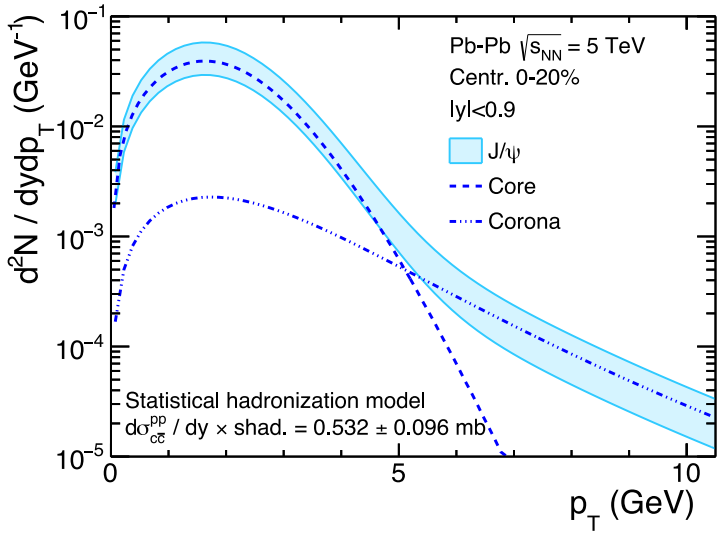

Figure 2.8: Estimation of the transverse-momentum spectrum of J/ψ modelled with the Statistical Hadronization Model (SHM) including the different contributions from J/ψ originating from the "core" and the "corona" [52].

spectrum for J/ψ calculated with the SHM is illustrated in figure 2.8. Essentially it consists of two types of J/ψ, those produced in the "core" assumed to be formed from previously thermally equilibrated cc̄-quarks and those originating from the "corona" of the fireball, with properties compatible to those produced in pp collisions. Accordingly, the corona part of the p_{T} spectrum is based on a fit to the measurements in pp collisions, the p_{T} spectrum of the core contribution is the result of a combination of hydrodynamic velocity profile calculations, propagated with a blast-wave function to the p_{T} spectrum, which is scaled with the core fraction from the SHM [52]. A clear difference between the two components is visible, while the corona J/ψ are distributed over a large range of p_{T}, those from the core and hence subject to a QGP phase are peaked around $p_{\text{T}} \approx 3$ GeV/c^2 and have a significant softer p_{T} distribution. Although the real p_{T} spectrum might be more complicated,

this approach nicely visualizes the difference between the kinematic properties of regenerated and direct J/ψ.

2.4.3b Transport models

Currently there are two transport models that try to describe the quarkonium production in heavy-ion collisions at the LHC [1, 53–55]. Both models are based on a kinetic rate equation including continuous dissociation and (re)combination of c$\bar{\text{c}}$ pairs. The models use the measured values of $\sigma_{\text{c}\bar{\text{c}}}$ in heavy-ion collisions as an estimator for the initial amount of c$\bar{\text{c}}$ quarks in the fireball. While the model by Zhou et al. explicitly employs gluon dissociation ($J/\psi + g \rightarrow c + \bar{c}$) as the dominant dissociation process, Zhao and Rapp dissociate charmonia in light parton (u, d, s and g) interactions (($J/\psi + p \rightarrow p + c + \bar{c}$)), with the partons originating from the QGP heat bath. Note the difference of the utilized processes, in [55] an inelastic process, with only the c$\bar{\text{c}}$ quarks in the final state, is used, the model of Zhao and Rapp [1, 53, 54] uses a quasi-free approach with the dissociated c$\bar{\text{c}}$ quarks and an additional parton in the final state. The dissociated c$\bar{\text{c}}$ quarks are then transported through the fireball according to the Boltzmann transport equation taking the mass, width and binding energy of charmonium states into account. In the model of Zhao and Rapp for the two-body heavy-quark potential a strong-binding scenario (SBS) (2 T_{c}) and a weak-binding scenario (WBS) (1.2 T_{c}) is separately assumed, representing upper and lower limiting cases for the J/ψ dissociation temperature. Within the model, those limiting cases result in a smaller (SBS) and a larger (WBS) fraction of regenerated J/ψ. The transport model by Zhou et al. explicitly adds the evolution of the fireball properties based on a hydrodynamical approach as input to the kinetic rate equation. Both models allow a separated access to the properties of the J/ψ produced by different mechanisms. Those J/ψ formed from initial c$\bar{\text{c}}$ pairs, without a significant influence of the medium on the spectral distributions, are called "primordial" J/ψ in the models. J/ψ produced via the regeneration mechanism, as introduced in section 2.4.2, are labeled as "regenerated" J/ψ. Their kinematic properties are modified compared to those of the primordial J/ψ, due to the extended amount of interactions of the c$\bar{\text{c}}$ quarks with the medium. In figure 2.9 the estimated $R_{\text{AA}}^{\text{J}/\psi}$ as function of p_{T} for $\sqrt{s_{\text{NN}}} = 2.76$ TeV Pb−Pb collisions from Zhou et al. (left) and Zhao and Rapp (right) is shown. For both models, a separated estimation for primordial and regenerated J/ψ of the nuclear modification factor is given. As expected, the interaction with the medium modifies the p_{T} distribution. Regenerated J/ψ are shifted towards lower p_{T} compared to primordial J/ψ.

2.4.3c Comover interaction model

The Comover Interaction Model (CIM) estimates the J/ψ production based on initially produced c$\bar{\text{c}}$ pairs interacting with comoving partons or hadrons of the medium, invoking dissociation and regeneration of J/ψ mesons. It is a non-equilibrium model, containing, in addition to the comover interaction, initial-state effects like shadowing [56]. Assuming an equal cross section for dissociation and regeneration by comover interactions, the influence on the J/ψ yields of the medium is mainly driven by the initial c$\bar{\text{c}}$ density.

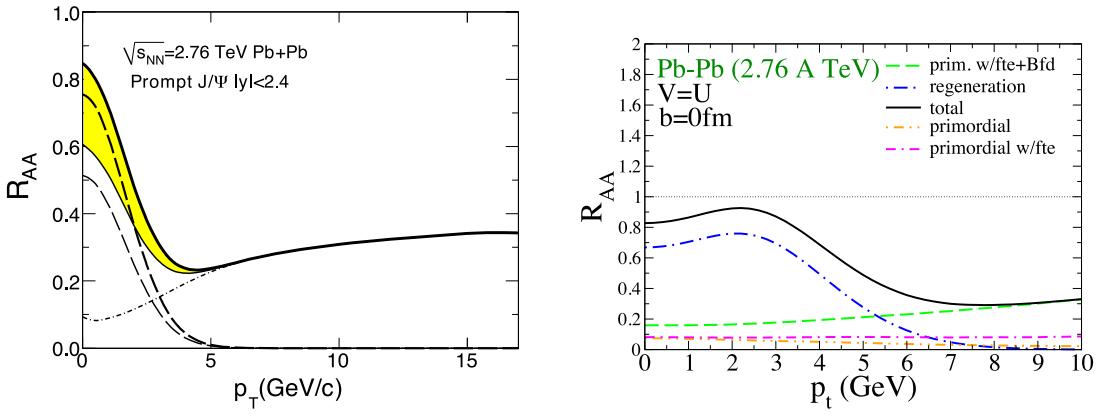

Figure 2.9: Calculations of the nuclear modification factor (R_{AA}) as function of the transverse momentum (p_{T}), performed in the framework of the transport model by Zhou et al. (left) and Zhao and Rapp (right). In the left plot the dashed lines represent the fraction of regenerated J/ψ and the dot-dashed line the fraction of primordial J/ψ. For the calculation by Zhao and Rapp the strong-binding scenario (SBS) of the model was applied and formation-time effects (fte), as well as B feeddown (Bfd) explicitly added. [54, 55]

2.4.4 Latest results from J/ψ measurements at the LHC

In this section, a short review of the latest results on J/ψ measurements will be given. While the general existence of a regeneration component in the J/ψ production as result of the measurements in $\sqrt{s_{\mathrm{NN}}} = 2.76$ TeV Pb−Pb collisions is widely accepted (figure 2.7), a more quantitative understanding of the J/ψ production is not yet available. For example, the relative strength of the primordial and the regenerated component of the J/ψ production as function of p_{T} and N_{part} needs further investigation. Also, on a microscopic level, as represented by the transport models (see 2.4.3b), there are a lot of open questions that need to be answered, i.e. a detailed understanding of the in-medium heavy-quark potential is not yet available. A strong-binding scenario is as compatible with the data from $\sqrt{s_{\mathrm{NN}}} = 2.76$ TeV Pb−Pb collisions as a weak-binding scenario for the J/ψ binding energy in the fireball, within the model by Zhao and Rapp [53, 54]. With regard to the regeneration picture, a small increase of the $R_{\mathrm{AA}}^{\mathrm{J}/\psi}$ should be visible between $\sqrt{s_{\mathrm{NN}}} = 2.76$ TeV and $\sqrt{s_{\mathrm{NN}}} = 5.02$ TeV collision energy, since the increase of $\sigma_{\mathrm{c\bar{c}}}$ is expected to be stronger than the additional anomalous suppression in this energy regime. The $R_{\mathrm{AA}}^{\mathrm{J}/\psi}$ measurement as function of the average number of participants at forward (left) and mid-rapidity (right) in $\sqrt{s_{\mathrm{NN}}} = 5.02$ TeV Pb−Pb collisions is depicted in figure 2.10. Estimations from the models introduced in 2.4.3 are represented by the colored surfaces, with the lines representing the minimum and maximum variation based on the input uncertainties, which are mainly dominated by the uncertainties of the $\sigma_{\mathrm{c\bar{c}}}$ measurement. In comparison to the results at $\sqrt{s_{\mathrm{NN}}} = 2.76$ TeV, a slightly larger $R_{\mathrm{AA}}^{\mathrm{J}/\psi}$ is observed in both rapidity ranges, at mid-rapidity it exceeds unity for $N_{\mathrm{part}} \gtrsim 350$. However, it is difficult to draw clear conclusions concerning the production mechanisms from this measurement, especially considering the uncertainties of the measurement and the models. As introduced in section 2.4.3, the p_{T} distributions of initial and regenerated J/ψ differ in the given theoretical descriptions, providing

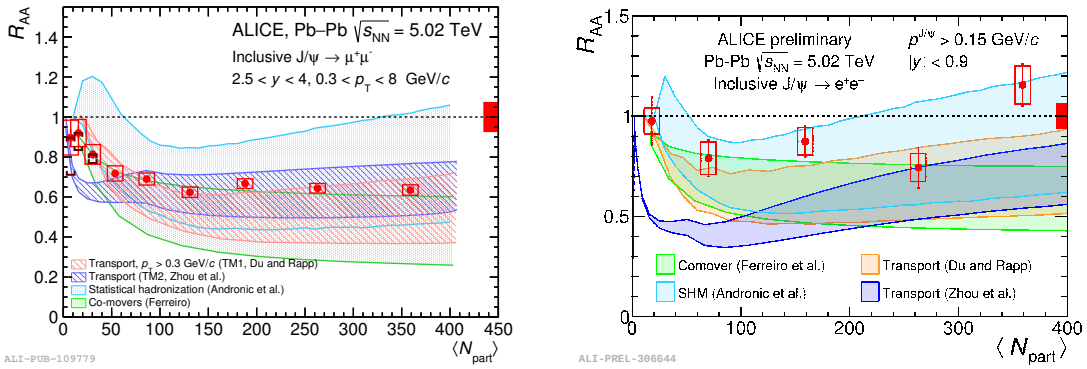

Figure 2.10: $R_{\mathrm{AA}}^{\mathrm{J}/\psi}$ measured at forward (left) and mid-rapidity (right) as function of N_{part} in $\sqrt{s_{\mathrm{NN}}} = 5.02$ TeV Pb−Pb collisions in comparison to calculations from transport models, the Statistical Hadronization Model (SHM) and the Comover Interaction Model (CIM) (see section 2.4.3) [57, 58].

the opportunity to gain further insights on the J/ψ productions by measurements of the transverse-momentum distribution of J/ψ.

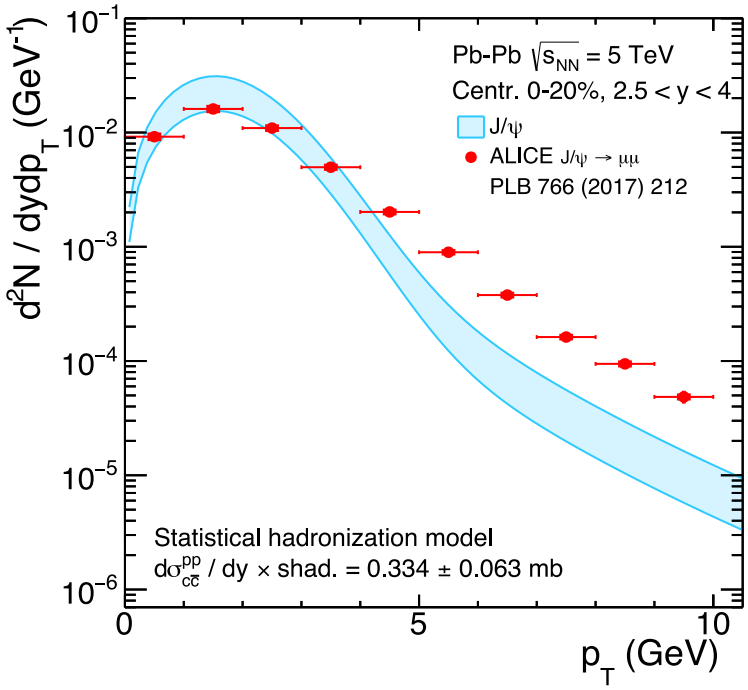

Figure 2.11: J/ψ transverse-momentum spectrum as calculated from the statistical hadronization model and measured at forward rapidity in the 20% most central $\sqrt{s_{\mathrm{NN}}} = 5.02$ TeV Pb−Pb collisions [52, 57].

In figure 2.11 a comparison between the transverse-momentum spectrum measured at forward rapidity in $\sqrt{s_{\mathrm{NN}}} = 5.02$ TeV Pb−Pb collisions and the one estimated with the framework of the SHM is given. The comparison is done on a selection of the 20% most central events, which enriches the J/ψ sample with an abundant amount of J/ψ matching the core definition of the SHM. Up to $p_{\mathrm{T}} \approx 5$ GeV/c an agreement between the data and the model is visible, nonetheless, for transverse momenta above 5 GeV/c, a clear deviation appears.

To highlight the influence of a potential QGP phase on the transverse-momentum spectrum, the $R_{\mathrm{AA}}^{\mathrm{J}/\psi}$ as function of transverse momentum is being calculated. Simi-

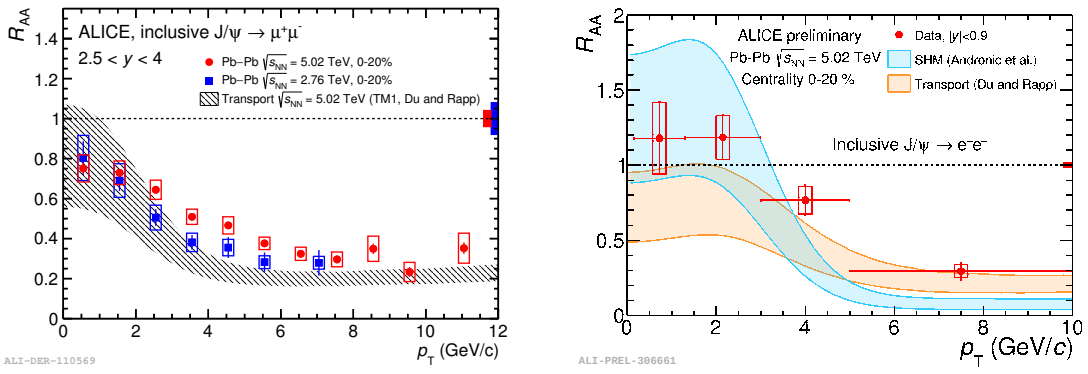

Figure 2.12: $R_{\mathrm{AA}}^{\mathrm{J}/\psi}$ as function of transverse momentum (p_{T}) measured in the 20% most central $\sqrt{s_{\mathrm{NN}}} = 5.02$ TeV Pb−Pb collisions at forward (left) and mid-rapidity (right) set side by side with calculations from the transport model of Du and Rapp and the Statistical Hadronization Model [57, 58]

lar to the measurement of the $R_{\mathrm{AA}}^{\mathrm{J}/\psi}$ as function of N_{part}, the transverse-momentum spectrum measured in pp collisions is used as baseline, and a deviation from unity corresponds to more or less produced J/ψ in the given momentum bin in Pb−Pb collisions. The $R_{\mathrm{AA}}^{\mathrm{J}/\psi}$ as function of p_{T} measured at forward (left) and mid-rapidity (right) together with estimations from the transport model by Du and Rapp and the SHM at mid-rapidity is depicted in figure 2.12 [1, 57, 58]. A fall of $R_{\mathrm{AA}}^{\mathrm{J}/\psi}$ from low to high p_{T} is observed at forward as well as at mid-rapidity. This observation agrees with the combination of J/ψ dissociation and (re)combination shifting the transverse momentum distributions of J/ψ towards $p_{\mathrm{T}} \approx 3$ GeV/c, as predicted by models containing a regeneration component. Also, the more strongly pronounced growth at mid-rapidity exceeding unity is anticipated, since the rapidity profile of $\sigma_{\mathrm{c\bar{c}}}$ rises towards mid-rapidity. At forward rapidity additionally the measurement at $\sqrt{s_{\mathrm{NN}}} = 2.76$ TeV collision energy is shown. Slightly higher values are visible, for the higher center-of-mass energy in the range of $2 < p_{\mathrm{T}} < 6$ GeV/c. However, this excess is not very significant, especially if one takes the global uncertainty into account. Nevertheless, in the same p_{T} region also the strongest deviation from the prediction of the transport model by Du and Rapp in both rapidity ranges is given. Results extracted from a small sample of Xe−Xe collisions at $\sqrt{s_{\mathrm{NN}}} = 5.44$ TeV seem to indicate comparable relative contributions of regeneration and suppression at similar $\sqrt{s_{\mathrm{NN}}}$ and N_{part} [59]. Although clearly supporting the regeneration picture, the measurements of $R_{\mathrm{AA}}^{\mathrm{J}/\psi}$ as function of N_{part} and p_{T} currently do not provide strong enough constraints for more detailed conclusions. Multi-differential J/ψ measurements are currently being performed at forward rapidity, including the analysis of the J/ψ yield as function of y, p_{T} and collision centrality. Preliminary results of these analyses can be found in [60, 61].

Another possibility to provide further constraints on the charmonium production mechanisms in heavy-ion collisions is the measurement of the ***elliptic flow*** of J/ψ. A potential chemical and thermal equilibration of charm quarks presupposes a pronounced interaction with the medium and hence the charm quarks should be subject to collective phenomena like elliptic flow. In chapter 5, the analysis of the elliptic

flow of J/ψ measured in $\sqrt{s_{\mathrm{NN}}} = 5.02$ TeV Pb−Pb collision will be discussed and compared to other existing measurements and calculations from models.

3 Experimental apparatus

In this chapter, the experimental prerequisites for the analyses presented in chapters 5 and 6 will be presented and discussed. Beginning with an introduction of the LHC providing the Pb−Pb collisions, followed by an exploration of the ALICE detector performing the measurement itself, and completed by a review of the data sample and the software framework the analyses have been performed on and with.

3.1 Large Hadron Collider (LHC)

Developed at the end of the 20th century and successfully performing the first ever Pb−Pb collisions in the TeV energy regime in 2010, the LHC is the world's largest particle accelerator and often even called the world's largest machine. The full

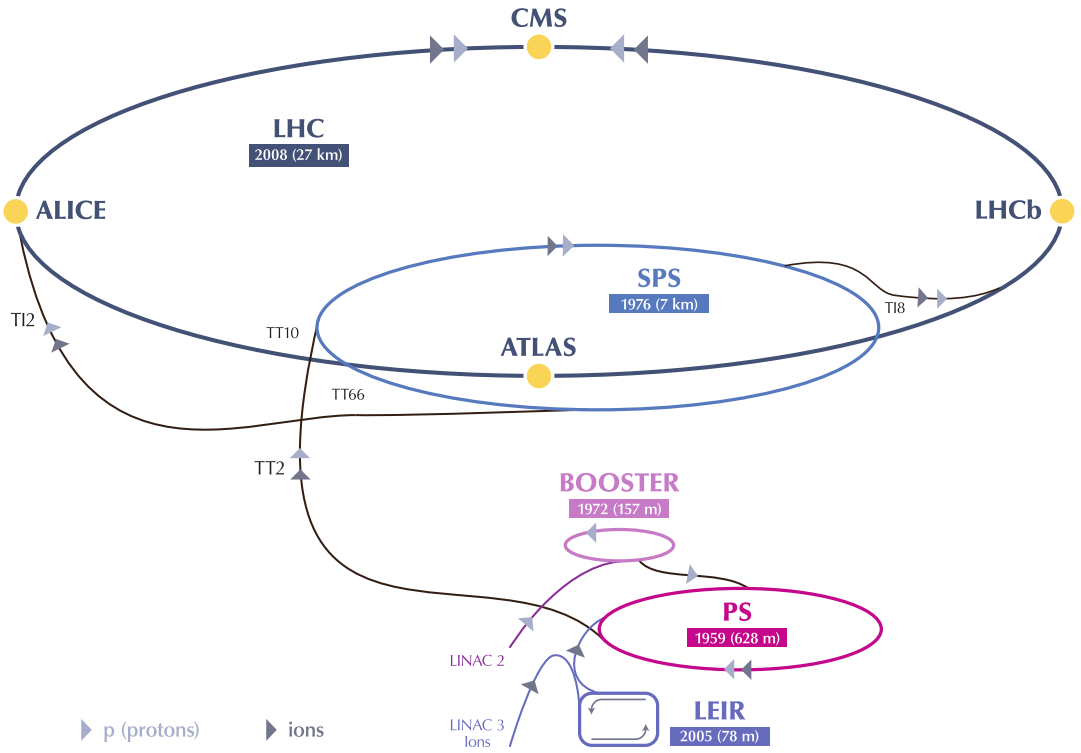

Figure 3.1: Sketch of the parts of CERNs accelerator complex responsible for the pp and A−A collisions induced at the four interaction points of the LHC. Figure adopted from [62]

complex needed for the acceleration of protons and ions to collision energies in the TeV energy regime is sketched in figure 3.1. Since the dynamical range of the magnets used to bent trajectories of the accelerated particles has an upper and lower limit, particles have to a have a minimum velocity when entering the LHC and thus they have to go through the chain of smaller accelerators from the LINear ACcelerator (LINAC) to the SPS before entering the LHC. Based on the nominal maximum field of the dipole magnets ($B = 8.33\text{T}$), protons can reach a

maximum energy of 7 TeV [63]. The nominal top energy for ions can be calculated via $E_{\mathrm{A}} = E_{\mathrm{p}} \cdot \frac{Z}{A}$, accordingly lead ions ($^{208}_{82}\mathrm{Pb}^{82+}$) are accelerated to a top energy of 2.759 TeV [64]. During Run 2, which is defined as the data taking period from 2015 to 2018, pp, p−Pb, Xe−Xe and Pb−Pb collisions where performed at collision energies between $\sqrt{s_{\mathrm{NN}}} = 5.02$ TeV and $\sqrt{s} = 13$ TeV. The analyses presented in this thesis are mainly based on the heavy-ion collision sample collected at the end of 2015. That sample contains Pb−Pb collisions at $\sqrt{s_{\mathrm{NN}}} = 5.02$ TeV collision energy, taken at interaction rates of 300-400 Hz (low interaction rate, 13 runs) and 1.0-7.5 kHz (high interaction rate, 159 runs) at the interaction point of the ALICE experiment. The low and high interaction rate data samples accumulate together 155 million minimum bias events before individual event selection criteria are applied.

3.2 A Large Ion Collider Experiment (ALICE)

ALICE is the dedicated heavy-ion experiment at the LHC built to measure an abundant variety of observables. Therefore, it was designed to perform precision measurements even in a high track-density environment. The detector system sketched in figure 3.2 and 3.3 is divided into two rapidity ranges. While at forward rapidity ($2.5 < y < 4$) a muon spectrometer devoted to the measurement of muons is installed, at mid-rapidity ($|y| \lesssim 0.9$) several subdetectors are combined to the so-called "central barrel" capable to identify and measure various particle species. At forward rapidity, J/ψ can be measured in the their dimuon decay channel with the muon spectrometer providing an excellent signal to background ratio. The central barrel detectors enable a J/ψ reconstruction in the dielectron decay channel. Both detector configurations allow the measurement of J/ψ down to zero transverse momentum, which is at the LHC a particular feature of the ALICE detector. In the following, the detectors used in the analyses presented in this thesis will be introduced, a full review of the ALICE detector can for example be found in [65, 66].

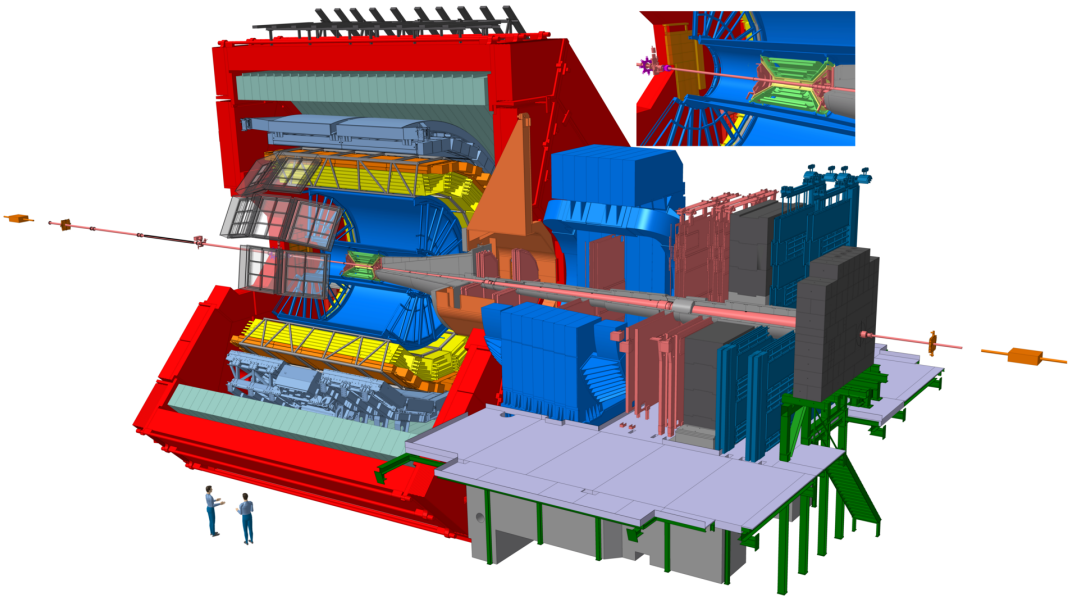

Figure 3.2: Sketch of the A Large Ion Collider Experiment (ALICE) detector in form of a 3D model [67].

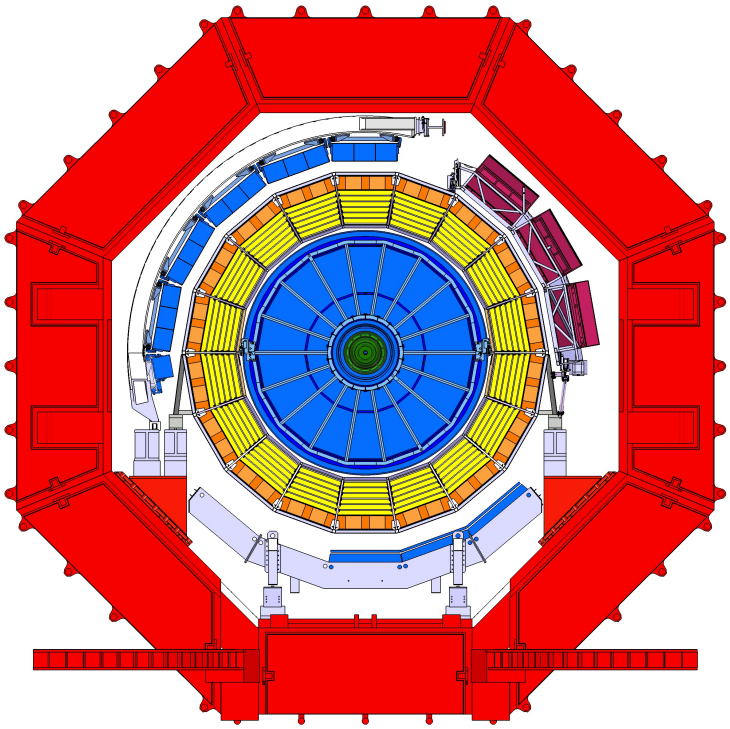

Figure 3.3: Cross section of the ALICE central barrel detectors [65].

3.2.1 The central barrel detectors

For the J/ψ measurement at mid-rapidity, the central barrel detectors have to deliver certain information on the measured particles, including a precise measurement of the trajectory, the transverse momentum, and information on the species of the particle. To extract the ***transverse momentum***, a magnetic field of $B_{\text{nominal}} = 0.5$ T ($B_{\text{low}} = 0.2$ T) is induced by a solenoidal magnet surrounding the central barrel detectors, bending the particle trajectories according to the Lorentz force:

$$\mathbf{F} = q(\mathbf{E} + \mathbf{v} \times \mathbf{B}). \tag{3.1}$$

A precise knowledge of the magnetic field and the track curvature (ρ) allows a high-resolution p_{T} measurement. In units common for high energy experiments (p_{T} [GeV/c], ρ [m], B [T], q [e]) the transverse momentum can be calculated based on:

$$p_{\text{T}} = 0.3 \cdot qB_{\perp} \cdot \rho. \tag{3.2}$$

The ***trajectory*** is reconstructed from space points, measured by the subdetectors, with a Kalman filter approach [65]. The trajectories are approximated as a helix defined by five parameters: y, z, $\sin(\varphi)$, $\tan(\lambda)$, $1/p_{\text{T}}$, where λ denotes the angle between the $x - y$ plane and the beam axis [68]. Hence, the resulting trajectory from the Kalman fit also provides access to the transverse momentum of the particle. Different techniques are applied to identify the various species of particles. Dependent on the species and the transverse momentum, the techniques deliver varying performances. For the identification of electrons with $p_{\text{T}} > 1$ GeV/c, as used in the J/ψ analyses presented in this thesis, the Time Projection Chamber (TPC) delivers a great performance. However, specially in the higher p_{T} regions, the TRD can add supplementary PID information. The detailed techniques utilized by the subdetectors will be described in the according sections (3.2.1b, 3.2.1c).

3.2.1a Inner Tracking System (ITS)

Placed at the most inner part of the central barrel, the Inner Tracking System (ITS) provides tracking and PID information utilizing silicon detectors. Sketched in

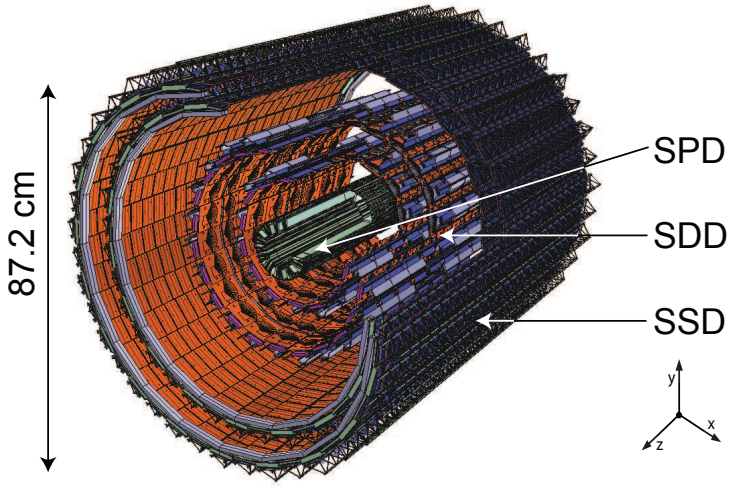

Figure 3.4: Drawing of the ALICE Inner Tracking System (ITS) and its three subsystems [69].

figure 3.4 the ITS consists of three subdetectors, the Silicon Pixel Detector (SPD), Silicon Drift Detector (SDD) and the Silicon Strip Detector (SSD), each consisting of two layers, with a complete radial extension from 3.9 cm to 43 cm. All six layers cover a pseudo-rapidity interval of at least ± 0.9 centered at zero, which corresponds to the full pseudo-rapidity range of the central barrel detectors ($|\eta| < 0.9$). The total material budget of the ITS (including air) sums to 7.26% of the radiation length. For the J/ψ reconstruction at mid-rapidity, it is the main source for background electrons from photon conversions. The PID capabilities of the ITS focus on low transverse momentum particles ($p_{\mathrm{T}} < 1$ GeV/c).

3.2.1b Time Projection Chamber (TPC)

The main PID and tracking device at mid-rapidity is the Time Projection Chamber (TPC). Starting at about 85 cm it extends to 250 cm in radial direction, and with a length of 500 cm it matches the pseudo-rapidity range of $|\eta| < 0.9$. Figure 3.5 shows the schematic layout of the ALICE TPC. It is a large gaseous time projection chamber, which uses MultiWire Proportional Chambers (MWPCs) for the signal readout. Ionizing radiation entering the gas volume of the TPC releases electrons from the gas atoms. These electrons then drift towards the readout chambers along the electrical field between the central electrode and the readout chambers. An additional field cage along the beam axis is supposed to minimize irregularities of the drift field. Since, the drift velocity is part of the limiting factors on the readout rate, the strength of the field is chosen as high as stable running conditions are ensured. In the case of the ALICE TPC $U_{\mathrm{Drift}} = 100\ kV$, which was an unprecedented value at the time of the development for large gaseous TPCs. Based on the constant drift velocity, the z component of a given trajectory can be calculated from the drift time of the electrons. A precise measurement of the $r\varphi$ component is performed by segmented readout chambers. Three different pad sizes are used starting from $r\varphi \times r = 4 \times 7.5$ mm^2 at the most inner part to 6×10 mm^2 and 6×15 mm^2 in

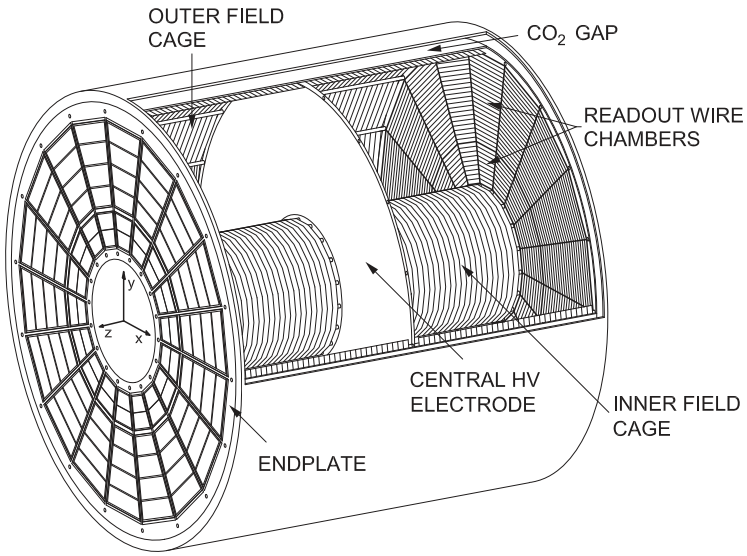

Figure 3.5: Illustration of the layout of the ALICE Time Projection Chamber (TPC) [70].

the middle and at the outer parts. In radial direction, there are 63 rows of the smallest pads, followed by 64 rows of middle-sized pads and 32 rows of the largest pads, adding up to a total of 159 pad rows. The segmented pads and the drift-time measurement result in a space-point resolution of < 1 mm in both directions, and a TPC standalone p_{T} resolution between 1% and 7%, strongly depending on the particle's momentum in the range of $1.5 < p_{\mathrm{T}} < 10$ GeV/c. [70]

As already indicated, the TPC is also capable to perform particle identification of ionizing particles. Charged particles traversing through the gas deposit energy according to the "Bethe equation" (often also referred to as "Bethe-Bloch equation") [11, 71]:

$$\left\langle \frac{\mathrm{d}E}{\mathrm{d}x} \right\rangle = Kz^2 \frac{Z}{A} \frac{1}{\beta^2} \left[\frac{1}{2} \ln \frac{2m_e c^2 \beta^2 \gamma^2 W_{\max}}{I^2} - \beta^2 - \frac{\delta(\beta\gamma)}{2} \right]. \tag{3.3}$$

From the Bethe-Bloch equation it is visible that the amount of deposited energy does not depend on the particle mass. However, since it is a function of the electrical charge (z) and velocity ($\beta,\ \gamma$), the combined measurement of the momentum p and the mean specific energy loss ($\left\langle \frac{\mathrm{d}E}{\mathrm{d}x} \right\rangle$) provides information to identify particles. A measurement of $\left\langle \frac{\mathrm{d}E}{\mathrm{d}x} \right\rangle$ as function of $\beta\gamma$ and an according parametrization is shown in figure 3.6 (left). Clean samples of various particles are identified by different selection schemes and used to cover certain ranges of $\beta\gamma$ to enable a precise $\left\langle \frac{\mathrm{d}E}{\mathrm{d}x} \right\rangle$ measurement. The special topology of neutral K^0, $\bar{\Lambda}^0$ and Λ^0 decays, due to the shape of the registered tracks called V_0 decays, allow the identification of pions and protons, without the utilization of $\mathrm{d}E/\mathrm{d}x$ information. In a similar manner, electrons are identified. A $\gamma + X \rightarrow e^+e^-$ decay also leads to a V_0 topology, which allows the selection of the electrons in the decay channel. The muon sample is recorded without collisions, using cosmic muons traversing through the TPC. Based on this sample of identified particles, a parametrization of the Bethe-Bloch equation for the conditions of the ALICE TPC is prepared. Dependent on the momentum, a separation between, and together with the parametrization, an identification of particles is possible. The right panel of figure 3.6 illustrates the individual bands drawn by particles with different masses, due to their divergent $\beta\gamma$ at similar p/z. To identify particles in physics analyses with the TPC, the parametrized Bethe-

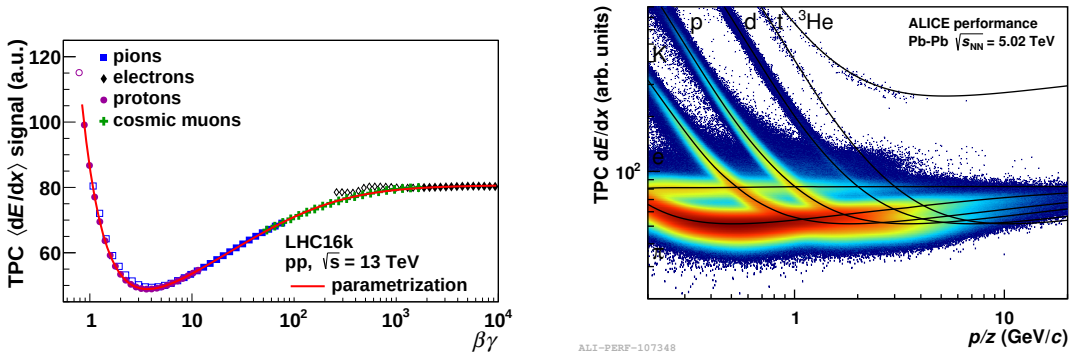

Figure 3.6: Left: Parametrization of the Bethe-Bloch equation based on measurements with the ALICE TPC [72]. Right: specific energy loss ($\mathrm{d}E/\mathrm{d}x$) measurement in $\sqrt{s_{\mathrm{NN}}} = 5.02$ TeV Pb−Pb collisions with the TPC as function of the rigidity (p/z), with lines indicating the expected $\left\langle \frac{\mathrm{d}E}{\mathrm{d}x} \right\rangle$ from the Bethe-Bloch parametrization for different particles [73].

Bloch function is compared to the measured $\mathrm{d}E/\mathrm{d}x$ as function of the momentum measured at the inner radius of the TPC (p_{TPC}) with different mass assumptions:

$$n\sigma^{\mathrm{TPC}}_{\mathrm{Particle}}(p_{\mathrm{TPC}}) = \frac{\left(\frac{\mathrm{d}E}{\mathrm{d}x}\right)_{\mathrm{measured}}(p_{\mathrm{TPC}}) - \left(\frac{\mathrm{d}E}{\mathrm{d}x}\right)^{\mathrm{Particle}}_{\mathrm{param.}}(p_{\mathrm{TPC}})}{\sigma_{\mathrm{res.}}(p_{\mathrm{TPC}})}. \tag{3.4}$$

In equation 3.4, $\sigma_{\mathrm{res.}}$ corresponds to the resolution of the $\mathrm{d}E/\mathrm{d}x$ measurement for a given track. The deviation between the measured and the expected $\mathrm{d}E/\mathrm{d}x$ for a given particle, based on the Bethe-Bloch parametrization, is then normalized to the resolution of the measurement and quoted as $n\sigma^{\mathrm{TPC}}_{\mathrm{Particle}}$. Several procedures are performed to calibrate the $\mathrm{d}E/\mathrm{d}x$ measurement of the TPC. The measured $\mathrm{d}E/\mathrm{d}x$ of a particle with a given momentum is dependent on the track's rapidity and the track density in the TPC. A review of the calibration procedures will be given within the discussion of the applied PID cuts for the analyses in section 4.6.

3.2.1c Transition Radiation Detector

Since the restart of the LHC in 2015, the TRD is finally completely installed and covers now the full azimuth and a similar pseudo-rapidity range ($|\eta| < 0.84$) like the ITS and TPC. Transition radiation is created with a certain probability when ultra-relativistic particles ($\gamma \gg 1$) cross boundaries between two materials with unequal permittivities. The spectrum and yield of the produced transition radiation depends on the one hand on the configuration of the utilized radiator, and on the other hand on the γ factor of the traversing particle:

$$S_0 = \iint \left(\frac{d^2 S_0}{d\theta d\omega}\right) d\theta d\omega = \frac{\alpha\hbar}{3}\frac{(\omega_A - \omega_B)^2}{\omega_A - \omega_B}\gamma. \tag{3.5}$$

Equation 3.5 describes the calculation of the integrated intensity S_0 of transition radiation as introduced by Cherry et al. in [74]. In the equation, ω_{A} and ω_{B} denote the plasma frequencies of the materials the radiator is composed of. The plasma frequencies of the materials are limited to their permittivity:

$$\epsilon_{A,B} = 1 - \frac{\omega^2_{A,B}}{\omega^2_P}. \tag{3.6}$$

Within the relevant momentum range, only electrons reach γ factors high enough ($\gamma \gtrsim 1000$) to produce transition radiation with finite probabilities. Hence, the measurement of transition radiation can be used to identify electrons.

The ALICE TRD is built around the TPC. It consists of 522 readout chambers, summing up to a total of 1,150,848 readout channels, arranged in 18 "supermodules" each divided into six layers and five stacks, as illustrated in figure 3.7. A single

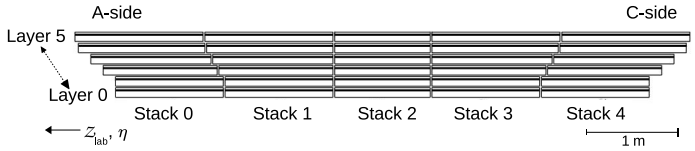

Figure 3.7: Cross-section of an ALICE TRD supermodule visualizing the arrangement into layers and stacks [75].

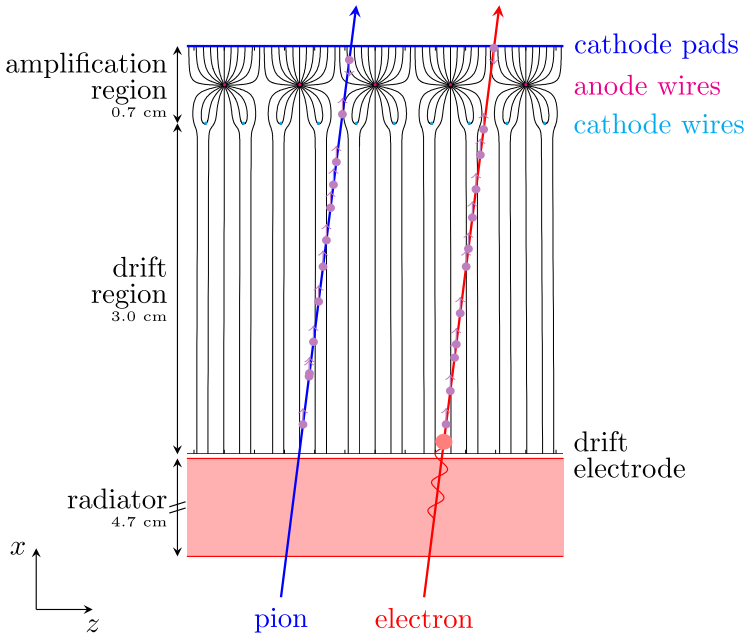

Figure 3.8: Schematic illustration of the structure of a single ALICE TRD chamber [75].

chamber is built from a combination of a foam/fibre radiator and a MWPC-based signal readout. Figure 3.8 sketches a cross-section of such a chamber, including an example for the different behavior of electrons and pions traversing the chamber. After passing the radiator potentially producing transition radiation, particles enter the gas volume, currently filled with a mixture of xenon and carbon dioxide ($Xe/CO_2 \approx 85/15$). There they deposit energy according to the Bethe-Bloch equation (3.3) in the 3 cm long drift region, in similar processes like in the TPC. Primary electrons from the ionization of the gas atoms drift towards the amplification region forced by the drift field. In the large electrical field around the amplification wires, they are accelerated and an ionization avalanche occurs. Typically around 3,500 electrons are produced per primary electron in such an avalanche. The resulting gas ions induce a charge on the cathode planes, which is read out via segmented cathode pads on the backside of the chamber. If a particle produces transition radiation when traversing the radiator, the combination of the energy of the transition-radiation photon and the energy deposited via gas ionization by the particle leads

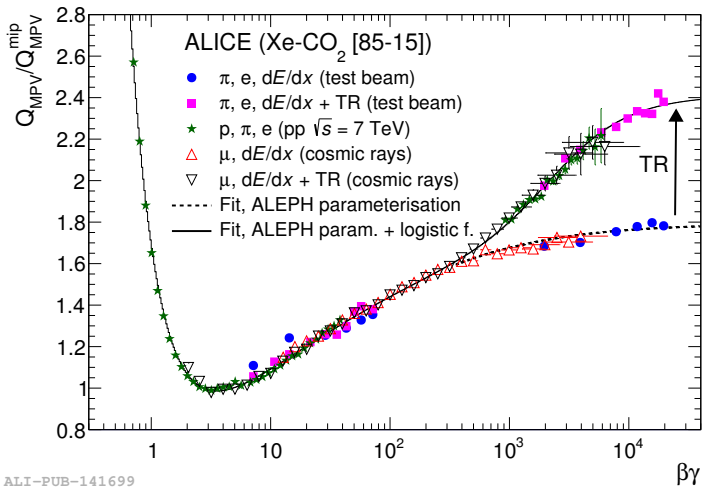

Figure 3.9: Deposited charge (Q_{MPV}) in units of minimum ionizing particles (mips) as function of $\beta\gamma$ measured with the ALICE TRD [75].

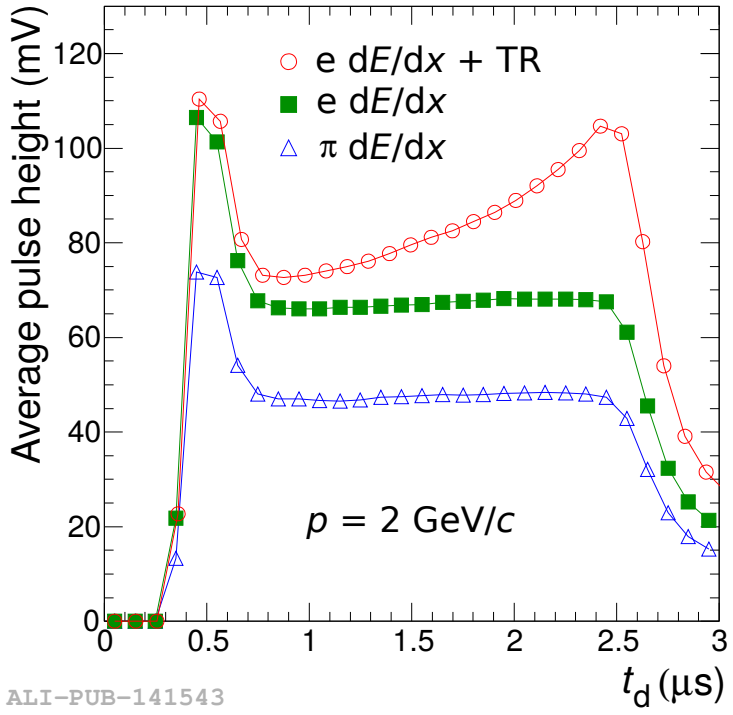

Figure 3.10: Measured mean signal shape of electrons w/ and w/o transition radiation and pions at $p = 2$ GeV/c recorded with prototype readout chambers of the ALICE TRD. [75]

to an increase of the electron avalanche, compared to a particle without transition radiation. Hence, the signal induced on the cathode pads is larger then the one estimated with the Bethe-Bloch equation. For the radiator of the ALICE TRD and a $p = 2$ GeV/c electron, the energy of transition radiation photons is typically in the range of 2-40 keV, with a significant peak of the distribution around 8 keV. The expected difference between tracks producing transition radiation and those only depositing charge according to the Bethe-Bloch equation in the readout chambers is clearly visible in figure 3.9. At $\beta\gamma \gtrsim 300$, transition radiation starts to modify the most probable deposited charge, adding almost one time the charge of a mip at $\beta\gamma \gtrsim 10^4$ in average (see 3.9). A special feature of the signal shape of the ALICE

TRD is visible in figure 3.10. Photons from transition radiation are dominantly absorbed after a very short distance in the gas volume, as indicated in figure 3.8. Thus, the electrons, created by the transition radiation, arrive towards the end of the signal creation at the amplification region, inducing a second bump about 2 μs after the initial rise of the signal. So-called "multi-dimensional" likelihood approaches, using up to seven separate time slices of the signal, utilize this feature for an improvement of the electron identification. With a signal from all six layers and a two dimensional likelihood approach at 90% electron efficiency, the TRD delivers a pion rejection factor of up to 410 [75].

Since the signal creation in the TRD and a preliminary PID and p_{T} estimation, based on the measured signal, does not need much time ($t_{\mathrm{decision}} < 6$ μs), the TRD can be used as readout trigger for a variety of observables. This includes charmonia decaying into electron-positron pairs, where a trigger on high p_{T} electrons/positrons is applied. Such a trigger configuration was part of pp and p−Pb data taking campaigns. However, due to the very limited Pb−Pb beam times, such a TRD trigger was not yet part of the ALICE trigger schemes during the recording of Pb−Pb collisions.

A potential contribution of the TRD to the global track reconstruction of the central barrel detectors is subject to ongoing developments. It is expected that, based on the segmented readout, the TRD is capable to improve the global tracking performance, especially in the upcoming data taking campaigns of Run3.

A full review of the ALICE TRD, describing the complete infrastructure and the detector itself, as well as a discussion of its performance, can be found in [75]. The analysis presented in chapter 6 introduces the TRD as additional PID detector to the J/ψ measurement and discusses its performance.

3.2.1d Time-Of-Flight detector (TOF)

The most outer detector of the central barrel, used in parts of the analyses presented in this thesis, is the Time-Of-Flight detector (TOF). It is built of Multi-gap Resistive-Plate Chambers (MRPCs), covering a pseudo-rapidity range of $|\eta| < 0.9$ and the full azimuthal angle, delivering a time-of-flight measurement with a resolution of about 50 ps. To measure the time-of-flight and hence the velocity of a particle, the time when a particle arrives at the TOF is put in correlation to the event time measured by the T0 detector (see 3.2.2a). Together with the measurement of the momentum, the estimation of the velocity allows to calculate the mass of a measured particle and thereby identify the particle. Due to the large mass difference between electrons and kaons, protons, or deuterons, the TOF performs well in reducing the corresponding contamination of electron samples up to $p \approx 2{-}4$ GeV/c, depending on the mass difference. In a similar procedure as introduced in equation 3.4 for the TPC, PID probabilities ($n\sigma^{\mathrm{TOF}}_{\mathrm{Particle}}$) in units of the time-of-flight measurement uncertainties are estimated and associated to the tracks [76].

3.2.2 Forward detectors

Important global event properties and trigger decisions are delivered by detectors in the forward direction. Thus, also for measurements at mid-rapidity those detectors are required, they provide for example the data for a precise collision-centrality estimation.

3.2.2a T0 detector

Placed at a radial distance of 6.5 cm from the beam axis and at +375 cm (T0-A) and -72.7 cm (T0-C) along the beam axis, respectively, the T0 detectors are installed to deliver precise timing information from the collisions and trigger the data readout. The time information is used as start time for the TOF measurement ($\Delta t \approx 50$ ps (r.m.s.)). Based on the measurement of the collision vertex, the T0 detectors trigger the data readout within 1.2 μs. Additionally, the T0 sends a wake-up signal in less then 900 ns after an interaction to the Front-End Electronics (FEE) of the TRD. To achieve these requirements two arrays of Cherenkov counters, equipped with fine-mesh dynode photomultiplier tubes, are used [65].

3.2.2b V0 detector

Covering the pseudo-rapidity ranges $5.1 \geq \eta \geq 2.8$ and $-1.7 \geq \eta \geq -3.7$, the V0 detector consists of two segmented scintillator counters (V0-A, V0-C). The V0 detector is part of several trigger schemes used for data taking with ALICE. A Minimum-Bias (MB) trigger concept, based on a logical "and" combination of a given minimum amount of hits in the V0-A, V0-C and the T0, was used for the recording of the data samples used for the analyses presented in this thesis. Increased requirements for the measured amplitudes in the V0-A and V0-C are applied for semi-central (CT1) and central trigger schemes. To estimate the collision centrality, the correlation between the measured V0 signal amplitudes and the track multiplicity of an event is used as input for Glauber model calculations [23, 77, 78]. Also the luminosity achieved in pp collisions can be measured with a precision of $\sim 10\%$ with the V0 detector. Due to the segmentation of the scintillators of the V0 detector, it is also possible to estimate the event-plane orientation with the signal amplitudes from the 32 individual counters [65].

3.2.2c Zero Degree Calorimeter (ZDC)

The Zero Degree Calorimeter (ZDC) is composed of three subdetectors. Located at $z = \pm 112.5$ m are the Zero degree Neutron calorimeter (ZN) and Zero degree Proton calorimeter (ZP), while the Zero degree Electromagnetic calorimeter (ZEM) is positioned at $z = 7.3$ m [66]. To measure the spectator neutrons, the ZN is placed between the two separate beam pipes. Since the trajectory of spectator protons is influenced by the magnets of the LHC, the ZP is placed with an offset on one side of the beam pipes. By measuring the amount of spectator nucleons, the ZDC is capable to estimate the collision centrality via:

$$E_{\mathrm{ZDC}} = E^{\mathrm{Beam}}_{\mathrm{per\ Nucleon}} \times N_{\mathrm{Spectators}} \tag{3.7}$$

$$N_{\mathrm{Participants}} = A - N_{\mathrm{Spectators}} = A - \frac{E_{\mathrm{ZDC}}}{E^{\mathrm{Beam}}_{\mathrm{per\ Nucleon}}}. \tag{3.8}$$

However, in the case of very peripheral collisions, the spectator nucleons will most likely be clustered in large fragments with Z/A ratios compatible to those of lead ions. Hence, those fragments will stay in the beam pipes due to the magnetic fields and far too little energy will be measured by the ZN or ZP. To be able to separate those very peripheral events from very central collisions, where also almost no spectators are measured by the ZN or ZP, the ZEM is installed on both sides of the beam pipe. Based on the fact that the energy of particles emitted in forward rapidity increases with the collision centrality, the measurement of the total

energy enables to distinguish between very central and peripheral collisions. This information is for example also used to reject background and pileup events.

3.2.3 Detector summary

In summary, the recording of a MB event is initialized by a trigger signal from the combination of the T0 and the V0 accepted by the ZDC. Indicating that all four detectors, i.e. T0, V0-A, V0-C and ZDC, observed a heavy-ion collision leading to a valid physics event. For the estimation of the collision's centrality, the signal amplitude in the V0 detector is correlated to the track multiplicity and thus the collision centrality via Glauber model calculations. The particle trajectories are reconstructed with the ITS and the TPC. To identify the particles correlated to the measured trajectories, the TPC, TOF, ITS and TRD deliver information. For the J/ψ measurement at mid-rapidity, the main PID detector is the TPC. In the analysis presented in chapter 5, additional information for the rejection of hadrons is used from the TOF. A study of the potential of the TRD to improve the electron identification for J/ψ measurements in Pb−Pb collisions is discussed in 6.

3.3 Analysis framework

AliRoot is the offline data analysis framework of the ALICE experiment [65]. Offline detector calibration, data simulation, event and track reconstruction, as well as specific physics analyses are performed with the AliRoot software suite. It is based on C++ and the "ROOT" framework [79, 80], which itself was developed for the storage, analysis and visualization of large amounts of data. The central computing resource available within ALICE is the Worldwide LHC Computing Grid (WLCG) [81]. It was developed and installed to provide computing facilities for the LHC experiments. Worldwide distributed computing centers of different sizes are artificially clustered to a "super computer". To enable user access to the WLCG the AliEn system has been developed [82].

The analysis workflow of AliRoot employs so-called "analysis tasks" [83]. Within AliRoot, a base analysis task class is provided, which handles basic functionalities, like event-loops accessing the events of a data storage object. Users configure analysis specific analysis tasks, derived from the base class, containing the analysis specific data handling, e.g. event and track selection. This approach has the advantage that the main I/O operations are identical for all analyses. The Lightweight Environment for Grid Operators (LEGO) train system [84] utilizes this advantage as it allows to bundle analysis tasks accessing the same data. Hence, analysis jobs set up with the LEGO train system allow several users to access analysis data with only one read operation of the data. Additional reduction of the amount of data reading operations is done by a preselection of the data. Events and tracks rejected by selection criteria, looser then those of the analysis itself, are excluded from the data used for the analysis. Also, information not needed for the analysis is excluded from the data. These two procedures reduce the storage size of the analyzed data by about a factor $\sim$ 500; the full data sample used in this analysis is reduced to about 250 GB and stored in so-called "nanoAODs".

To ensure the reproducibility of all results of data analyses, the main parts of the analysis code are supposed to be part of AliRoot. AliRoot and its components are stored and organized with the versioning system "git" [85]. The code for analyses

investigating J/ψ production in the dielectron channel is collected in the "dielectron" framework [86].

4 Measurement of J/ψ in Pb−Pb collisions with ALICE

The ALICE experiment is capable to measure J/ψ at mid-rapidity in the J/$\psi \rightarrow e^+ + e^-$ decay channel. In this chapter, the principles of this measurement with ALICE, as well as the data sample, on which the analyses presented in this thesis are performed on, will be discussed. This includes:

- a review of the collision centrality estimation, based on charged track multiplicities and Glauber modeling;
- a discussion of the event and track selection criteria;
- an explanation of the methods used for the J/ψ signal extraction.

4.1 LHC's 2015 heavy-ion run

In the end of 2015, the first heavy-ion data taking period of the LHC with Pb−Pb collisions at $\sqrt{s_{\mathrm{NN}}} = 5.02$ TeV collision energy took place, within the ALICE collaboration marked as "LHC15o". An integrated nucleon-pair luminosity ($\mathcal{L}$) of $\mathcal{L} \approx 19\ \mathrm{pb}^{-1}$ has been achieved at interaction point 2 - position of the ALICE experiment - during 18 days of physics data taking [87]. This corresponds to 154,774,896 MB interactions recorded with ALICE, distributed over 194 data taking runs. As mentioned in section 3.2.2b, the MB trigger, for this period, was defined by a combination of signals in the V0-A, V0-C and T0 detector. However, the event sample as selected with the given MB trigger condition, still contains events not usable for physics analyses. After an additional event selection, discussed in section 4.2, the data sample contains about $90 \cdot 10^6$ minimum bias events. Based on a MB event cross-section of $\sigma = 4.72$ b, as quoted in [88], this number of MB events corresponds to an integrated luminosity of $\mathcal{L}_{\mathrm{int}} \approx 17\ \mu\mathrm{b}^{-1}$. A run-by-run quality assurance (QA) ensures the quality of the data bundled in different runs and investigate whether the data recorded in the various runs can be merged or not. It compares mid-level quantities of the analyses, e.g. the event-plane resolution. More details and results on the performed QA checks will be given in the analysis specific chapters.

Several ***Monte Carlo (MC)*** simulations were prepared for the LHC15o data sample. For the analyses in this thesis two productions were used, a MB production ("LHC16g1") and one production with injected J/ψ signals ("LHC16j1"). The latter one has the advantage, that, even though it contains only 1.6 M events, it allows a statistically precise analysis of the behavior of J/ψ in the simulations.

4.2 Event selection

Every time the signal amplitudes of the V0-A, V0-C and the T0 exceed given thresholds in coincidence, an event is recorded. These events can contain pileup contaminating the event and influencing the properties of the track sample related to the

event. The so-called ***physics selection*** identifies, in a first offline selection step, events contaminated by pileup or of low reconstruction quality and removes them from the event sample. For the given data sample, the physics selection applies an offline reevaluation of the information from the V0 detectors. This reevaluation is based on a detailed analysis of the raw data from the V0 detectors. The criteria for the signal amplitudes and the time correlation of the signals of the V0-A and V0-C signals are revisited and adjusted in comparison to the online trigger configuration. If the three ZDC subdetectors are available, a rejection of pileup events, based on the relative time information of them, is applied. To reject events with a bad quality in terms of the TPC data reconstruction quality, the actual high voltage of the readout chambers is compared with the nominal values.

After the physics selection is applied, the events have to pass additional analysis specific selection criteria.

Event vertex: A successful reconstruction of an event vertex, with at least one global track as contributor, is required. Additionally, the position of the measured vertex has to be within ±10 cm of the center of ALICE along the beam axis ($z_{vtx} = \pm 10$ cm), for an event to be selected. This requirement ensures a symmetric detector acceptance and hence builds the foundation for a symmetric track reconstruction quality.

Event-plane: Since the detector acceptance and performance is not perfectly symmetric over the full azimuth, a successfully reconstructed event-plane (see section 4.4) is required for a correct background estimation via the mixed-event technique (see section 4.7.1) in every event.

Collision centrality: The uncertainties on the measurement of the collision centrality rise strongly for very peripheral collisions. To avoid inconveniences due to these uncertainties, only collisions with a measured centrality in the range of the 90% most central collisions are part of the analyzed event sample. Additional collision-centrality selections are applied for the analysis of the J/ψ elliptic flow and will be discussed in chapter 5.

Out-of-bunch pileup: Due to the high bunch-crossing rates during the 2015 heavy-ion run a not ignorable amount of out-of-bunch pileup occurred. Detectors with a short signal collection time, like the ITS or the V0 detectors, are able to distinguish between tracks from the actual event and those from out-of-bunch pileup. However, in the TPC the signal collection is long enough, that particles emerging from out-of-bunch pileup can appear in the same track sample as particles from the physics event. These tracks are not part of the global track sample, since the ITS rejects them. But as they strongly influence the PID measurement of the TPC, events highly contaminated by out-of-bunch pileup are rejected. This rejection is based on the comparison of the measured track multiplicity in the V0 detectors, which is fast enough to separate the tracks correlated to the event from those of the out-of-bunch collisions, and the track multiplicity measured by the TPC. Figure 4.1 illustrates the correlation between the amplitudes of the V0 detectors (x-axis) measured in an event and the number of tracks registered in the TPC in the same event. The color scale on the z-axis represents the fraction of the total number of events. Most central collisions correspond to the highest V0 amplitudes $\mathrm{V0M_{amp.}} \approx 35,000$. Without out-of-bunch pileup such a collision leads to $N_{\mathrm{tracks}}^{\mathrm{TPC}} \approx 12,000$, indicated by the upper

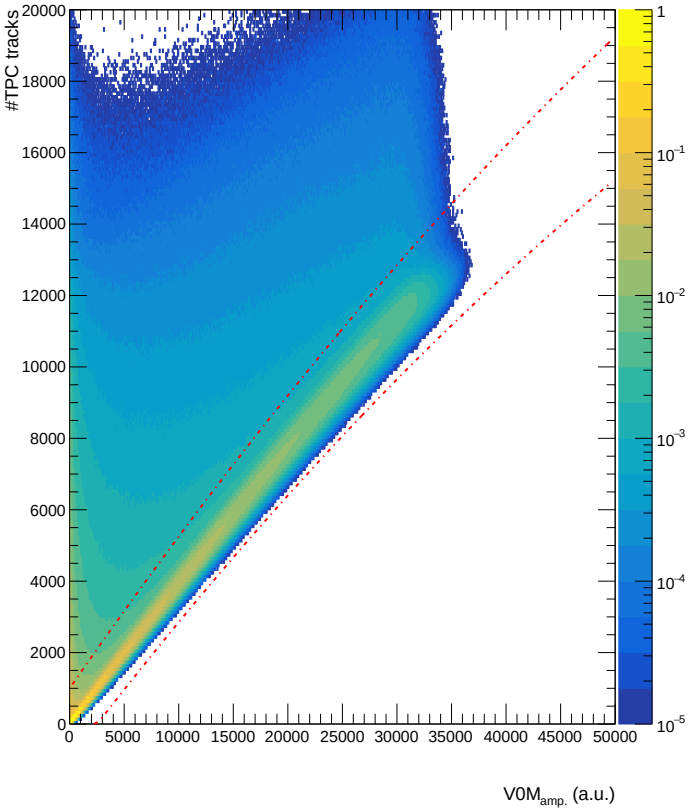

Figure 4.1: Amount of TPC tracks correlated to an event as function of the amplitude of the V0 detectors in the same event. The red dash-dotted lines represent the selection criteria. All events, below the bottom line or above the upper line are rejected.

end of the highly populated band between the dash-dotted lines. Thus, events in which the TPC registered about 12,000 additional tracks, when compared to the band of events without out-of-bunch pileup, correspond to an increment in the track density in the TPC due to out-of-bunch pileup of an additional full central collision. Obviously such an increase of the track density in the TPC, has a strong influence on the $\mathrm{d}E/\mathrm{d}x$ measurement in the TPC. Represented by the dash-dotted red lines are the selection criteria used to reject those events. All events above the top line or below the bottom line, respectively, are excluded from further analysis steps. The mathematical functions, given in equations 4.1 and 4.2, corresponding to these criteria, are tuned on data samples with a low interaction rate and thus almost no pileup occurrences.

$$f_{\mathrm{up}}(x = \mathrm{V0M_{amp.}}) = 10^3 + 0.44 \cdot x + -1.5 \cdot 10^{-6} \cdot x^2 \tag{4.1}$$

$$f_{\mathrm{low}}(x = \mathrm{V0M_{amp.}}) = -10^3 + 0.4 \cdot x + -1.5 \cdot 10^{-6} \cdot x^2 \tag{4.2}$$

As a remark: for the analysis presented in chapter 5, a predecessor of the selection criteria discussed above was applied, since at the actual time of the analysis not all values, utilized in the criteria, were available in the data prepared for analyses. However, an integrity check of the correlation between the used quantities in both versions of the pileup rejection was done and did not show any conspicuous behavior.

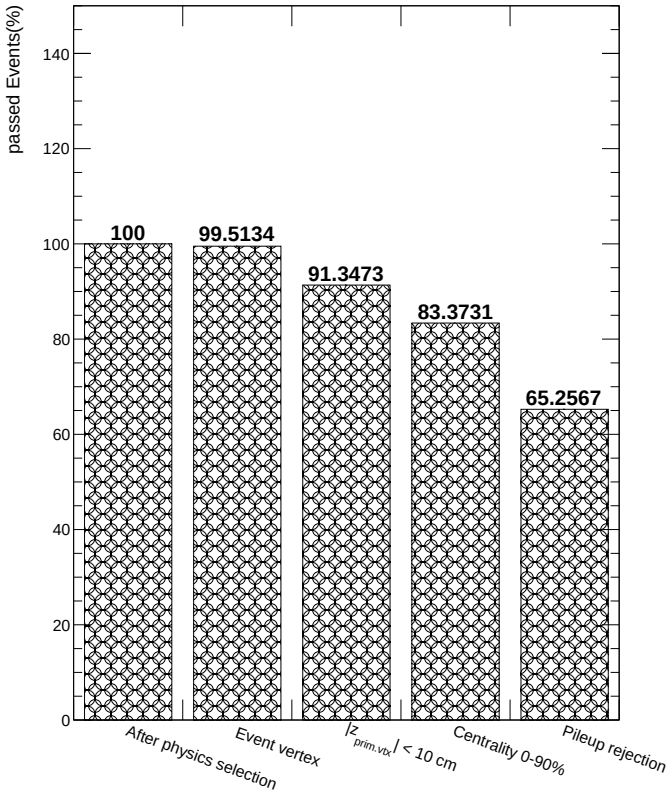

Figure 4.2: Percentage of events passing the selection criteria. Every step represents a combination of the criterion indicated by the label, and the criteria of the previous steps.

Influence on the number of events in the data sample: The percentage of events passing the selection criteria is depicted in 4.2; the given values represent the percentage of accepted events from all events. Each step represents the cumulative action of the indicated selection criterion and all previous criteria. As expected for a well performing physics selection, almost all events have a reconstructed event vertex with at least one contributor. Approximately 8% of events are rejected, since they do not fulfill the condition of $|z_{vtx}| < \pm 10$ cm. In the next step, the 10% most peripheral events are excluded. From this exclusion, one would intuitively expect a further reduction by 10% of the event sample. However, the previously applied selection criteria seem to bias the centrality distribution by rejecting more events in the range of 90%-100%, than in other centrality ranges. Nevertheless, for the analyses presented in this thesis, which are performed on the remaining event sample, this should not represent an issue due to the small size of the bias. The pileup selection criterion rejects almost 20% of the events, although they passed all other criteria. Currently some effort is made to reestablish the usability of the rejected events via a special offline calibration. However, this will unfortunately still take some time and is not available on the time scales of this thesis. Hence, the only option for the analyses presented in this thesis was to reject these events, even-though they represent a statistically relevant amount.

4.3 Collision centrality estimation

The collision centrality ($\mathcal{C}$) is an important information required for several stages of the analyses presented in this thesis. It provides access to an estimation of the geometrical volume of the fireball. Within ALICE a common framework for the centrality estimation is established, which classifies the centrality of an event based on the track multiplicities [89]. In detail, all centrality values presented in this thesis are calculated based on the measurement of the amplitudes in the V0 detectors. The

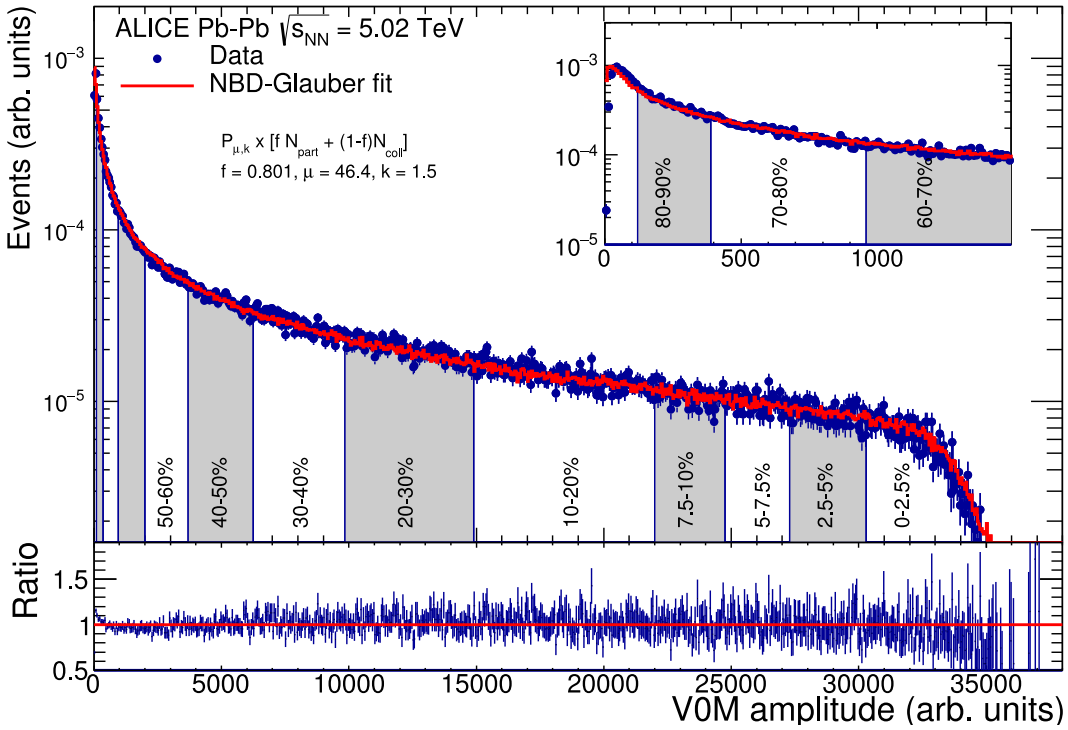

Figure 4.3: Number of events as function of the measured V0 amplitude (blue circles), with the corresponding centrality class indicated. The red line corresponds to the Glauber Monte Carlo approximation based on a negative binomial distribution [89].

approximation of the event distribution as function of the measured V0 amplitude with a Glauber Monte Carlo calculation allows the estimation of $\langle N_{\mathrm{part}} \rangle$ and $\langle N_{\mathrm{coll}} \rangle$ for a given V0 amplitude. Illustrated in figure 4.3 is the number of events as function of the V0 amplitude (blue circles), together with the approximation by the utilized Glauber Monte Carlo model (red line). Indicated by vertical lines are the actual centrality classes as defined by the given V0 amplitudes. In the bottom part of the figure the ratio of the measurement and the model is shown. Only for the most central events ($\mathrm{V0_{amp.}} \gtrsim 32,500$) a slight deviation appears. In addition to $\langle N_{\mathrm{part}} \rangle$ and $\langle N_{\mathrm{coll}} \rangle$, the Glauber model provides an estimate for the impact parameter (b) of the collision. It represents the distance between the centers of both lead ions. An illustration of N_{part} and b is sketched in figure 4.4. Based on b, an approximation of the eccentricity of the fireball can be made.

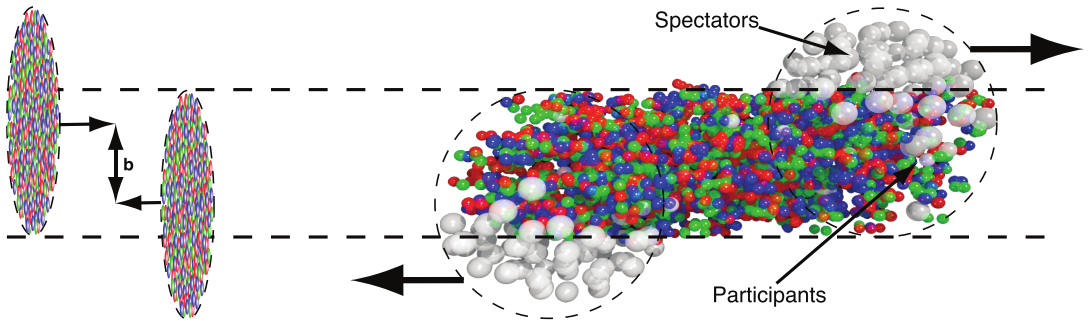

Figure 4.4: Sketch of a heavy-ion collision, as approximated by the Ultrarelativistic Quantum Molecular Dynamics (UrQMD) model [90, 91]. The left side represents the status before the collision with the impact parameter (b) indicated. On the right side the status after the initial collision is given, with all participating nucleons (N_{part}) marked with colors. Figure originates from [92] adopted in [93].

4.4 Event-plane angle estimation

4.4.1 Ansatz

The overlap of the colliding nuclei and hence the initial geometrical shape of the fireball, can be approximated by an ellipse, with its eccentricity depending on the impact parameter. In the case of a vanishing impact parameter the overlap is represented by an ellipse with equal short and long axis, i.e. a circle. Figure 4.5 illustrates

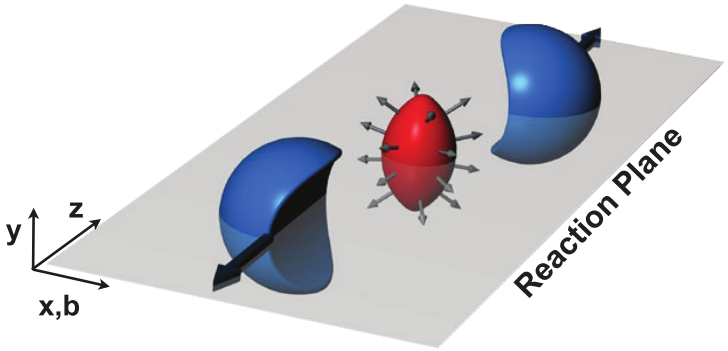

Figure 4.5: Sketch of a heavy-ion collision with a non-vanishing impact parameter [93].

the process of two colliding nuclei with $b > 0$, resulting in an almond shaped fireball [93]. During the evolution of the collision, the initial geometric anisotropy translates into an anisotropy in the phase space during the expansion of the fireball. For collisions in the energy regime of the LHC, an increase of the hydrodynamic pressure along the long axis towards the center of the ellipse is expected. This pressure gradient induces a higher particle flow in the direction of the short axis compared to the direction of the long axis. A simulation of the hydrodynamical evolution of the energy density in a heavy-ion collision with $b = 7$ fm in the x-y plane as function of the time is shown in figure 4.6 [93, 94]. As discussed before, the initial geometric anisotropy leads to a more pronounced expansion of the energy density along the short axis of the initial ellipse. Based on this phenomenon an estimate for the ***reaction plane*** can be made, which defines a reference angle for the azimuthal orientation of the collision. The reaction plane represents the plane spanned by the

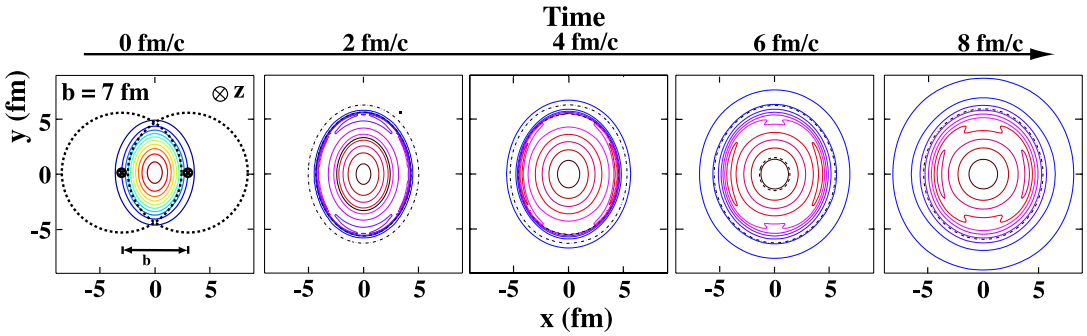

Figure 4.6: Evolution of the energy density (color-coded z-axis) in the x-y plane of a non-central heavy-ion collision as function of the time [93, 94].

impact parameter and the beam axis, as sketched in figure 4.5. Unfortunately, the space coordinates of the impact parameter are not directly accessible. To estimate the azimuthal orientation of the reaction plane (Ψ_{RP}), the so-called azimuthal event-plane angle ($\Psi_{\mathrm{ep.}}$) is calculated from the measurement of the event flow vector ($\mathbf{Q}_n$) [95]:

$$\mathbf{Q}_n = \begin{pmatrix} \sum_i \cos n\phi_i \\ \sum_i \sin n\phi_i \end{pmatrix}, \tag{4.3}$$

$$\Psi_{n,\mathrm{ep}} = \frac{1}{n} \arctan\left(\frac{Q_{n,\mathrm{y}}}{Q_{n,\mathrm{x}}}\right). \tag{4.4}$$

In equation 4.3 and 4.4, n represents the harmonic of $\mathbf{Q}_n$, for an elliptic flow measurement $n = 2$. The particles (i) used for the summation of azimuthal orientations (ϕ_i), correspond to a subsample of all particles from the given event. For example, particles with a large p_{T}, e.g. correlated to a jet occurrence, are excluded from those subsamples, since they probably were not affected by the pressure gradient of the energy density and hence, do not carry information about the azimuthal reaction-plane orientation. The subsamples are composed of all particles, which fulfill the following requirements:

$$\begin{aligned} |dca_{\mathrm{xy}}| &< 0.3 \text{ cm}, \\ |dca_{\mathrm{z}}| &< 0.3 \text{ cm}, \\ 70 \leq N^{\mathrm{cls}}_{\mathrm{TPC}} &\leq 159, \\ 0.2 \leq \frac{\chi^2_{\mathrm{TPC}}}{N^{\mathrm{cls}}_{\mathrm{TPC}}} &\leq 4, \\ |\eta| &\leq 0.8, \\ 0.2 \leq p_{\mathrm{T}} &\leq 5 \text{ GeV}/c. \end{aligned} \tag{4.5}$$

In a second iteration, all J/ψ electron candidates are recursively excluded from the event-plane calculation to avoid autocorrelations. The measured $\mathbf{Q}_n$ vector has to be corrected for non-uniformities in the detector efficiencies, to ensure a flat and thus unbiased $\Psi_{\mathrm{ep.}}$ distribution over the complete azimuth. Those corrections are performed with the "QnCorrections framework"[1], it applies a calibration of the $\mathbf{Q}_n$ according to the procedures proposed by Selyuzhenkov and Voloshin in [95] and is integrated into AliRoot. The following section discusses the correction procedures and the resulting event-plane distributions.

[1] https://github.com/FlowCorrections/FlowVectorCorrections

4.4.2 Calibration

Several calibration steps have to be performed in order to minimize the bias of detector inefficiencies on the azimuthal event-plane angle estimation. A flat event-plane distribution ensures an unbiased measurement of the elliptic flow, despite anisotropic detector efficiencies along the azimuth.

Since the $\Psi_{\text{ep.}}$ estimation with the V0 detectors is based on the signal amplitude distribution over the detector, anisotropies in the single-channel response introduce biases to the event-plane distribution. Hence, the first calibration step for the V0-A and V0-C is the equalization of the single-channel gain. Within this first calibration step two iterative corrections are applied:

$$\begin{aligned}\text{V0}'_{\text{amp.}}(\mathcal{C}) =& \frac{\text{V0}_{\text{amp.}}(\mathcal{C})}{\langle \text{V0}_{\text{amp.}}(\mathcal{C})\rangle},\\ \text{V0}''_{\text{amp.}}(\mathcal{C}) =& 1 + \frac{\text{V0}_{\text{amp.}}(\mathcal{C})' - \langle \text{V0}_{\text{amp.}}(\mathcal{C})'\rangle}{\sigma_{\text{V0}_{\text{amp.}}(\mathcal{C})'}}.\end{aligned}$$

For the TPC no gain equalization procedure is required, because the $\Psi_{\text{ep.}}$ estimation with the TPC is based on the reconstructed track sample. After the gain equalization step, the calibration of the event plane estimation is based on the rewritten definition of the average event flow vector, which takes potential detector inefficiencies along the azimuthal angle into account:

$$\langle \mathbf{Q}_n \rangle_{\Psi_{\text{RP}}} = \begin{pmatrix} \langle X_{\Psi_{\text{RP}}}\rangle = \bar{X}_n + A^{+}_{2n}(\cos(n\Psi_{\text{RP}}) + \Lambda^{s+}_{2n}\sin(n\Psi_{\text{RP}})) \\ \langle Y_{\Psi_{\text{RP}}}\rangle = \bar{Y}_n + A^{-}_{2n}(\sin(n\Psi_{\text{RP}}) + \Lambda^{s-}_{2n}\cos(n\Psi_{\text{RP}})) \end{pmatrix} \tag{4.6}$$

Here the index "Ψ_{RP}" denotes that $\langle \mathbf{Q}_n \rangle$ corresponds to the hypothetical average of the $\mathbf{Q}_n$ for a fixed reaction plane angle (Ψ_{RP}). The correction coefficients $A^{\pm}_{2n}$ and $\Lambda^{s\pm}_{2n}$ represent:

$$A^{\pm}_{2n} = 1 \pm \langle X_{2n}\rangle, \tag{4.7}$$

$$\Lambda^{s\pm}_{2n} = \frac{\langle Y_{2n}\rangle}{A^{\pm}_{2n}}. \tag{4.8}$$

In the case of a perfect detector without inefficiencies these two coefficients vanish. For the TPC, the acceptance coefficients ($A^{\pm}_{2n}$) and the smallness parameters ($\Lambda^{s\pm}_{2n}$) can be calculated directly from the measured $\mathbf{Q}_n$ distributions. Due to the high segmentation of the V0-A and V0-C, it is not possible to directly calculate the coefficients in a similar manner as for the TPC. However, they can be estimated with the sub-event method, utilizing the TPC $\mathbf{Q}_n$ after its calibration and the $\mathbf{Q}_n$ of the V0-A and V0-C. Symmetry implies that:

$$A^{+}_{2n}\Lambda^{s+}_{2n} = A^{-}_{2n}\Lambda^{s-}_{2n}. \tag{4.9}$$

Together with the following equations based on the sub-event technique:

$$\begin{aligned} 8\langle X^a_n X^b_n\rangle &= (A^{+}_{2n})^2(1 + (\Lambda^{s+}_{2n})^2),\\ 8\langle Y^a_n Y^b_n\rangle &= (A^{-}_{2n})^2(1 + (\Lambda^{s-}_{2n})^2),\\ 8\langle X^a_n Y^b_n\rangle &= A^{+}_{2n}A^{-}_{2n}(\Lambda^{s+}_{2n} + \Lambda^{s-}_{2n}), \end{aligned} \tag{4.10}$$

the correction coefficients can be estimated via:

$$\begin{aligned} A_{2n}^{B-} &= \frac{\sqrt{2\langle X_n^a X_n^b\rangle}\langle X_n^a X_n^c\rangle}{\langle X_n^a X_n^c\rangle\langle X_n^b X_n^c\rangle + \langle X_n^a Y_n^c\rangle\langle X_n^b Y_n^c\rangle}, \\ \Lambda_{2n}^{B+} &= \frac{\langle X_{2n}^a Y_{2n}^b\rangle}{\langle X_{2n}^a X_{2n}^b\rangle}, \\ \Lambda_{2n}^{B-} &= \frac{\langle Y_{2n}^a X_{2n}^b\rangle}{\langle Y_{2n}^a Y_{2n}^b\rangle}. \end{aligned} \tag{4.11}$$

All coefficients and calibration steps are calculated and applied in dependence of the collision centrality and the position of the collision vertex along the beam-axis. In the first applied calibration step, after the gain equalization of the V0 detectors, the distributions of the event flow vectors are re-centered around zero:

$$\mathbf{Q}'_n = \mathbf{Q}_n - \langle \mathbf{Q}_n \rangle. \tag{4.12}$$

The re-centering step shifts the X_n and Y_n component of $\mathbf{Q}_n$ with a constant value, based on the offset from zero of the input distributions. In the next step, the width of the now centered distributions is "equalized", to ensure that it is independent of the collision centrality and the vertex position:

$$\mathbf{Q}''_n = \mathbf{Q}'_n / \sigma_{\mathbf{Q}_n}. \tag{4.13}$$

The alignment correction handles an effective misalignment, visible in the cross terms between the X- and Y-component of different event-plane estimators:

$$\langle X_n^a Y_n^b\rangle \neq \langle X_n^b Y_n^a\rangle. \tag{4.14}$$

To correct for this effect, $\mathbf{Q}_n$ is rotated:

$$\mathbf{Q}'''_n = \mathbf{Q}''_n + \mathbf{Q}''_{n,\,\phi}. \tag{4.15}$$

After these three calibration steps, the higher order "twist" and "rescale" corrections are applied. They are based on the mixed terms between the X- and Y-component, visible in the acceptance coefficient 4.7 and the smallness parameters 4.8. The twist correction accounts for these mixed terms with a diagonalization procedure:

$$\langle X_n''''\rangle_\Psi = \frac{\langle X_n'''\rangle_\Psi - \Lambda_{2n}^{s-}\langle Y_n'''\rangle_\Psi}{1 - \Lambda_{2n}^{s+}\Lambda_{2n}^{s-}}, \tag{4.16}$$

$$\langle Y_n''''\rangle_\Psi = \frac{\langle Y_n'''\rangle_\Psi - \Lambda_{2n}^{s-}\langle X_n'''\rangle_\Psi}{1 - \Lambda_{2n}^{s+}\Lambda_{2n}^{s-}}. \tag{4.17}$$

Finally, the following equation describes the rescale calibration step, which scales the $\mathbf{Q}_n$ components according to the acceptance coefficient:

$$\langle X_n'''''\rangle_\Psi = \frac{\langle X_n''''\rangle_\Psi}{A_{2n}^{+}}, \tag{4.18}$$

$$\langle Y_n'''''\rangle_\Psi = \frac{\langle Y_n''''\rangle_\Psi}{A_{2n}^{-}}. \tag{4.19}$$

As mentioned in the previous section, the corrections are applied within the *Qn-Corrections framework*, which utilizes the techniques presented in [95]. The review

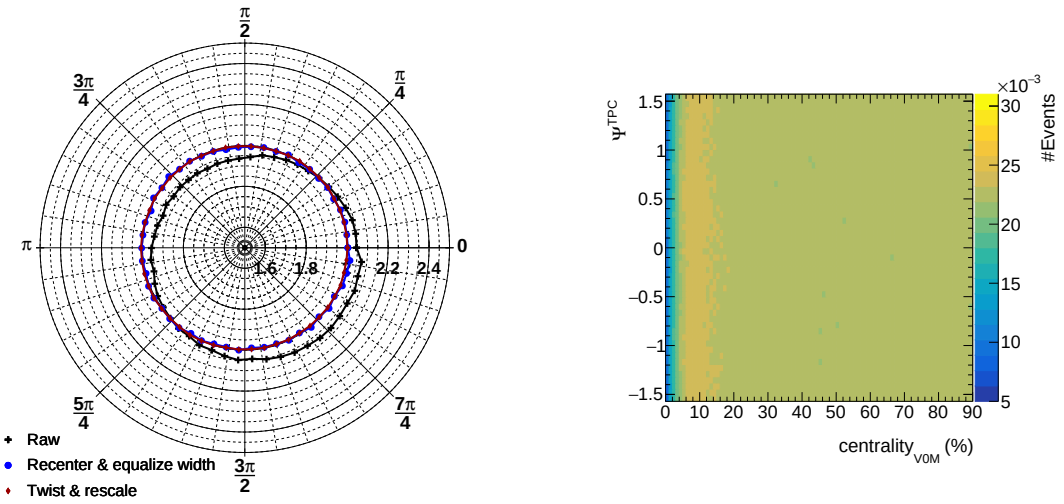

Figure 4.7: Left panel: Measured TPC event-plane angle distribution for different calibration passes. The polar angle corresponds to the measured event-plane angle and the radial axis gives the event probability. Right panel: Fully calibrated TPC event-plane angle distributions as function of the event centrality.

by Selyuzhenkov and Voloshin also contains a detailed discussion of the theoretical principles, on which the calibration procedures are based.

In figure 4.7 a comparison between the azimuthal event-plane angle estimation with the TPC ($\Psi_{\text{ep.}}^{\text{TPC}}$) before and after the calibration is depicted (left panel), and the distribution of $\Psi_{\text{ep.}}^{\text{TPC}}$ as function of the collision centrality after the calibration is given (right panel). The left panel of figure 4.7 demonstrates the improvement of the $\Psi_{\text{ep.}}^{\text{TPC}}$ distribution with each calibration step. It shows $\Psi_{\text{ep.}}^{\text{TPC}}$ in polar direction and the percentage of the event probability in radial direction. Only minimal anisotropies below the per mill level are observed after the second calibration step. As the right panel of figure 4.7 depicts, the distribution of $\Psi_{\text{ep.}}^{\text{TPC}}$ (y-axis) is well calibrated for all event centralities (x-axis). A comparison of the fully calibrated event-plane angle distributions measured with the TPC and the V0 detectors is presented in figure 4.8. As in figure 4.7, the polar angle corresponds to the measured $\Psi_{\text{ep.}}$ and the radial axis gives the probability of a measurement with the given azimuthal event-plane angle. Unfortunately, the distributions of the azimuthal event-plane angle estimation with the V0A ($\Psi_{\text{ep.}}^{\text{V0A}}$) and azimuthal event-plane angle estimation with the V0C ($\Psi_{\text{ep.}}^{\text{V0C}}$) are not as uniform as the one of $\Psi_{\text{ep.}}^{\text{TPC}}$. The distributions fluctuate between a probability of 1.8% and 2.2% for a given azimuthal event-plane angle, what corresponds to a maximum variation of $\sim 20\%$. However, the deviations are of a clearly visible $n \approx 4$ harmonic and thus compensate themself almost completely in a elliptic flow (v_2) measurement.

4.4.3 Resolution

The measurement of the elliptic flow of J/ψ ($v_2^{\text{J}/\psi}$) is based on the measurement of the strength of the correlation between the azimuthal distribution of the measured J/ψ and $\Psi_{\text{ep.}}$. A resolution below unity of the $\Psi_{\text{ep.}}$ estimation weakens the measured correlation compared to the true correlation. Thus, a correction for the resolution of

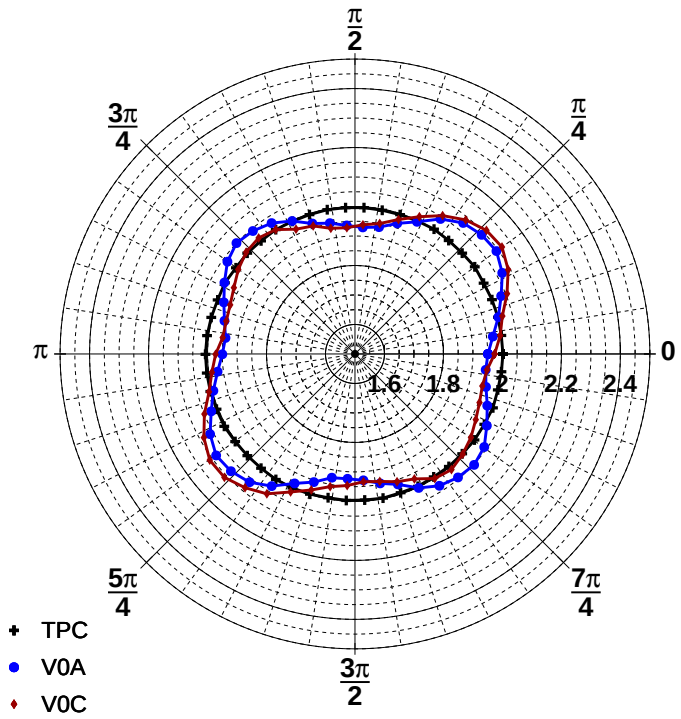

Figure 4.8: Azimuthal event-plane angle distribution measured with the TPC (black crosses), V0A (blue circles) and the V0C (red diamonds), in the final calibration step. The polar angle corresponds to the measured event-plane angle and the radial axis gives the event probability.

the event-plane angle measurement has to be applied. To determine the resolution of the $\Psi_{\text{ep.}}$ measurement a data driven approach, analyzing the correlation of event planes estimated with independent detectors, is utilized [96]. In this case, three independent measurements are compared:

$$R_n^A = \sqrt{\frac{\langle \cos(n(\Psi_n^A - \Psi_n^B))\rangle \langle \cos(n(\Psi_n^A - \Psi_n^C))\rangle}{\langle \cos(n(\Psi_n^B - \Psi_n^C))\rangle}}. \tag{4.20}$$

While the nominator in equation 4.20 represents the deviations of the detector of which the resolution is calculated, the denominator corrects for the uncertainties of the two reference detectors. The resolution of the second-order event-plane measurement with the TPC, V0A and the V0C as function of the event centrality is given in figure 4.9. As expected, a clear dependence on the collision centrality is observed. While for central events no initial anisotropy from the collision shape exists, for the more peripheral events ($\mathcal{C} > 60\%$) fluctuations in the initial collision geometry of higher orders become more relevant and thereby reduce the precision of the second-order event-plane measurement. As correction factor for the $v_2^{\text{J}/\psi}$ measurement a weighted average of the resolution in the utilized event-centrality range is used. Measurements at forward rapidity provide a high resolution J/ψ yield distribution as function of the collision centrality. This distribution is utilized to weight the resolutions, when the averages are calculated, resulting in the following factors:

$$R_2^{\text{TPC}} = 0.88, \tag{4.21}$$

$$R_2^{\text{V0A}} = 0.68, \tag{4.22}$$

$$R_2^{\text{V0C}} = 0.77. \tag{4.23}$$

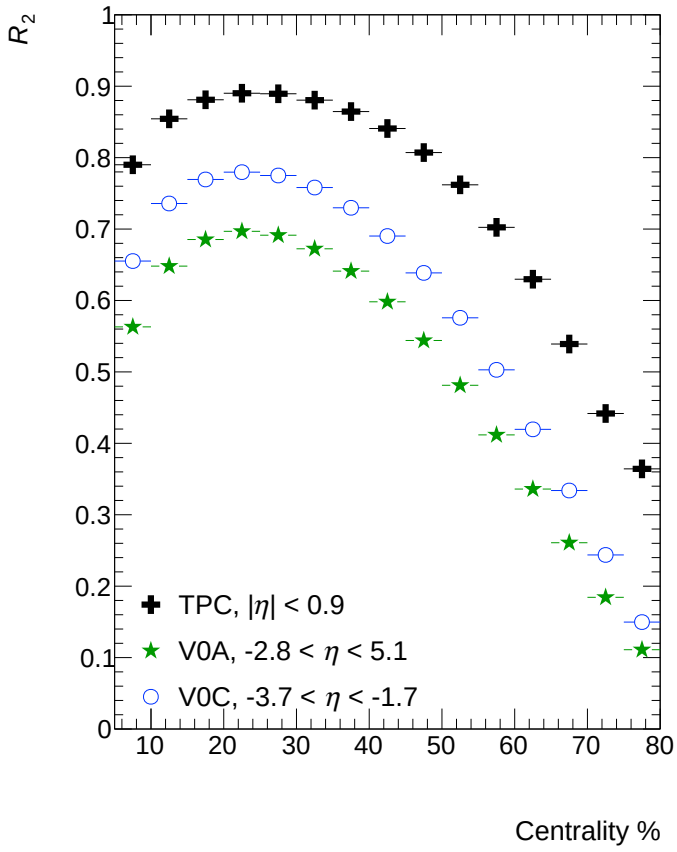

Figure 4.9: Resolution of the second-order event-plane determination as function of the event centrality.

A run-by-run quality-assurance analysis based on the resolution of the event-plane determination with the TPC was done for the utilized data sample. In order to ensure a comparable quality of the $\Psi_{\text{ep.}}$ estimation in all analyzed events, runs in which large deviations of the resolution compared to the overall average have been observed are excluded from further analysis steps.

4.5 Track selection

Several criteria are applied in the selection process of electron and positron track candidates for the J/ψ reconstruction. These criteria are supposed to reject tracks outside of the kinematic range of tracks resulting from J/ψ-decays and ensure the reconstruction quality of the remaining track candidates, such that the kinematic information, as well as the PID information, is reliable.

Transverse momentum: Based on the kinematics of J/$\psi \to e^+e^-$ decays and the p_{T}-distribution of potential background tracks, the following track-p_{T} selection is applied:

$$p_{\text{T}} \geq 1 \text{ GeV}/c. \tag{4.24}$$

The left panel of figure 4.10 depicts the p_{T} distributions of the track sample before (black crosses) and after (blue circles) the track selection. In addition, the p_{T}

distribution of electrons from $J/\psi \rightarrow e^+e^-$ decays estimated with Monte Carlo simulations (red diamonds) is shown. Below 1 GeV/c the amount of electrons originating from $J/\psi \rightarrow e^+e^-$ decreases, while the amount of electrons from other sources still increases (see for example [97]). As a remark, the p_T distribution of the simulated J/ψ spectrum is not completely realistic. However, this does not effect the drop of the single electron distribution below $p_T \approx 1.75$ GeV/c. After the application of the track selection the distribution is steeper, indicating that more tracks at higher p_T are removed. This is a result of the fact, that the track curvature decreases with p_T and in average a reduced curvature leads to less clusters in the TPC. Stronger bend tracks pass more different areas of the TPC readout chambers, whereas straighter tracks can be "stuck" in "dead zones" without good reconstruction capabilities.

Pseudorapidity range: To ensure a good track reconstruction, the track itself has to be within the pseudorapidity (η) range of all utilized detectors. Thus, all track candidates have to fulfill

$$|\eta| \leq 0.9. \tag{4.25}$$

Number of clusters in the TPC: As baseline for a good track reconstruction with the TPC, a minimum amount of track-correlated charge clusters along the trajectory is required:

$$N_{\mathrm{TPC}}^{\mathrm{cls}} > 70. \tag{4.26}$$

The distributions of $N_{\mathrm{TPC}}^{\mathrm{cls}}$ measured before (black crosses) and after (blue circles) the track selection, as well as the distribution for electrons from $J/\psi \rightarrow e^+e^-$ decays estimated with Monte Carlo simulations is given in the right panel of figure 4.10. Before the track selection criteria are applied, the distribution between $N_{\mathrm{TPC}}^{\mathrm{cls}} = 50$ and $N_{\mathrm{TPC}}^{\mathrm{cls}} = 130$ is almost flat. After the application of the track selection criteria the distribution rises towards a value of $N_{\mathrm{TPC}}^{\mathrm{cls}} \approx 140$. Thus, the other criteria select preferably tracks with a higher amount of $N_{\mathrm{TPC}}^{\mathrm{cls}}$, what corresponds to tracks of a high reconstruction quality. In the Monte Carlo simulation, electrons from $J/\psi \rightarrow e^+e^-$ decays tend to be reconstructed with high values of $N_{\mathrm{TPC}}^{\mathrm{cls}} \geq 140$. This observation supports a minimum requirement of $N_{\mathrm{TPC}}^{\mathrm{cls}}$ for the track reconstruction.

Trajectory and space point agreement: After the reconstruction of a particle's trajectory its deviation (χ^2) from the space points assigned to the particle is measured and normalized to the number of clusters of the track:

$$\frac{\chi^2}{N_{\mathrm{cls}}} = \frac{1}{N_{\mathrm{cls}}} \sum_{i=0}^{n_{\mathrm{cls}}} \frac{y_{i,cls} - y_{i,trjy}}{\sigma_{i,y}^2} \frac{z_{i,cls} - z_{i,trjy}}{\sigma_{i,z}^2}. \tag{4.27}$$

For the **ITS** the normalized deviation has to be within

$$0 \leq \frac{\chi^2_{\mathrm{ITS}}}{N_{\mathrm{ITS}}^{\mathrm{cls}}} \leq 5. \tag{4.28}$$

For the **TPC** it is required to be within

$$0 \leq \frac{\chi^2_{\mathrm{TPC}}}{N_{\mathrm{TPC}}^{\mathrm{cls}}} \leq 2.75. \tag{4.29}$$

As reference, the number of degrees of freedom (n_{dof}) for the measurement with the TPC is $n_{\mathrm{dof}} = 2 \cdot N_{\mathrm{cls}} - 5$. The reduction of n_{dof} by five results from the five

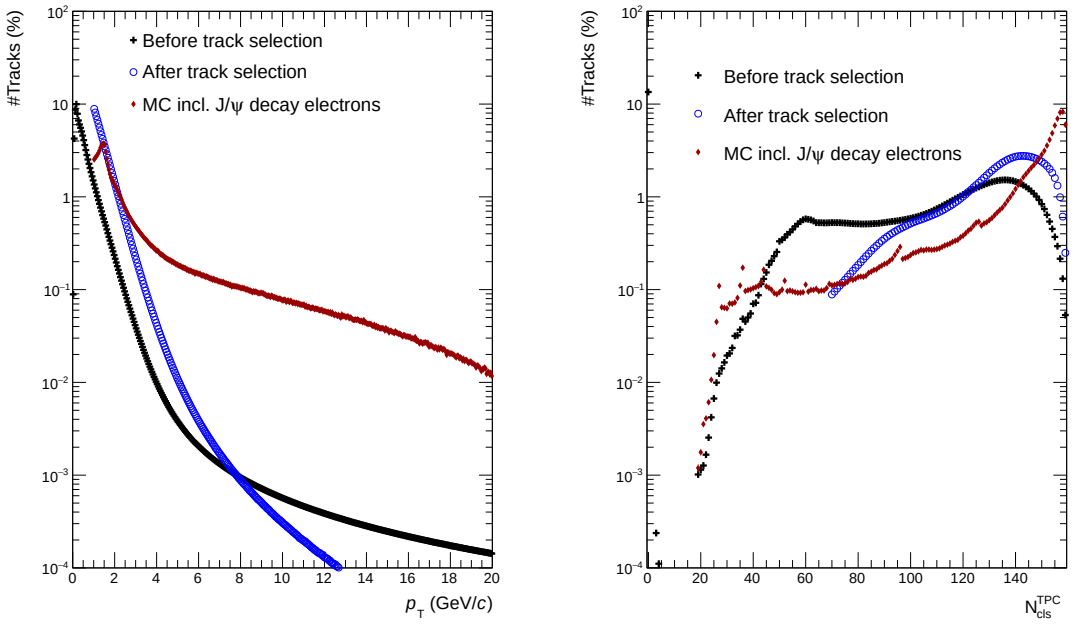

Figure 4.10: Left panel: Track-p_T distribution of the data track sample before (black crosses) and after (blue circles) the track selection and of electrons from $J/\psi \to e^+e^-$ decays in Monte Carlo simulations (red diamonds). Right panel: Distribution of N_{TPC}^{cls} measured before and after the track selection in experimental data and measured for electrons from $J/\psi \to e^+e^-$ decays in Monte Carlo simulations(red diamonds).

parameters used by fit in the Kalman filter (see 3.2.1). Thus, the selection criterion in the TPC corresponds to $\frac{\chi^2}{N_{dof}} \lesssim 1.5$. The left panel of figure 4.11 illustrates the behavior of the track sample as function $\frac{\chi^2_{ITS}}{N^{cls}_{ITS}}$ and $\frac{\chi^2_{TPC}}{N^{cls}_{TPC}}$. The track selection shifts the most probable values of the distributions of $\frac{\chi^2_{ITS}}{N^{cls}_{ITS}}$ (black crosses) and $\frac{\chi^2_{TPC}}{N^{cls}_{TPC}}$ (green stars) towards lower values (blue open circles and full circles). Hence, preferably tracks with a better agreement between the reconstructed trajectory and the assigned space points, compared to the most probable values before the track selection, are selected. The clear majority of electrons from $J/\psi \to e^+e^-$ decays in Monte Carlo simulations are reconstructed with values for $\frac{\chi^2_{ITS}}{N^{cls}_{ITS}}$ (pink open diamonds) and $\frac{\chi^2_{TPC}}{N^{cls}_{TPC}}$ (red full diamonds) within the applied selection criteria. Their distributions show a steeper falling slope towards larger values, than the track sample before the application of the track selection.

Number of shared clusters in the ITS: Due to the small opening angle of dielectron pairs from photon conversions, they have a significantly higher probability to share a cluster in the ITS in comparison to dielectron pairs from $J/\psi \to e^+e^-$ decays. Thus, rejecting tracks that have a high ratio of shared clusters over their total amount of clusters in the ITS reduces the contamination of the electron candidate sample with electrons from photon conversions. In the presented analyses, only tracks with

$$\frac{N^{\text{Shar. cls}}_{ITS}}{N^{cls}_{ITS}} < 0.4 \tag{4.30}$$

are accepted. The simulated number of shared clusters for electrons from $J/\psi \to e^+e^-$ decays clearly supports this criterion. The distribution is shown in the right panel of figure 4.11 (red diamonds). More than 90% of the electrons are reconstructed without any shared clusters. In data already below the threshold of $\frac{N_{\mathrm{ITS}}^{\mathrm{Shar.\ cls}}}{N_{\mathrm{ITS}}^{\mathrm{cls}}} < 0.4$ an increase of the steepness of the distribution is observed, when comparing the distributions before (black crosses) and after (blue circles) the application of the track selection. This change is a result of the required hit in one of the SPD layers (see eq. 4.31).

Kink rejection: Track candidates are rejected, if a "kink" in their trajectory through the detector is observed. Such kinks point to an interaction, e.g. a weak decay, of the electron candidate preventing a correct reconstruction of the original J/ψ-decay kinematics.

First hit in the SPD: Electrons from photon conversions ($\gamma + A \to e^+e^- + A$) are a potential background source. An efficient way to reject electrons from conversions is the requirement of at least one track-correlated hit in any of the three SPD layers:

$$N_{\mathrm{SPD}}^{\mathrm{Hit}} \geq 1 \tag{4.31}$$

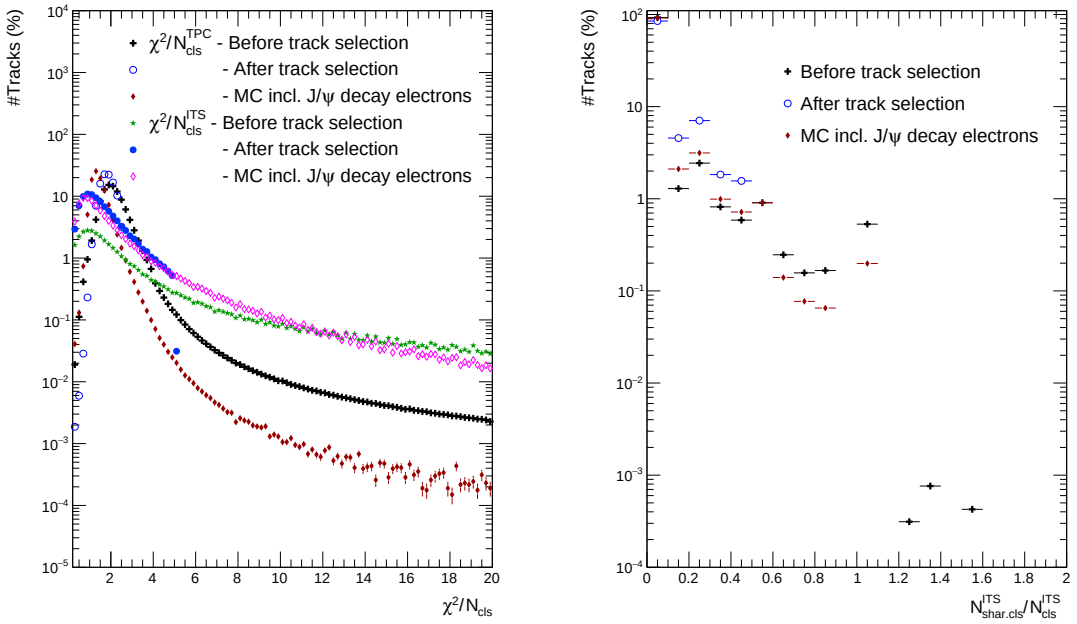

Figure 4.11: Distribution of χ^2 normalized to the number of measured track clusters in the given detector (left panel) and of the fraction of $N_{\mathrm{ITS}}^{\mathrm{Shar.\ cls}}$ over $N_{\mathrm{ITS}}^{\mathrm{cls}}$ (right panel) measured in experimental data before (black crosses) and after (blue circles) the track selection and measured for electrons from $J/\psi \to e^+e^-$ decays in Monte Carlo simulations(red diamonds).

Track impact parameter: Since a J/ψ has a very short lifetime, selecting only those tracks originating from small distances around the event vertex for further

analyses, reduces the background contamination of the track sample. The distance between the event vertex and track origin is called distance of closest approach (dca). Tracks originating from outside of:

$$-1.0 \text{ cm} \leq dca_{\text{xy}} \leq 1.0 \text{ cm}, \tag{4.32}$$

or

$$-3.0 \text{ cm} \leq dca_{\text{z}} \leq 3.0 \text{ cm} \tag{4.33}$$

are rejected. In figure 4.12 the dca distributions in the x-y plane (left panel) and the z-axis (right panel) are depicted. Both panels show that the track sample before the application of the track selection (black crosses) has the widest distribution. The distributions for electrons from $\text{J}/\psi \to e^+e^-$ decays (red diamonds), estimated with Monte Carlo simulations, are significantly peaked within ± 0.2 cm (dca_{xy}) and ± 2 cm (dca_{z}). This indicates that most electrons from $\text{J}/\psi \to e^+e^-$ decays fulfill the applied selection criteria for dca_{xy} and dca_{z} and vise versa rejected tracks mainly originate from other sources. Between the distributions before (black crosses) and after (blue circles) the track selection a steeper decrease towards the borders of the selection criteria is observed after the track selection was applied. Thus, the majority of tracks selected by the other selection criteria also fulfills the track impact parameter criteria.

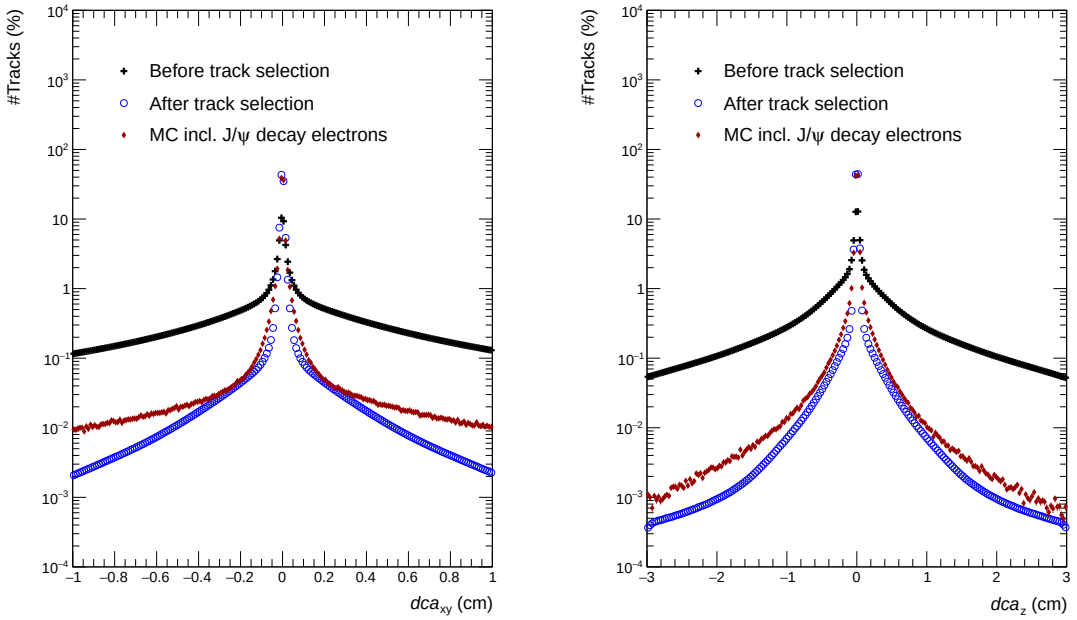

Figure 4.12: Track dca distribution in the x-y plane (left panel) and the z-axis (right panel) measured in experimental data before (black crosses) and after (blue circles) the track selection and measured for electrons from $\text{J}/\psi \to e^+e^-$ decays in Monte Carlo simulations(red diamonds).

ITS and TPC refit: The reconstruction of a particle's trajectory through the mid-rapidity detectors of ALICE is based on a Kalman filter algorithm [65]. The so-called "refit" flag for a given tracking detector is set, if the final inward fit of the Kalman filter algorithm inside the detector was successful.

After the application of all track selection criteria, about 4% of the initial track sample remains. Further track selection criteria, applied in those cases where PID informations from the TRD are used, are discussed in the chapter 6.

4.6 Particle identification

4.6.1 TPC

The goal of the particle identification in this analysis is the selection of electrons and positrons out of the remaining track sample after the track selection.

Based on the parametrized specific energy loss ($n\sigma^{\mathrm{TPC}}_{\mathrm{Particle}}$) of electrons, pions and protons in the TPC (see equation 3.4), a selection of electrons and positrons, as well as a rejection of protons and pions, is applied:

$$-2.5 \leq n\sigma^{\mathrm{TPC}}_{\mathrm{e}} \leq 3, \tag{4.34}$$

$$n\sigma^{\mathrm{TPC}}_{\mathrm{p}} \geq 3.5, \tag{4.35}$$

$$n\sigma^{\mathrm{TPC}}_{\pi} \geq 3.5. \tag{4.36}$$

At first order, the estimation of the expected $\mathrm{d}E/\mathrm{d}x$ is based on a parametrization of the Bethe-Bloch equation (see equation 3.3 and figure 3.6). However, to achieve the needed precision for a successful PID, an additional calibration of the parametrization for each individual data taking period is required. After a first global calibration, a second so-called "post-calibration" is applied. This calibration step accounts more specifically than the global calibration for the characteristics of the selected track sample used in the analysis. The post-calibration uses information gathered from the analysis of topological selected electrons. In this case, so-called "V0 electrons" from gamma conversions are selected, mainly utilizing the fact that they appear "off vertex" and have vanishing invariant mass. The mean of the measured parametrized specific energy loss for electrons ($n\sigma^{\mathrm{TPC}}_{\mathrm{e}^{\pm}}$) distributions corresponds to the deviation between the measured $\mathrm{d}E/\mathrm{d}x$ and the expected value from the parametrization of the Bethe-Bloch function (see equations 3.3, 3.4). Thus, correctly calibrated, the mean of the $n\sigma^{\mathrm{TPC}}_{\mathrm{e}^{\pm}}$ distributions should be at zero for all centrality intervals. Since $n\sigma^{\mathrm{TPC}}_{\mathrm{e}^{\pm}}$ is normalized to the resolution of the $\mathrm{d}E/\mathrm{d}x$ measurement a width of one is targeted for the acnSigmaTPCele distributions. Demonstrated in figure 4.13 is the deviation of the mean (left panel) of the $n\sigma^{\mathrm{TPC}}_{\mathrm{e}^{\pm}}$ distribution from zero and of the width (right panel) from unity for V0 electrons as function of the collision centrality before the post-calibration is applied. The two different markers indicate two separately reconstructed sub-periods of the LHC15o data sample. The evolution of the mean as function of the centrality corresponds to a decrease of the average $\mathrm{d}E/\mathrm{d}x$ per track in more central collisions, due to a higher track density in the TPC. Due to the smaller signals that are measured in more central collisions, the influence of fluctuations on the measurement rises. Thus, the width of the $n\sigma^{\mathrm{TPC}}_{\mathrm{e}^{\pm}}$ distributions increases. Post-calibration maps, correcting the values of the expected $\mathrm{d}E/\mathrm{d}x$ for their deviations, are produced containing corrections as function of η and centrality. A more detailed discussion and the applied calibration maps can be found in [98].

The influence of the selection criteria listed in the equations 4.34, 4.35 and 4.36 is visualized in figure 4.14. From left to right, the electron selection, and proton and pion rejection criteria are applied. The proton rejection is visible below ~ 1.5 GeV/c particle momentum, where the expected proton $\mathrm{d}E/\mathrm{d}x$ as function of momentum

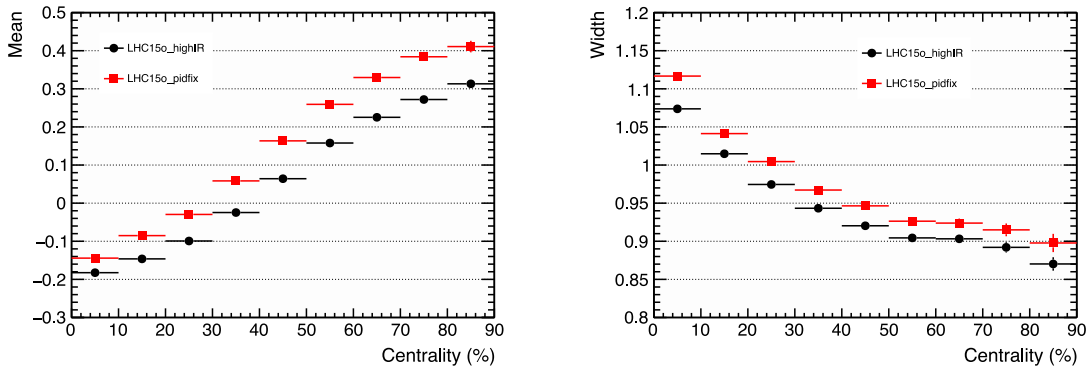

Figure 4.13: Mean (left panel) and width (right panel) of the parametrized specific energy loss for electrons ($n\sigma_{\mathrm{e}^{\pm}}^{\mathrm{TPC}}$), measured with a selected V0-electron sample, as function of the collision centrality. The different markers correspond to two different sub periods of the LHC15o data sample. [98]

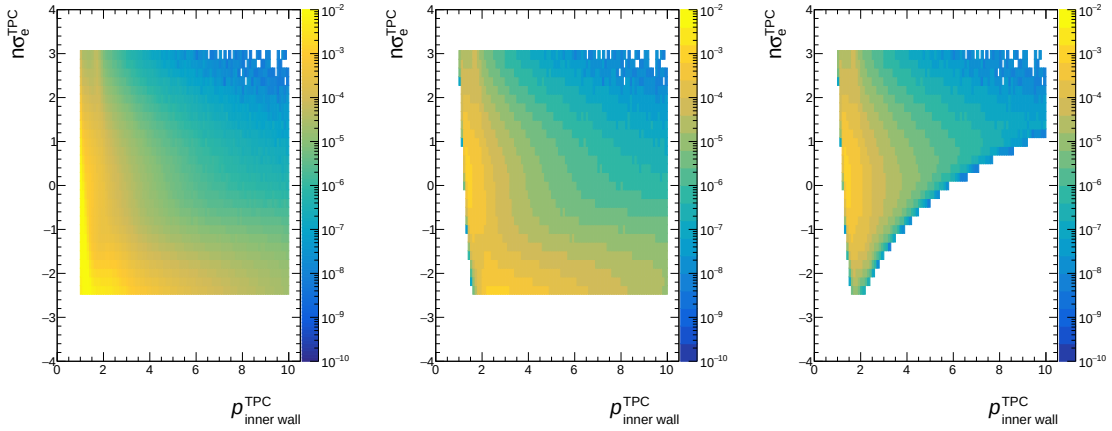

Figure 4.14: Distribution of the parametrized specific energy loss for electrons ($n\sigma_{\mathrm{e}^{\pm}}^{\mathrm{TPC}}$) as function of their momentum measured at the entry of point into the TPC for the track sample after track selection. From left to right, the electron selection (eq. 4.34), and proton (eq. 4.35) and pion (eq. 4.36) rejection criteria are added to the track selection.

crosses the electron $\mathrm{d}E/\mathrm{d}x$. With increasing momentum, the separation capability between electrons and pions of the TPC is reduced, since the pions also approach the relativistic rise of the Bethe-Bloch equation. Thus, the pion rejection interferes with electron selection and particles inside the $-2.5 \leq n\sigma_{\mathrm{e}}^{\mathrm{TPC}} \leq 3$ electron selection are rejected.

4.6.2 TOF

In the same manner as for the $\mathrm{d}E/\mathrm{d}x$ measurement of the TPC, a deviation from the expected time of flight for a given particle is calculated and normalized to the resolution. Accordingly, an electron selection based on

$$|n\sigma_{e}^{\mathrm{TOF}}| \leq 3 \tag{4.37}$$

is applied. This allows to rejects hadrons, mainly entering the track sample in the crossing regions of the electrons and the hadron bands in the TPC. However, the TOF delivers an efficient separation of electrons and hadrons only up to $p_{\mathrm{T}} \approx 4$ GeV/c. Thus, the selection described in equation 4.37 is only applied for tracks with $p_{\mathrm{T}} < 4$ GeV/c. Another difficulty that appears using the information from the TOF is the relatively small track-matching efficiency to the TOF. To ensure that only tracks identified as hadrons by the TOF measurement are rejected, and not additionally those where simply no TOF information is available, the TOF selection criteria has only to be fulfilled by tracks that actually have been measured by the TOF. This approach is also called an "if available" selection criteria. Already the TOF itself, but especially in the "if available" mode of the selection criteria, is difficult to calibrate correctly for reconstruction efficiencies based on Monte Carlo simulations. Hence, the above discussed criteria are only applied in the $v_2^{\mathrm{J}/\psi}$ analysis, which is not corrected for reconstruction efficiencies.

4.7 J/ψ reconstruction

After the preparation of an electron/positron candidate sample by the track selection and particle identification, a pair reconstruction algorithm combines electron and positron candidates and calculates the pairs properties. The energy-momentum four-vectors of the electron and positron candidate are added, to reconstruct the kinematic properties of the J/ψ candidate:

$$\mathbf{P}_4^{\mathrm{Cand.}} = \mathbf{P}_4^{e^+} + \mathbf{P}_4^{e^-}.$$

With $\mathbf{P}_4^{\mathrm{Cand.}}$ one can calculate the invariant mass of the J/ψ candidate:

$$m_{\mathrm{inv.}} = \sqrt{(E_{e^-} + E_{e^+})^2 - (\mathbf{p}_{e^-} + \mathbf{p}_{e^+})^2} = 2m_e^2 + 2(E_{e^-}E_{e^+} - \mathbf{p}_{e^-}\mathbf{p}_{e^+}). \quad (4.38)$$

The so-called ***opposite sign (OS) spectrum*** is derived from all possible pair combinations of the electron and positron sample. A recursive rejection of electron and positron candidates from conversions is applied within the first iteration of the pairing algorithm. Tracks forming any pair with:

$$m_{\mathrm{inv.}} \leq 0.05 \text{ GeV}/c \quad (4.39)$$

and thus showing a high probability to originate from a photon conversion instead of a J/ψ, are excluded from the track sample to reduce the background.

The random combination of all electron and positron candidates into a dielectron pair in a given event introduces a combinatorial background to the pair sample. To retrieve the number of reconstructed J/ψ from the OS spectrum, the background has to be subtracted from the OS spectrum.

4.7.1 Background estimation

The OS spectrum contains two different sources of background: an uncorrelated part due to the pairing of random electron-positron combinations, and a correlated part, for example from open-charm decays. For the given data sample and detector configuration, the most prominent background source is the combinatorial background. The shape of the combinatorial background is dominated by the single electron and positron phase-space distributions. However, the global properties of a given event

and their influence on the track reconstruction, e.g. elliptic flow and track multiplicity, lead to a small but not vanishing correlation between decay-wise uncorrelated tracks of the same event. Several approaches are possible to estimate the shape and size of the combinatorial background with varying advantages and disadvantages [99]. In the analyses presented in this thesis, the benchmark method for the background estimation is the ***event-mixing (ME)*** technique. To investigate a potential systematic influence of the ME technique on the results, a comparison to the ***like-sign (LS)*** technique is utilized.

Event mixing: The event-mixing technique pairs electrons and positrons from different events in order to estimate the combinatorial background. This approach has two major advantages:

- it allows to reduce the statistical error of the background estimation to a minimum;
- it ensures that there are no correlations between the paired tracks.

To include the above mentioned influence of the global event properties on the same-event OS background spectrum, event categories are defined in which the tracks are mixed. Depending on the analyzed event centralities (0%-90% $R_{\mathrm{AA}}^{\mathrm{J}/\psi}$; 20%-40% $v_2^{\mathrm{J}/\psi}$) different categories are needed to reproduce the background correctly. For both analyses the events are categorized in eight $\Psi_{\mathrm{ep.}}$ intervals, to account for angular correlations, introduced into the same-event background by the global elliptic flow. In the elliptic flow analysis presented in chapter 5, the azimuthal event-plane angle estimated by the V0C is used for the categorization to minimize non-flow effects. However, since $\Psi_{\mathrm{ep.}}^{\mathrm{TPC}}$ should describe the event properties that induce correlations in the background more precisely, it is used for the $R_{\mathrm{AA}}^{\mathrm{J}/\psi}$ measurement presented in chapter 6. Correlated variations of the track behavior induced by the track density of the event are taken care of by sorting the events into collision-centrality categories. For the $v_2^{\mathrm{J}/\psi}$ measurement 10% wide intervals are utilized and 5% wide intervals for the $R_{\mathrm{AA}}^{\mathrm{J}/\psi}$ measurement, respectively. For the $R_{\mathrm{AA}}^{\mathrm{J}/\psi}$ measurement presented in chapter 6, the events are additionally subdivided into groups of z_{vtx} positions. A summary of the used mixing categories is given in table 4.1.

Category	n intervals	range
$\Psi_{\mathrm{ep.}}$	8	$-1/2\pi \ldots 1/2\pi$
$\mathcal{C}$	9 (18-$R_{\mathrm{AA}}^{\mathrm{J}/\psi}$)	$0\% \ldots 90\%$
z_{vtx} [cm] ($R_{\mathrm{AA}}^{\mathrm{J}/\psi}$ only)	14	$[-10,\ -7,\ -5,\ -4, \ldots,\ 4,\ 5,\ 7,\ 10]$

Table 4.1: Summary of event-mixing categories.

A peculiarity of the Pb−Pb data measured at high interaction rates in 2015 is the out-of-bunch pileup discussed in section 4.2. It also influences the background estimation with the event-mixing technique. Without the rejection of the events containing out-of-bunch pileup, the shape of the estimated background does not match the shape of the background in the measured OS spectrum. Most probably this occurs due to the varying track reconstruction between the events with and without out-of-bunch pileup. For example, an increased pion contamination in out-of-bunch pileup events can lead to additional correlations in the OS spectrum, which can not be reproduced by the event-mixing background estimation. As mentioned

previously, a detailed investigation of the out-of-bunch pileup events is still ongoing and for the presented analyses they are excluded from the event sample.

The statistical precision of the background estimation with the event-mixing technique depends on the amount of mixed events per category. Limited by the amount of random access memory (ram) per analysis node, up to 150 events per category are mixed per bin, in the case that nanoAODs are used. Since more tracks are combined for the background estimation than in the creation of the OS spectrum, it has to be scaled to match the height of the OS spectrum. Therefore, the ratio between the OS spectrum and the ME spectrum in regions without a dielectron-resonance signal, e.g. 2.5 GeV/$c \leq m_{\text{inv.}} \leq$ 2.8 GeV/c & 3.5 GeV/$c \leq m_{\text{inv.}} \leq$ 3.8 GeV/c, is utilized as scaling factor.

Like sign: The LS method estimates the background contribution to the OS spectrum based on the combination of tracks with identical electric charge. Electron-electron and positron-positron pairs do not contain correlations. Hence, the LS spectrum depicts the combinatorial part of the OS background spectrum. It has the advantage that it naturally contains the correlations introduced to the track sample by the global event properties. Thus, it reproduces the shape of the OS background spectrum without additional corrections, like event-mixing categories. However, it is limited in its statistical precision by the amount of electron-positron pairs per event:

$$B = N_+ \cdot N_- - \sqrt{N_+ N_-}. \tag{4.40}$$

In this equation B denotes the number of background pairs and $N_\pm$ the corresponding number of electrons or positrons. It is only valid in the case of solely combinatorial background and the successful reconstruction of every signal pair. To estimate the number of signal pairs (S) under realistic conditions, the following equations can be used:

$$S = N_\pm - R \cdot 2\sqrt{N_{++} N_{--}} \qquad \text{(geometric mean)}, \tag{4.41}$$

$$S = N_\pm - R \cdot (N_{++} + N_{--}) \qquad \text{(arithmetic mean)}. \tag{4.42}$$

While the geometric mean is the preferable method for the estimation of the background, in a situation of vanishing same-sign pairs and simultaneously occurring charge asymmetries the utilization of the arithmetic mean becomes necessary. A mass-dependent correction for charge asymmetries is introduced as R factor. It can for example be estimated from the comparison of the LS spectrum to the ME spectrum:

$$R(m_{\text{inv.}}) = \frac{N^{\text{ME}}_{+-}(m_{\text{inv.}})}{2\sqrt{N_{++}(m_{\text{inv.}}) N_{--}(m_{\text{inv.}})}}. \tag{4.43}$$

Nevertheless, significant deviations from unity appear mainly in the low-mass regions, while in the mass region of the J/ψ, for the given data sample, the R-factor can be assumed to be close to unity [100]. Presented in figure 4.15 are the background spectra from the ME (black crosses) and LS (blue circles) technique, corresponding to an inclusive J/ψ spectrum for the 90% most central events. In the bottom panel, the ratio of both spectra is given. As discussed before, significant deviations from unity are only observed in the mass region below 1 GeV/c^2.

4.7.2 Signal extraction

Based on the background subtracted OS spectrum, the signal yield, i.e. the amount of measured J/ψ, can be extracted. To retrieve the J/ψ yield, two different methods

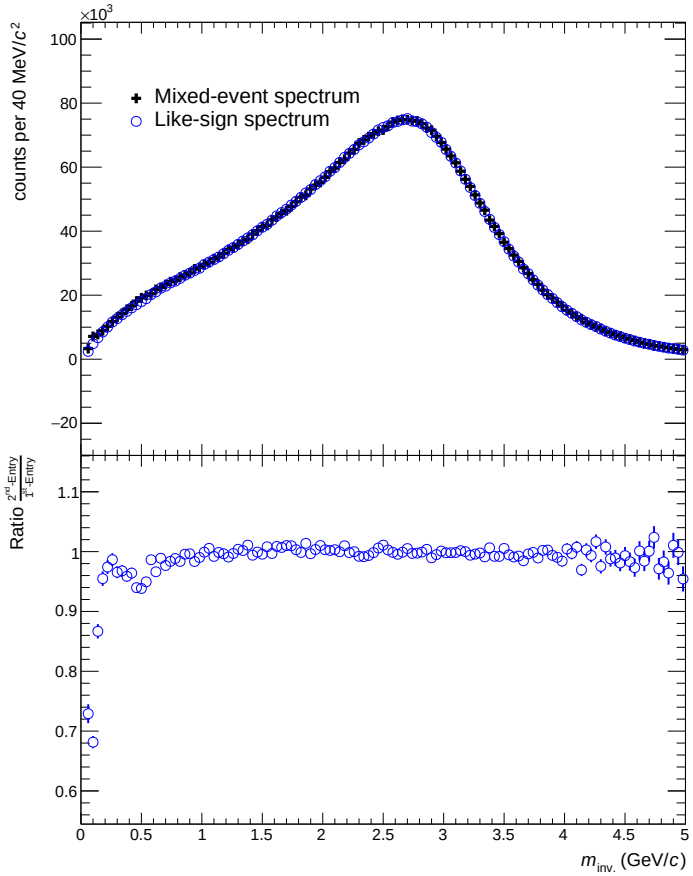

Figure 4.15: Background estimations for the inclusive J/ψ dielectron spectrum from the event-mixing (ME) (black crosses) and the like-sign (LS) technique (blue circles), measured in the 90% most central events. Both estimations are scaled with a constant, estimated outside the J/ψ signal region, to the opposite sign (OS) spectrum individually. The bottom part shows the ratio of the LS over the ME estimation.

are employed. The ***"bin counting"*** method is a quite intuitive and simple approach to extract the signal yield:

$$S = \sum_{m_{\mathrm{inv.}}\ \mathrm{range}} w_i. \tag{4.44}$$

It sums up the bin content (w_i) of all bins in a given mass window. As shown in table 2.1, the decay width of the J/ψ (< 0.1 MeV/c^2) is far below the measured resolution of the invariant mass OS spectrum (40 MeV/c^2). Thus, one could expect the resonance peak in only one single mass bin. However, due to the resolution of the measurement and also energy losses of the electrons due to "Bremsstrahlung", of which the recovery is difficult, the width of the measured resonance is wider. Hence, the mass window used for the bin counting method is 2.92-3.16 GeV/c^2, and as a systematical variation, a width of 2.85-3.20 GeV/c^2 is used.

A different approach to extract the J/ψ signal yield is the integration of a fitted J/ψ signal shape, estimated beforehand with Monte Carlo simulations. The Monte Carlo simulated shape contains the low-mass tail due to Bremsstrahlung of electrons. This fixed shape is then scaled to the background subtracted OS spectrum and integrated over the same mass windows as used in the bin counting method.

Depicted in figure 4.16 is the OS spectrum for the 90% most central events together with the corresponding background estimation from the ME (left) and the LS (right) technique. In the bottom panes of both panels, the corresponding background subtracted OS spectrum is given. Extracted with the bin counting method, yields of $S = 12553 \pm 802.5$ (ME background) and $S = 12020 \pm 944.4$ (LS background) J/ψ are observed. Based on a signal-over-background of $S/B = 0.0284 \pm 0.00181$ (ME) and $S/B = 0.0271 \pm 0.00213$ (LS), respectively, a significance of

$$\frac{S}{\sqrt{S+B}} = 18.6 \pm 1.17 \text{ (ME) } (17.8 \pm 1.38 \text{ (LS)}) \tag{4.45}$$

is observed. A discussion on the calculation of the statistical uncertainties and the definition of the significance can be found in the appendix A.

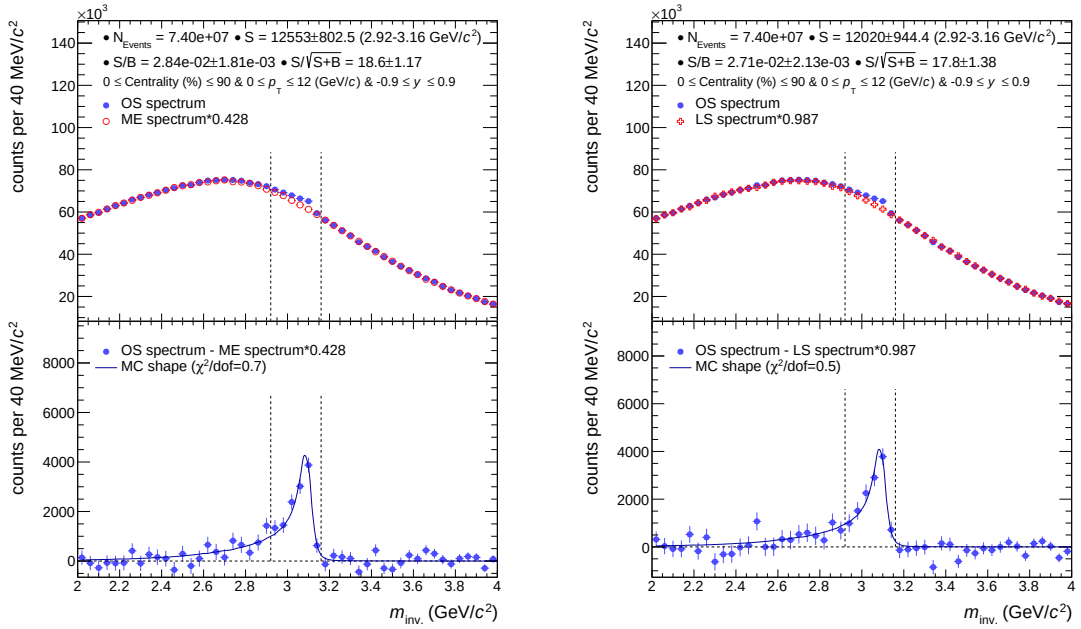

Figure 4.16: Demonstration of a J/ψ-signal extraction. The top panes of both panels show the opposite sign (OS) spectrum together with the event-mixing (ME) (left panel), like-sign (LS) (right panel) background estimation. The bottom parts show the corresponding background-subtracted signal spectrum.

In similar manner, the signal and background yield and the significance have been extracted for subsamples of the data set for further analyses. The signal extraction as function of the azimuthal orientation with respect to $\Psi_{\text{ep.}}$ will be discussed in chapter 5. To measure $\sigma^{\text{J}/\psi}$ and $R_{\text{AA}}^{\text{J}/\psi}$ respectively, the signal extraction has to be corrected for its efficiencies. The applied efficiency correction to measure $R_{\text{AA}}^{\text{J}/\psi}$ with the TRD as additional PID detector will be discussed in the chapter 6.

5 Elliptic flow of J/ψ

In this chapter the phenomenological concept, why J/ψ originating from a QGP could inherit a non-zero elliptic flow, will be shortly introduced, followed by the presentation of the measurement itself and a comparison of latest model calculations with the results of the measurement.

5.1 Phenomenology

If thermalization of heavy-quarks, i.e. c or $\bar{\text{c}}$ quarks, takes place in the QGP, they should be subject to collective effects like elliptic flow. In the case of the J/ψ, this leads to significant differences of the kinematic properties of direct J/ψ and those originating from a (re)combination of quasi-free c$\bar{\text{c}}$ quark pairs out of the collective medium. The v_2 of inclusive charged particles as function of p_{T}, measured in the

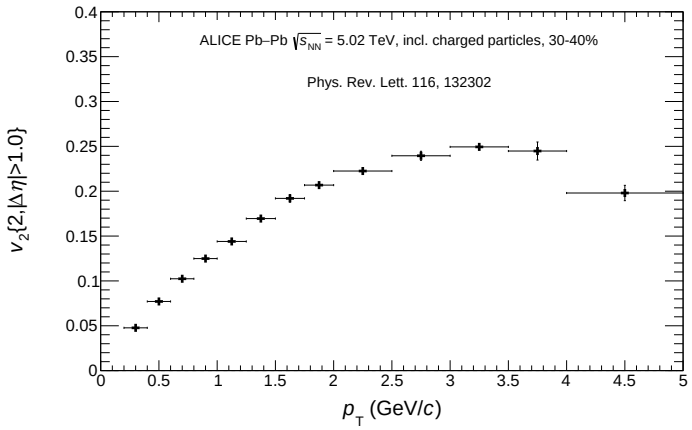

Figure 5.1: Ellitpic flow (v_2) of inclusive charged particles as function of the transverse momentum (p_{T}), measured in $\sqrt{s_{\text{NN}}} = 5.02$ TeV Pb−Pb collisions with ALICE [101].

centrality range 30% to 40% in Pb−Pb collisions at $\sqrt{s_{\text{NN}}} = 5.02$ TeV, is given in figure 5.1. A significant v_2 is observed especially for transverse momenta above 2 GeV/c. The pressure gradient, responsible for the development of the observed v_2, should influence quasi-free c or $\bar{\text{c}}$ quarks in a similar manner and result in a non-zero $v_2^{\text{J}/\psi}$ for J/ψ from regeneration processes. Hence, the measurement of $v_2^{\text{J}/\psi}$ is capable to put further constraints on the models that contain a description of the J/ψ production. Especially a comparison to transport models, like those introduced in section 2.4.3b, is of interest. Those models contain a full kinematic evolution of the fireball and are able to separate the kinematics of primordial and regenerated J/ψ. Thus, comparisons between measured data and theoretical predictions should be able to shed further light on the details of the J/ψ production.

5.2 Measurement

The elliptic-flow measurement of J/ψ is based on the measurement of the difference between $\Psi_{\text{ep.}}$ (see section 4.4) and the azimuthal orientation of the J/ψ ($\varphi_{J/\psi}$):

$$\Delta\phi = \varphi_{J/\psi} - \Psi_{\text{ep}}. \tag{5.1}$$

As already shortly introduced in section 4.4, azimuthal correlations in heavy-ion collisions can be expressed in form of a Fourier expansion [96, 102, 103]:

$$E\frac{\mathrm{d}^3N}{\mathrm{d}^3p} = \frac{1}{2\pi}\frac{\mathrm{d}^2N}{p_{\mathrm{T}}\mathrm{d}p_{\mathrm{T}}\mathrm{d}y}\left(1 + \sum_{n=1}^{\infty} 2v_n\cos(n(\varphi - \Psi))\right). \tag{5.2}$$

Starting from the equation above, two different approaches give access to $v_2^{\mathrm{J}/\psi}$, both are based on the measurement of $\Delta\phi$.

In- and out-of-plane: This approach is based on a J/ψ-yield measurement in dependence of $\Delta\phi$. The integration of equation 5.2 leads to the following expression for $v_2^{\mathrm{J}/\psi}$:

$$v_2^{\mathrm{J}/\psi} = \frac{\pi}{4 \cdot R_2}\frac{S_{\text{in}} - S_{\text{out}}}{S_{\text{in}} + S_{\text{out}}}. \tag{5.3}$$

Here R_2 denotes the resolution of the azimuthal event-plane angle measurement (introduced in section 4.4.3) as correction factor and $S_{\text{in/out}}$ represents the signal yield measured in two $\Delta\phi$ ranges:

$$S_{\text{in}} \longleftrightarrow \begin{cases} |\Delta\phi| < \frac{\pi}{4} \text{ and} \\ \frac{3\pi}{4} < |\Delta\phi| < \pi \end{cases}, \tag{5.4}$$

$$S_{\text{out}} \longleftrightarrow \frac{\pi}{4} < |\Delta\phi| < \frac{3\pi}{4}. \tag{5.5}$$

While the range defined in equation 5.4 corresponds to the range of azimuthal angles with $\Psi_{\text{ep.}}$ in the center and thus, S_{in} denotes the yield measured "in-plane", S_{out} represents the yield measured "out-of-plane".

Fit method: For the $v_2^{\mathrm{J}/\psi}$ measurement with the "fit method", the dielectron-pair v_2 is measured as function of $m_{\text{inv.}}$:

$$v_2^{ee}(m_{\text{inv.}}) = \langle\cos(2(\varphi^{ee}(m_{\text{inv.}}) - \Psi_{\text{ep.}}))\rangle. \tag{5.6}$$

This dielectron-pair v_2 is composed out of $v_2^{\mathrm{J}/\psi}$ and the artificial flow of the combinatorial background v_2^B, weighted with the number of signal (background) dielectron pairs [104]:

$$v_2^{ee}(m_{\text{inv.}}) = \frac{S(m_{\text{inv.}}) \cdot v_2^{J/\psi}(m_{\text{inv.}}) + B(m_{\text{inv.}}) \cdot v_2^B(m_{\text{inv.}})}{S(m_{\text{inv.}}) + B(m_{\text{inv.}})}. \tag{5.7}$$

The signal and background spectra as function of $m_{\text{inv.}}$ are measured with the standard signal-extraction procedure, as introduced in section 4.7.2. From these spectra then the values for S and B as function of ($m_{\text{inv.}}$) are extracted. Thus, only $v_2^{\mathrm{J}/\psi}$ and v_2^B are left as unknown components. To estimate v_2^B, selected parts of the v_2^{ee}

distribution as function of $m_{\text{inv.}}$ are fitted with a polynomial function. For the selection of the fitted parts, the v_2^{ee} data points in the J/ψ mass range, as used for the signal extraction, are excluded. The shape of the combinatorial background of the v_2 measurement depends on the kinematic composition of the dielectron pairs. Thus, at different p_{T} bins polynomial-functions of different orders (2nd, 3rd and 5th) have to be used to estimate the v_2^B distribution. In the last step, the function representing the full v_2^{ee} composition, given in equation 5.7, is fitted to the data points, with $v_2^{\text{J}/\psi}$ as free parameter. A demonstration of the $v_2^{\text{J}/\psi}$ measurement

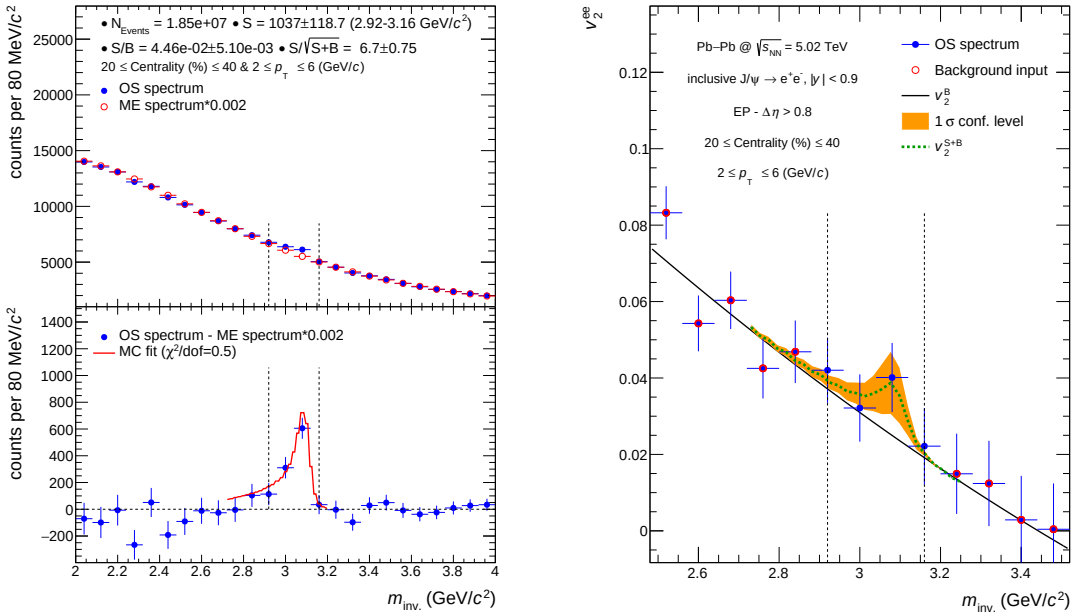

Figure 5.2: Right panel: Dielectron pair invariant mass spectrum, used as input for the elliptic flow of J/ψ ($v_2^{\text{J}/\psi}$) extraction. Left panel: Elliptic flow of dielectron pairs (v_2^{ee}) with $2 \leq p_{\text{T}} \leq 6$ GeV/c as function of their invariant mass ($m_{\text{inv.}}$). Measured in semi-central events (20-40%), with the V0C detector as event-plane estimator.

based on the fit method is given in figure 5.2. In the left panel the J/ψ-yield extraction is shown, it provides the signal and background yield as input for the $v_2^{\text{J}/\psi}$ extraction via the fit method, which is depicted in the right panel of the figure. The measured v_2^{ee} is represented by the blue, full circles, the red, open circles indicate those data points, used to constrain the second order polynomial function, utilized to estimate v_2^B. The resulting function for v_2^{ee} (v_2^B) after the respective fit is drawn as green, dashed (black, solid) line. In addition a 1σ confidence level around the fit is shown in orange, to visualize significance of the difference between v_2^B and v_2^{ee}, which corresponds to $v_2^{\text{J}/\psi}$.

5.3 Dependence on $\Delta\phi$ of the J/ψ reconstruction efficiency

Both introduced methods to measure $v_2^{\text{J}/\psi}$ rely on the assumption that the J/ψ reconstruction efficiency does not depend on the relative azimuthal orientation of the

J/ψ with respect to $\Psi_{\mathrm{ep.}}$ ($\Delta\phi$). Potential inhomogeneities of the detector acceptance along azimuth are accounted for by the calibration procedures ensuring a flat $\Psi_{\mathrm{ep.}}$ distribution. However, a correlation of the reconstruction efficiency to $\Delta\phi$ would artificially in- or decrease $v_2^{\mathrm{J}/\psi}$. The only variation as function of $\Delta\phi$ that could influence the J/ψ reconstruction significantly is the particle density. As a direct result of the existence of elliptic flow of charged particles in heavy-ion collisions, the track density along $\Delta\phi$ shows large variations. These variations are clearly

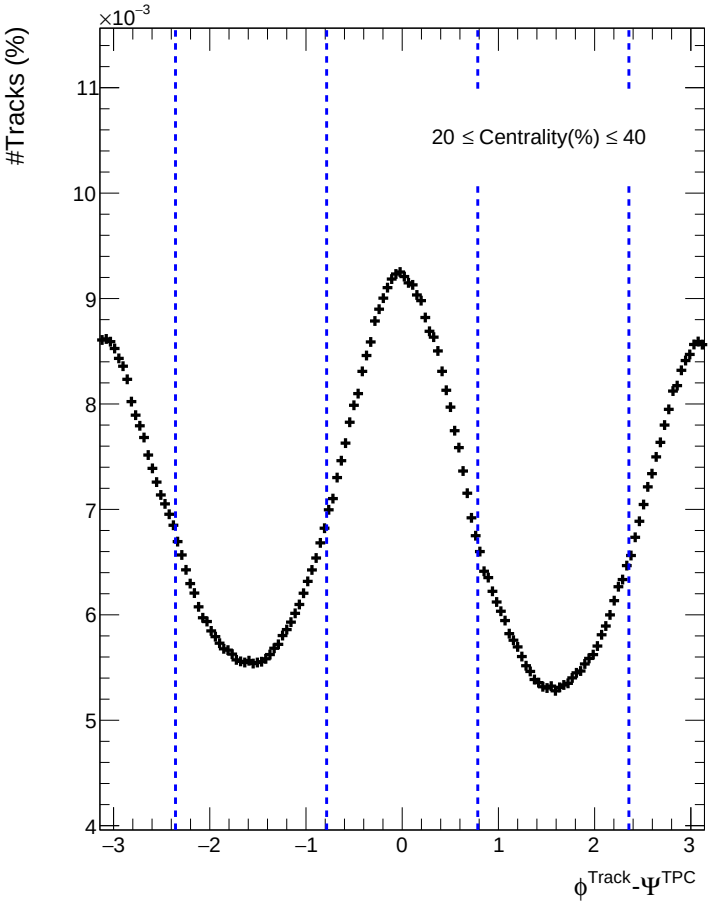

Figure 5.3: Electron and positron candidate distribution as function of $\Delta\phi$ in the centrality interval from 20-40%. The vertical blue dashed lines indicate the in- and out-of-plane bin borders.

visible in the electron and positron track distributions as function of $\Delta\phi$, depicted in figure 5.3. Indicated by blue, dashed lines are the borders between the in- and out-of-plane regions. Between the maximum and the minimum amount of tracks, a factor $\sim 1.5 - 2$ is observed. This variation of the track density could induce differences in the track reconstruction and the particle identification performance as function of $\Delta\phi$. As a first check whether further corrections have to be applied to the data before the extraction of $v_2^{\mathrm{J}/\psi}$ is done or not, the track reconstruction quality variables of the TPC and $n\sigma_{\mathrm{Particle}}^{\mathrm{TPC}}$ have been measured as function of $\Delta\phi$. The average of the number of clusters in the TPC per track (left), $n\sigma_{\mathrm{Particle}}^{\mathrm{TPC}}$ (center) and χ^2 over the number of clusters in the TPC (right) as function of $\Delta\phi$, is given in figure 5.4. There is no significant systematic variation visible between the in- and out-of-plane regions and the absolute values of the measured averages correspond to expected numbers. In the given case $n\sigma_{\mathrm{Particle}}^{\mathrm{TPC}}$ does not correspond to the post calibrated value (see section 4.6.1), hence, the deviation from zero is expected. The width of

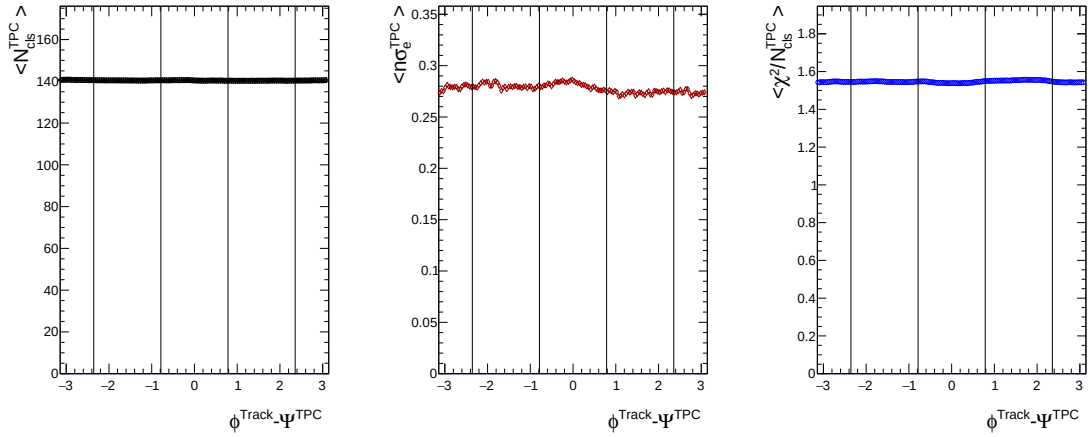

Figure 5.4: From left to right: the average number of clusters per track in the TPC, $n\sigma^{\mathrm{TPC}}_{\mathrm{Particle}}$ and χ^2 over the number of clusters in the TPC as function of $\Delta\phi$.

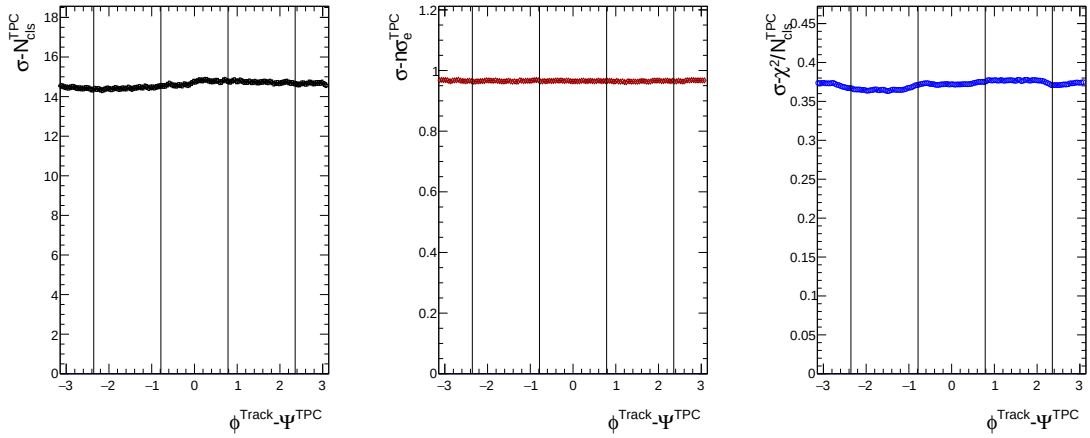

Figure 5.5: From left to right: the width (σ) of the distributions of the number of clusters per track in the TPC, $n\sigma^{\mathrm{TPC}}_{\mathrm{Particle}}$ and χ^2 over the number of clusters in the TPC as function of $\Delta\phi$.

the distributions presented in 5.4 is depicted in figure 5.5. Similar to the averages of the distributions, no significant dependence on $\Delta\phi$ is observed. In conclusion, the measured distributions do not show any significant indication that the J/ψ reconstruction efficiency should vary in a relevant manner as function of $\Delta\phi$. Next to the track reconstruction quality in the TPC, the track density could influence the matching efficiency between the TPC and the ITS and by that influence the J/ψ reconstruction efficiency. To identify a potential variation of the track matching efficiency between the in- and out-of-plane regions of an event is measured. In this case the efficiency is defined as the ratio of all tracks successfully reconstructed in the TPC and the ITS over those successfully reconstructed in the ITS:

$$\epsilon_{\mathrm{match}} = \frac{N^{\mathrm{TPC+ITS}}_{\mathrm{trk}}}{N^{\mathrm{ITS}}_{\mathrm{trk}}}. \tag{5.8}$$

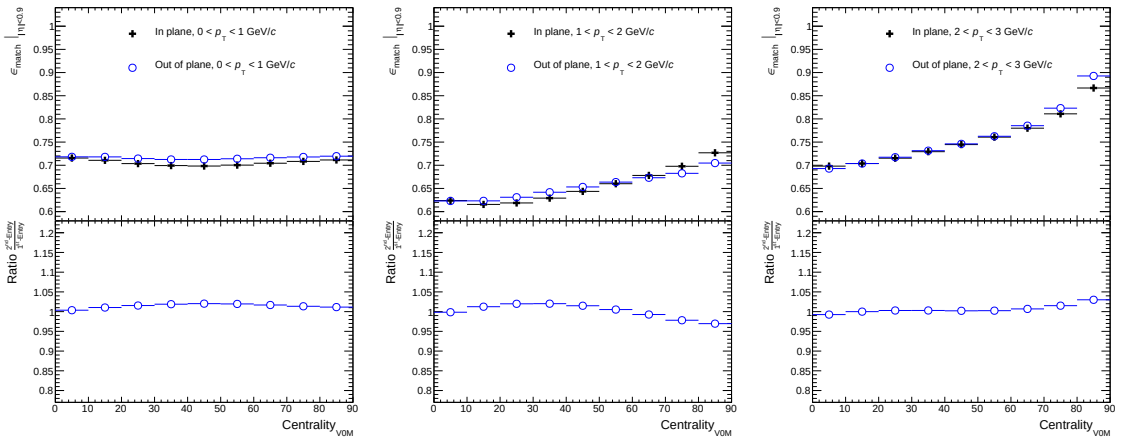

Figure 5.6: Ratio of the tracks successfully reconstructed in the TPC and those successfully reconstructed in the ITS as function of the collision centrality

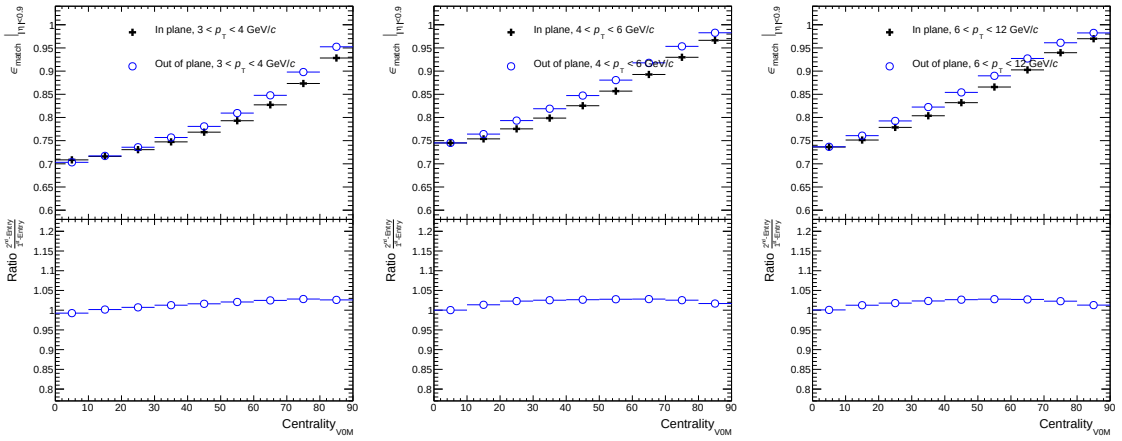

Figure 5.7: Ratio of the tracks successfully reconstructed in the TPC and the ITS and those successfully reconstructed in the ITS as function of the collision centrality

The results are depicted in figures 5.6 for the p_{T} ranges: 0-1 GeV/c, 1-2 GeV/c and 2-3 GeV/c and 5.7 for the p_{T} ranges: 3-4 GeV/c, 4-6 GeV/c and 6-12 GeV/c. The top part of the figures show the track matching efficiency (see equation 5.8) as function of the collision centrality for the in-plane (black crosses) and out-of-plane (blue circles) region. In the bottom part of the figures, the ratio of the efficiency measured in-plane and out-of-plane is given. For all p_{T} and centrality regions, the variation between the in- and out-of-plane track matching efficiency is below 4%. An even smaller variation of the matching efficiency is observed in the semi-central events, especially in the p_{T} region between 2 and 4 GeV/c ($\epsilon_{\mathrm{out}}/\epsilon_{\mathrm{in}} < 2\%$). With respect to the statistical and systematical uncertainties of the results (see section 5.4) from the analysis, this variation should be negligible and thus no additional correction is applied. This can be underlined by calculating the artificially induced elliptic flow due to varying J/ψ reconstruction efficiencies between the in- and out-of-plane regions: under the assumption that the difference of the matching efficiency translates one-to-one into

the J/ψ reconstruction efficiency, a 5% difference ($\epsilon_{\text{out}}/\epsilon_{\text{in}} = 5\%$) would lead to an artificially created $v_2^{\text{J}/\psi}$ of:

$$v_2^{\text{J}/\psi} = \frac{\pi}{4 \cdot R_2} \frac{S_{\text{in}} - S_{\text{out}}}{S_{\text{in}} + S_{\text{out}}} = \frac{\pi}{4 \cdot R_2} \frac{100 - 105}{100 + 105} = -0.022. \tag{5.9}$$

This value is already small compared to the statistical and systematic uncertainties of the measurement. However, since the majority of J/ψ decay electrons lead to better reconstructed tracks than those from electrons of background sources (see Monte Carlo simulation results in section 4.5), presumably a larger part of the difference of the matching efficiencies between the in- and out-of-plane $\Delta\phi$ regions is driven by tracks not originating from J/ψ decays. Thus, probably less then 50% of the difference between the matching efficiencies translate into varying reconstruction efficiencies. Combined with a more realistic value of 2% for the variation itself, this leads to an artificial elliptic flow of $v_2^{\text{J}/\psi} = -0.0044$, which corresponds to about 3% of the observed $v_2^{\text{J}/\psi}$ values and their statistical and systematic uncertainties.

5.4 Results

The highest significance for a non-zero J/ψ elliptic flow is expected in semi-central collisions. To prove that a non-zero J/ψ elliptic flow exists, events in the range of the 20-40% most central collisions are selected. As discussed in chapter 2, different p_{T} distributions are expected for direct and regenerated J/ψ. To improve the access to the predicted distinctions for $v_2^{\text{J}/\psi}$ between regenerated and direct J/ψ , the variations of the p_{T} distributions are utilized by measuring $v_2^{\text{J}/\psi}$ as function of p_{T} in three different p_{T} intervals:

$$\text{bin} - 1 : 0 \leq p_{\text{T}} \leq 2 \text{ GeV}/c, \tag{5.10}$$
$$\text{bin} - 2 : 2 \leq p_{\text{T}} \leq 6 \text{ GeV}/c, \tag{5.11}$$
$$\text{bin} - 3\text{a} : 6 \leq p_{\text{T}} \leq 100 \text{ GeV}/c \text{ and} \tag{5.12}$$
$$\text{bin} - 3\text{b} : 4 \leq p_{\text{T}} \leq 12 \text{ GeV}/c. \tag{5.13}$$

Based on the p_{T} measurements and theoretical calculations, the largest amount of regenerated J/ψ and therefore J/ψ which should inherit elliptic flow, are expected in the range from 2 (GeV/c) $\leq p_{\text{T}} \leq$ 6 (GeV/c). Unfortunately, the statistical precision of the analyzed data sample does not allow a meaningful signal extraction in the p_{T} range from 6 (GeV/c) $\leq p_{\text{T}} \leq$ 100 (GeV/c), see figure 5.10 for example. Therefore, for the final $v_2^{\text{J}/\psi}$ measurement with the "fit method" a small variation of the last p_{T} range was applied. As a result bin-2 and bin-3b (see eq. 5.11 and 5.13) have a small overlap. Nevertheless, the elliptic flow, as measured with the fit method, is quoted with respect to the mean p_{T} of all J/ψ used for the $v_2^{\text{J}/\psi}$ extraction and hence, bin-3 still provides valuable information.

5.4.1 In- and out-of-plane method

Due to the division into subsamples the in- and out-of-plane method suffers stronger than the fit method from the limited statistics of the analyzed data sample. Depicted in the figures 5.8, 5.9 and 5.10 are the invariant mass spectra in- (left panels) and out-of-plane (right panels) in the three p_{T} bins. The spectra are based on the event, track and pair selection procedure introduced in chapter 4. From those spectra, the

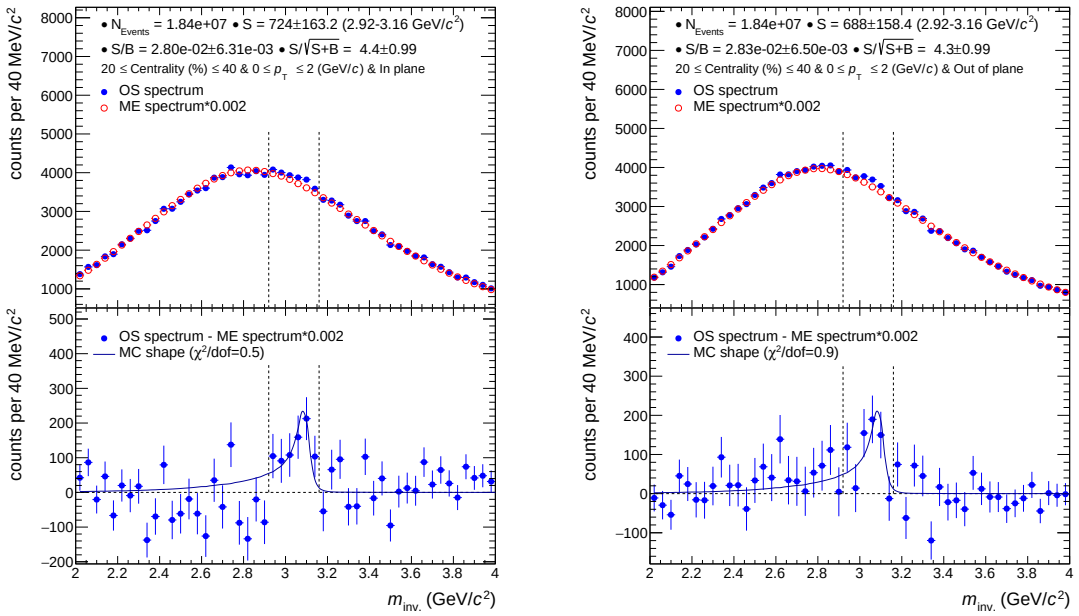

Figure 5.8: Left panel: In-plane dielectron invariant mass spectrum in the J/ψ transverse momentum (p_{T}) range of 0-2 GeV/c. Right panel: Out-of-plane dielectron invariant mass spectrum in the J/ψ transverse momentum (p_{T}) range of 0-2 GeV/c.

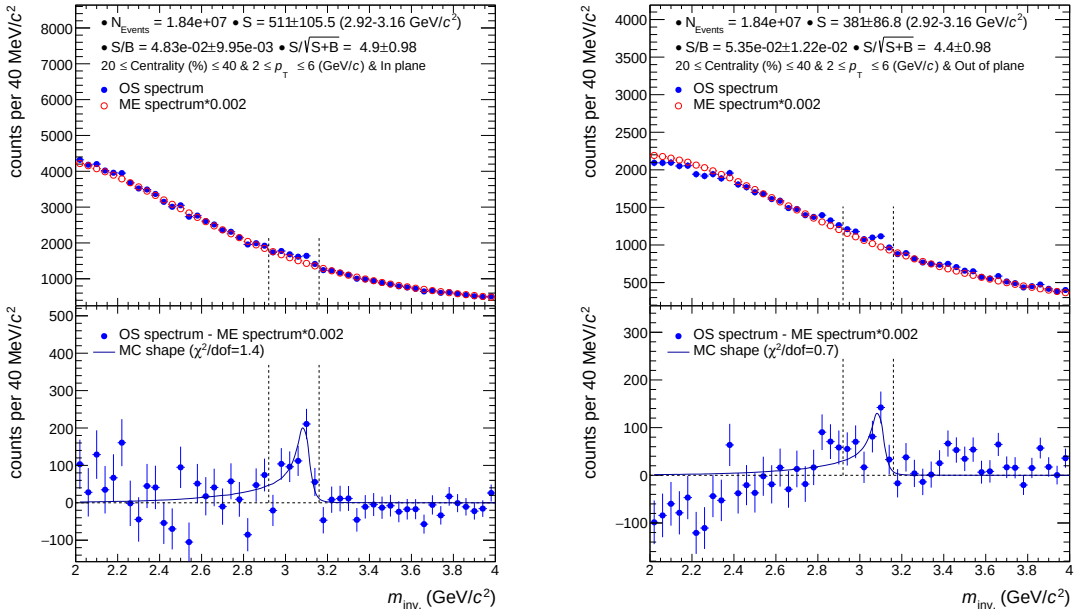

Figure 5.9: Left panel: In-plane dielectron invariant mass spectrum in the J/ψ transverse momentum (p_{T}) range of 2-6 GeV/c. Right panel: Out-of-plane dielectron invariant mass spectrum in the J/ψ transverse momentum (p_{T}) range of 2-6 GeV/c.

J/ψ yield to calculate the elliptic flow is extracted. Especially for bin-3, it is difficult to correctly extract the yield from the given spectra. Already for bin-1 and bin-2

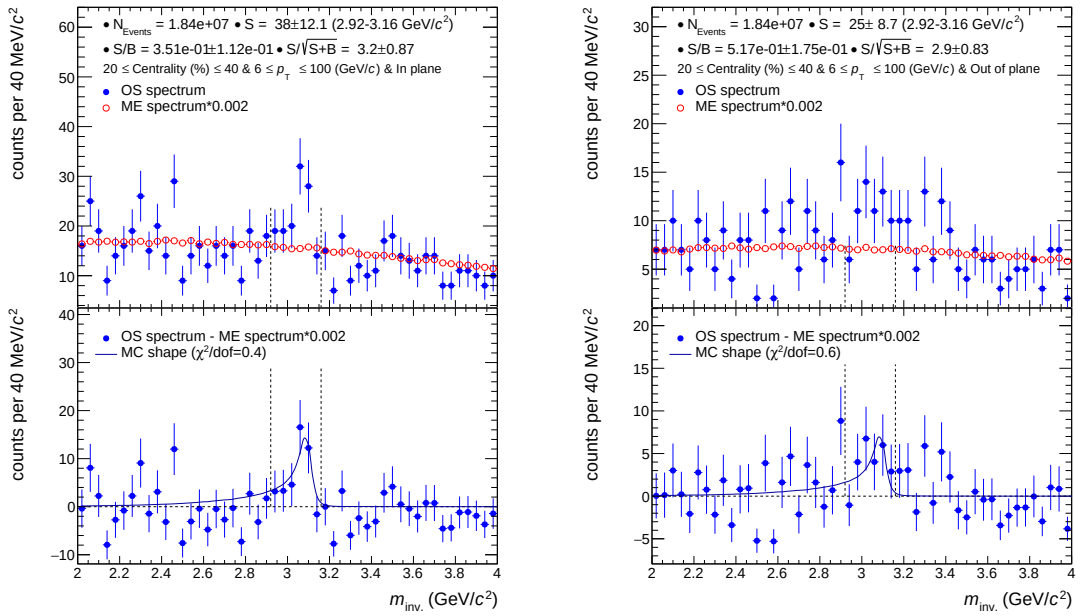

Figure 5.10: Left panel: In-plane dielectron invariant mass spectrum in the J/ψ transverse momentum (p_{T}) range of 6-100 GeV/c. Right panel: Out-of-plane dielectron invariant mass spectrum in the J/ψ transverse momentum (p_{T}) range of 6-100 GeV/c.

the significance for the J/ψ resonance measurement is below 5σ, for bin-3 it is even below 3σ for the out-of-plane spectrum. Thus, the reliability of the results of the $v_2^{\mathrm{J}/\psi}$ measurement, based on the given data sample and in the given collision centrality range, is difficult to evaluate. Nevertheless, for completeness $v_2^{\mathrm{J}/\psi}$ measured in the p_{T} ranges 0-2 GeV/c, 2-6 GeV/c and 6-100 GeV/c with the in- and out-of-plane method is presented in figure 5.11. Due to the large statistical uncertainties, the measurement does not allow a conclusive statement on the question, whether the produced J/ψ show any elliptic flow or not.

5.4.2 Fit method

Since the fit method, in contrast to the in- and out-of-plane method, extracts an integrated signal over the full $\Delta\phi$ range its statistical precision does not suffer from an additional binning. Thus, it is the preferred method for the extraction of a final $v_2^{\mathrm{J}/\psi}$ result.

5.4.2a Systematic uncertainties

To estimate the quality and reliability of the results extracted with the fit method, those parts of the analysis, where a systematic influence might be introduced, were explicitly studied. Table 5.1 summarizes the parts, of which a systematic influence on the results was reviewed. The upper panel of figure 5.12 depicts $v_2^{\mathrm{J}/\psi}$ for the systematic variations introduced to the signal-extraction method. Each labeled block, limited by the tick marks, in the lower panel corresponds to the results of all signal-extraction alterations for a given modification of the track sample. The study does not give any clear indications for a preferable approach between the

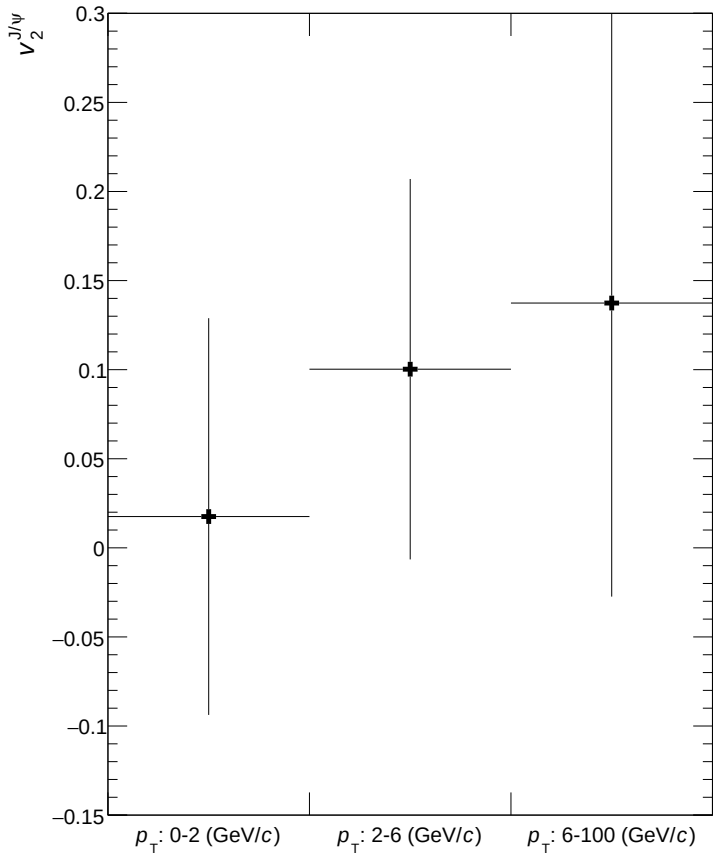

Figure 5.11: Elliptic flow of J/ψ ($v_2^{\mathrm{J}/\psi}$) measured in three different transverse momentum (p_{T}) ranges with the in- and out-of-plane method. Based on the yield extraction from the invariant mass spectra shown in figures 5.8, 5.9 and 5.10.

different alterations. The systematic influence of the different modifications of the signal-extraction method seems to be similar for all track samples in first order. Nevertheless, the influence on the results is still significantly smaller than the statistical uncertainty. A variation of the pion-rejection criterion towards a looser criterion seems to systematically influence the result towards lower values for $v_2^{\mathrm{J}/\psi}$. The looser criterion probably introduces a larger pion contamination, which could lead to an overestimation of the elliptic flow of the background and hence, artificially decrease the observed value for $v_2^{\mathrm{J}/\psi}$. At first glimpse, a tighter pion-rejection also seems to systematically decrease the results for $v_2^{\mathrm{J}/\psi}$. However, under application of the tight rejection criterion, also values on the upper edge of the total variations for $v_2^{\mathrm{J}/\psi}$ are observed. Hence, a clear recognition of a systematic behavior is not given. Taking into account that a tighter criterion implies a further decrease of the statistical precision, it is most likely that the differences of the results are due to the enlarged statistical fluctuations. Except for a few outliers, all results from the systematic variations for $v_2^{\mathrm{J}/\psi}$ agree within their given statistical uncertainties.

Such a study of the systematic behavior was performed for all p_{T} ranges of the analysis with the TPC and also the V0C detector as event-plane estimator. To estimate the systematic uncertainty of the final result, a value for $v_2^{\mathrm{J}/\psi}$ was extracted for each modification of the signal-extraction method on every track sample alteration. Since the variation between the extracted $v_2^{\mathrm{J}/\psi}$ values could also simply originate

Description	Variations
Event selection	
Out-of-bunch pileup: $N^{\text{TPC}}_{\text{tracks}} < 5.13 \cdot 10^{-6} \cdot \text{V0M}^2_{\text{amp.}} + 0.5 \cdot \text{V0M}_{\text{amp.}} + p$ $N^{\text{TPC}}_{\text{tracks}} > 8.13 \cdot 10^{-6} \cdot \text{V0M}^2_{\text{amp.}} + 0.3 \cdot \text{V0M}_{\text{amp.}} + p$	$p = \{750,\ 1000,\ 1500\}$ $p = \{-750,\ -1250\}$
z_{vtx}-position difference: $\lvert z^{\text{SPD}}_{\text{vtx}} - z^{\text{Global Tracks}}_{\text{vtx}} \rvert < 0.2$ mm	required not required
Track selection	
TPC track reconstruction quality: $0 \leq \chi^2_{\text{TPC}}/N^{cls}_{\text{TPC}} \leq p$	$p = \{2.5,\ 2.75,\ 3\}$
Particle identification	
Electron selection: $p_1 \leq n\sigma^{\text{TPC}}_e \leq p_2$ Post calibration	$p_1 = \{-2,\ -2.5,\ -3\}$ $p_2 = \{2.5,\ 3\}$ active/not active
Pion rejection: $p \leq n\sigma^{\text{TPC}}_\pi$	$p_1 = \{3.5,\ 4.5\}$
J/ψ signal extraction	
Background estimator	Event mixing Like sign
Signal determination method	Bin counting MC fit integration
Signal determination range	$2.92 \leq m_{\text{inv.}} \leq 3.16$ GeV/c^2 $2.85 \leq m_{\text{inv.}} \leq 3.20$ GeV/c^2
Resolution of $m_{\text{inv.}}$ measurement	40 MeV/c^2 80 MeV/c^2
$v_2^{J/\psi}$ extraction	
v_2^B estimation function	3rd or 4th order polynomial
v_2^B estimation range	$2.6 \leq m_{\text{inv.}} \leq 3.5$ GeV/c^2 $2.32 \leq m_{\text{inv.}} \leq 3.76$ GeV/c^2 $2 \leq m_{\text{inv.}} \leq 4$ GeV/c^2
v_2^B width of signal exclusion range	$2.92 \leq m_{\text{inv.}} \leq 3.16$ GeV/c^2 $2.88 \leq m_{\text{inv.}} \leq 3.26$ GeV/c^2 $2.84 \leq m_{\text{inv.}} \leq 3.26$ GeV/c^2

Table 5.1: Systematic variations of the $v_2^{\text{J}/\psi}$ extraction.

from statistical fluctuations, a check of the statistical significance of the variation with the so-called "Barlow criterion" is done [105]. If a variation does not exceed a significance of one σ:

$$\frac{|< v_2^{J/\psi} > - v_{2,\ i}^{J/\psi}|}{|\text{stat. uncert.}(< v_2^{J/\psi} >)^2 - \text{stat. uncert.}(v_{2,\ i}^{J/\psi})^2|} > 1, \tag{5.14}$$

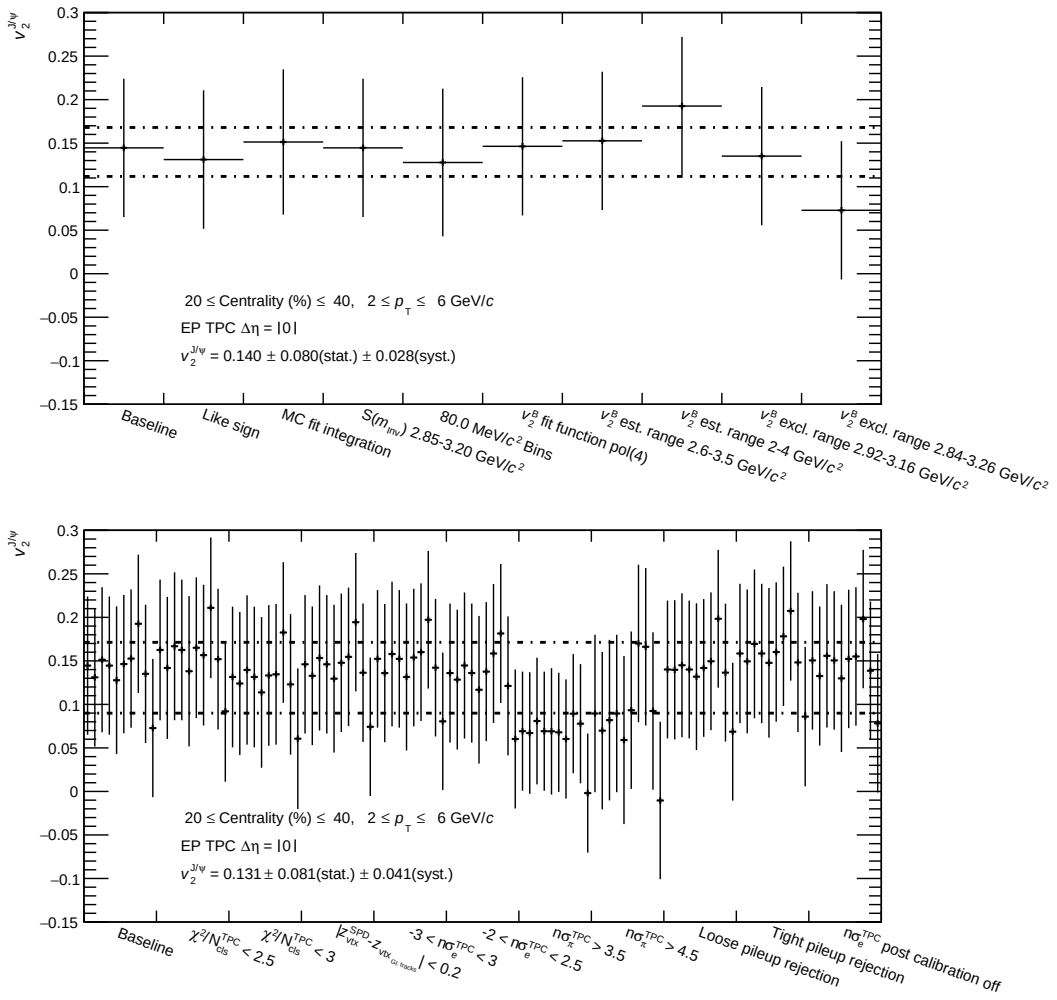

Figure 5.12: Elliptic flow of J/ψ ($v_2^{\mathrm{J}/\psi}$) as function of the systematic variations indicated by the bin label. Upper panel: signal-extraction variations performed on the baseline track sample. Lower panel: signal-extraction variations performed on the varied track sample, as indicated by the bin label. The dash-dotted lines correspond to the systematic uncertainty estimated from the variations, with their center of gravity on the average $v_2^{\mathrm{J}/\psi}$ of all variations.

it is labeled as statistical fluctuation and removed from the distribution of the results. The final value for the systematic uncertainty corresponds to the standard deviation of the distribution of results accepted by the Barlow criterion.

5.4.2b J/ψ elliptic flow as function of p_{T}

The quoted elliptic flow corresponds to the average of all systematic variations, accepted by the Barlow criterion, weighted with their statistical significance. Hence, a result with a smaller statistical uncertainty has a larger influence on the quoted result compared to a result with a larger uncertainty. As mentioned before, the placement of the quoted $v_2^{\mathrm{J}/\psi}$ along the p_{T}-axis corresponds to the measured mean p_{T} of all reconstructed J/ψ in the given p_{T} bin. The mean p_{T} is extracted with the same methodical approach as the $v_2^{\mathrm{J}/\psi}$ measurement based on the fit method.

The results of the $v_2^{\mathrm{J}/\psi}$ measurement as function of p_{T} are presented in figure 5.13. Unfortunately, the statistical uncertainties are quite large also for the fit method.

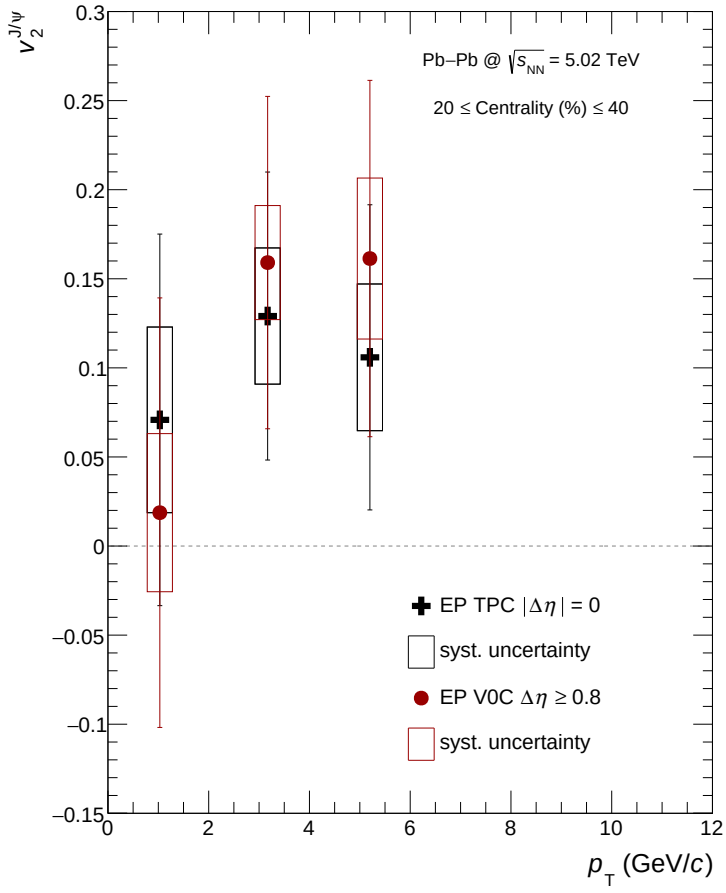

Figure 5.13: Elliptic flow of J/ψ ($v_2^{\mathrm{J}/\psi}$) as function of the transverse momentum (p_{T}), extracted via the fit method, based on the TPC (black crosses) or the V0C (red circles) as event-plane estimator.

Nevertheless, in the p_{T} range from 2−6 GeV/c, a hint for a non-zero J/ψ elliptic flow with a significance of 2.7 σ is observed based on the TPC as detector providing the event-plane estimation. Actually, the measured value for $v_2^{\mathrm{J}/\psi}$ in this p_{T} range, with the event-plane estimation from the V0C, is even larger. However, due to the slightly worse event-plane resolution, the statistical significance for a non-zero elliptic flow is smaller. The larger $v_2^{\mathrm{J}/\psi}$ from the measurement with the V0C also supports the statement that non-flow effects due to auto correlations in the measurement with the TPC are negligible.

5.5 Comparison to theory and other measurements

In similar manner like the measurements presented in this thesis, the elliptic flow of J/ψ was measured at forward rapidity in $\sqrt{s_{\mathrm{NN}}}$ = 5.02 TeV Pb−Pb collisions. Hence, an obvious comparison of the elliptic flow of J/ψ measured at mid-rapidity is the one with the measurement at forward rapidity. In the left panel of figure 5.14 $v_2^{\mathrm{J}/\psi}$ measured at forward (green diamonds) and at mid-rapidity (black crosses) is presented [106]. Both results are reconstructed from the 20-40% most central events and correspond to the $v_2^{\mathrm{J}/\psi}$ of inclusive J/ψ. While at mid-rapidity the

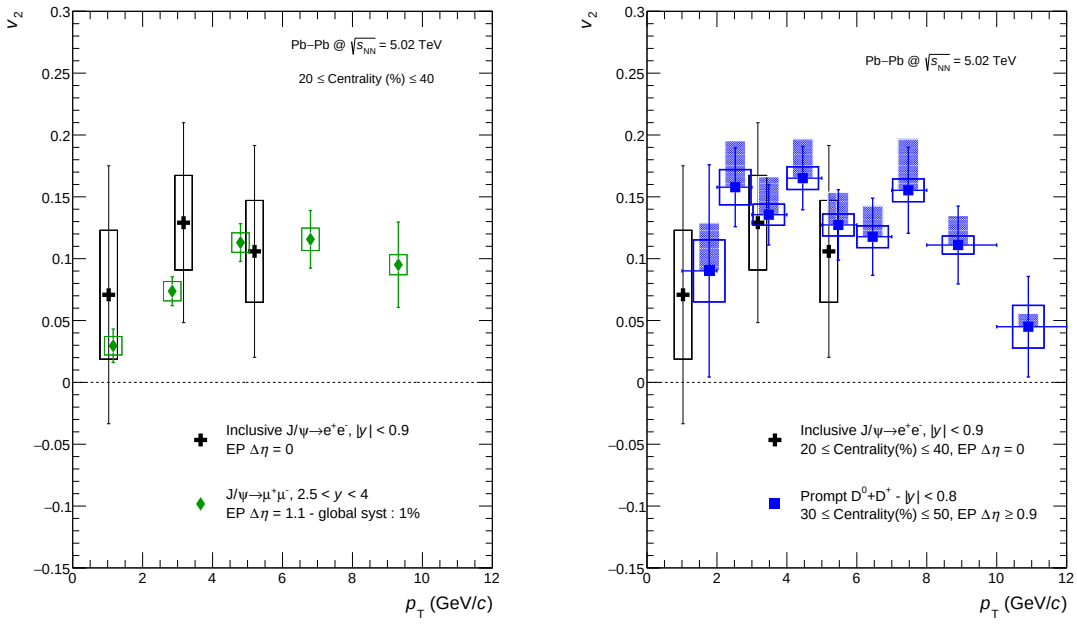

Figure 5.14: Left panel: elliptic flow of J/ψ ($v_2^{\mathrm{J}/\psi}$) measured at forward (green diamonds) and mid-rapidity (black crosses) [106]. Right panel: D-meson (blue squares) and J/ψ (black crosses) elliptic flow measured at mid-rapidity [107].

largest $v_2^{\mathrm{J}/\psi}$ is observed for $\langle p_{\mathrm{T}} \rangle \approx 3\mathrm{GeV}/c$, at forward rapidity it between around $\langle p_{\mathrm{T}} \rangle \approx 5\mathrm{GeV}/c$ and $\langle p_{\mathrm{T}} \rangle \approx 7\mathrm{GeV}/c$. However, due to the size of the statistical uncertainties, the reliability of the determined peak position at mid-rapidity is small. At mid-rapidity, $\sigma_{\mathrm{c\bar{c}}}$ is larger compared to forward rapidity, which seems to result in a larger $R_{\mathrm{AA}}^{\mathrm{J}/\psi}$ (see figure 2.10) for central events at mid-rapidity. Based on the regeneration approach and the predicted p_{T} distribution of regenerated J/ψ, the observed larger $v_2^{\mathrm{J}/\psi}$ at mid-rapidity in the p_{T} range of $2-6$ GeV/c is plausible. However, it is not clear why the absolute value for $v_2^{\mathrm{J}/\psi}$ at forward rapidity, at $p_{\mathrm{T}} \approx 6$ GeV/c goes up to the same level as observed at mid-rapidity at lower p_{T}. In the right panel of figure 5.14, a comparison of the results for $v_2^{\mathrm{J}/\psi}$ at mid-rapidity with the v_2 measurement of D-mesons [107] is given. Compatible values are observed within the statistical uncertainties. Clear interpretations of the results are difficult due to the large uncertainties of the $v_2^{\mathrm{J}/\psi}$ measurement. Still, a slightly steeper increase of v_2 at low p_{T} might be visible in the results from the D-meson measurement. Due to the mass difference of J/ψ- and D-mesons, and under the assumption that the c$\bar{\mathrm{c}}$ quarks forming J/ψ- and D-mesons are subject to the same collective effects, such a behavior would be expected. However, a detailed analysis of the shift of the spectra could offer further information on the collective behavior of heavy quarks, but is not possible due to the uncertainties. The thermalization time of charm quarks (τ_{Charm}) estimated from the comparison of model calculations with the D-meson v_2 measurement is $\tau_{\mathrm{Charm}} \approx 3-14$ fm/c. This allows a full charm thermalization during the QGP phase [107]. Thus, the compatibility of the maxima of the measured v_2 values for D-mesons and J/ψ hint towards a J/ψ regeneration from fully thermalized charm quarks.

Finally, a comparison of the measured results at forward and mid-rapidity with estimations from both transport models introduced in section 2.4.3b is presented in figure 5.15 [106]. The model calculations are able to separate the primordially

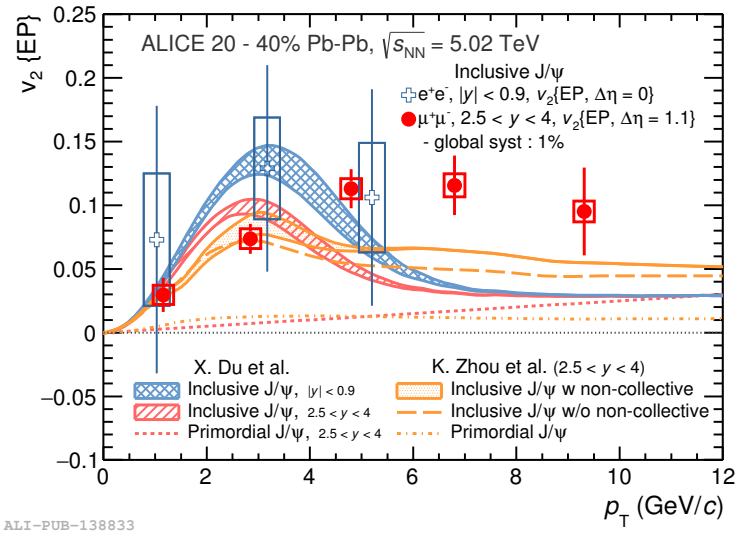

Figure 5.15: Elliptic flow of J/ψ ($v_2^{J/\psi}$) as function of p_T measured at forward (red circles) and mid-rapidity (blue crosses) compared to transport model calculations provided by Du and Rapp and Zhou et al. [1, 55]. [106]

produced J/ψ from the regenerated J/ψ, as introduced in the description of the models in section 2.4.3b. In the figure, the primordial J/ψ are represented by a red dotted and yellow dash-dotted line, while the inclusive J/ψ (red, blue and yellow bands) represent the combination of primordial and regenerated J/ψ. The result of this separation follows the theoretical expectation that primordial J/ψ are not significantly subject to collective effects and show an almost vanishing v_2. On the other hand, regenerated J/ψ which represent the difference between the inclusive and primordial calculations of the models show a significant elliptic flow in the low p_T region. This is in agreement with the concept that those c$\bar{c}$ quarks (re)combining to a J/ψ at later stages of the collision interacted heavily with the collective medium during the QGP phase. In addition, a non-collective component is introduced to the J/ψ production in the model by Zhou et al. This component generates additional elliptic flow of the J/ψ over a wide range of p_T, due to modifications of the J/ψ production induced by a strong magnetic field in the early stages of the collision. Unfortunately, only Du and Rapp provided a calculation at mid-rapidity. In the low p_T area both model calculations for the inclusive J/ψ production agree well with the experimental data. However, at higher transverse momenta $p_T \gtrsim 6$ GeV/c the model calculations and the data measured at forward rapidity diverge, which might hint towards a missing production mechanism in the models. Analyses of p−Pb collisions at $\sqrt{s_{NN}} = 5.02$ TeV and $\sqrt{s_{NN}} = 8.16$ TeV, with particle multiplicities compatible with semi-central Pb−Pb events, show a comparable $v_2^{J/\psi}$ in the higher p_T area, where the divergence from the model calculations is observed [108]. The results of those analyses are given in figure 5.16. The similarity of the observed $v_2^{J/\psi}$ at higher p_T brings up the question whether the potentially missing production mechanism is correlated to a QGP phase or to CNM effects. However, it is not clear that the $v_2^{J/\psi}$ must have the same origin in p−Pb and Pb−Pb collisions, even though it is observed at similar p_T. In addition, several measurements in p−Pb collisions give results which have been interpreted as signature of collectivity up to now (e.g. [109]).

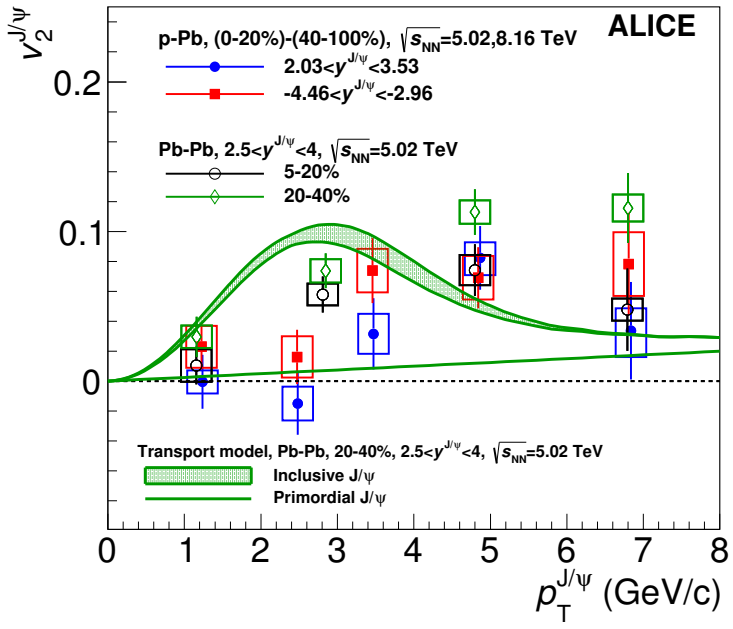

Figure 5.16: Elliptic flow of J/ψ ($v_2^{\mathrm{J}/\psi}$) as function of the transverse momentum (p_{T}) measured at forward rapidity in Pb−Pb collisions at $\sqrt{s_{\mathrm{NN}}} = 5.02$ TeV (black circles and green diamonds) and p−Pb collisions at $\sqrt{s_{\mathrm{NN}}} = 5.02$ TeV and $\sqrt{s_{\mathrm{NN}}} = 8.16$ TeV (blue circles and red squares) [108].

Thus, the clear separation of p−Pb collisions, collective effects, a QGP phase and the correlated interpretation of the results appears to be difficult at LHC collision energies. Comparing the results in p−Pb collisions to those in Pb−Pb collisions at mid-rapidity a different course of $v_2^{\mathrm{J}/\psi}$ is visible, especially around a transverse momentum of 3 GeV/c, where the J/ψ production in Pb−Pb collisions should be dominated by the regeneration component. Hence, a more precise measurement of $v_2^{\mathrm{J}/\psi}$ at mid-rapidity should be able to shed further light on the J/ψ production mechanisms. Hopefully, already the Pb−Pb data sample recorded with ALICE in the fall of 2018, amongst other setups with a semi-central collision trigger, will be able to provide a higher statistical precision. It should contain up to a factor ~ 2 more semi-central collisions, compared to the data sample used for the analysis presented in this thesis.

6 J/ψ measurements and the ALICE TRD

Clearly, multi-differential high precision measurements of J/ψ are able to put strong constraints on models that try to describe the quarkonia production in heavy-ion collisions. However, at mid-rapidity, the precision of the J/ψ measurement is limited due to systematical and statistical uncertainties. Whereas for the first Pb−Pb data taking in 2010 and 2011 only $\sim 50\%$ of the Transition Radiation Detector (TRD) was installed, the installation of the TRD was finished before the restart of the LHC in 2015. Hence, in first order, full azimuthal acceptance from the TRD is available in the Pb−Pb data sample recorded late 2015. Up to now, the PID information from the TRD has not been included into J/ψ reconstruction strategies at mid-rapidity for this data sample.

In this chapter, a fully efficiency-corrected measurement of the nuclear modification factor of J/ψ ($R_{\mathrm{AA}}^{\mathrm{J}/\psi}$) as function of the number of participating nucleons (N_{part}), utilizing the additional PID information from the TRD, will be presented. This includes a description of:

- the strategy how the TRD is included,
- the influences on the reconstruction efficiencies as function of p_{T},
- a comparison of the resulting reconstructed yields and the according significance of the signal
- and a comparison of the $R_{\mathrm{AA}}^{\mathrm{J}/\psi}$ and its statistical uncertainties with and without the TRD.

6.1 Strategy to include the TRD

The principles of particle identification with the TRD are described in section 3.2.1c. Up to now, the TPC is utilized to identify electrons for inclusive J/ψ analyses at mid-rapidity (see section 4.6.1). Additional PID information from the TRD can help to increase the purity of the electron sample selected with the TPC and enable to access those electrons rejected by the hadron exclusion criteria of the TPC. As mentioned in section 3.2.1c, a special feature of the ALICE TRD is the variation of the signal shape between tracks with and without transition radiation (see figure 3.10). To utilize the time dependence of the variations of the signal shape, likelihood calculations for up to seven time slices, referred to as dimensions, of the signal are prepared. The pion efficiency (ϵ_π), defined as $\epsilon_\pi = \frac{N_\pi^{\mathrm{Acc.}}}{N_\pi^{\mathrm{Acc.}}+N_\pi^{\mathrm{Rej.}}}$, for the different signal analysis methods of the TRD as function of the track momentum is depicted in the left panel of figure 6.1. Presented are values, measured at a fixed electron efficiency (ϵ_e), defined as $\epsilon_e = \frac{N_e^{\mathrm{Acc.}}}{N_e^{\mathrm{Acc.}}+N_e^{\mathrm{Rej.}}}$, of 90% and based on tracks that produced a signal in six layers of the TRD. The smallest ϵ_π is observed with the 7D likelihood (LQ7D) or

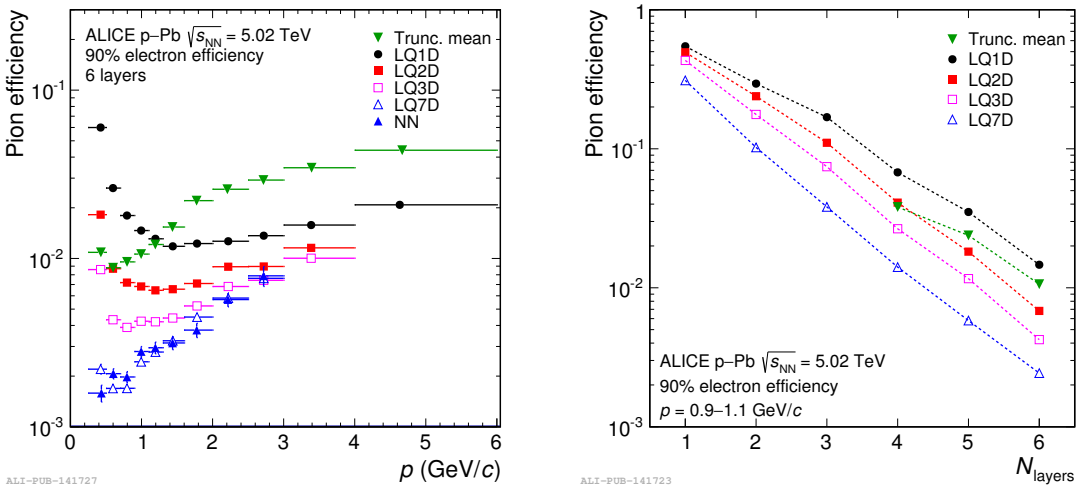

Figure 6.1: Pion efficiency as function of the track momentum (left panel) and as function of the number associated layers with hits (right panel), for the different particle identification methods of the TRD [75].

a neural network (NN) calculation, although towards large momenta the difference to the other methods decreases and the performance of the 2D, 3D, 7D likelihood and the neural network becomes comparable. Above track momenta of 3 GeV/c, the loss of time slices in the TRD readout signal reaches a relevant level. Hence, the advantage in terms of pion suppression of those methods utilizing several time slices to provide PID informations decreases. Based on the given PID performances and their dependence of the track momenta and quality, for this initial study the 2D likelihood method is used as compromise between performance and stability.

ϵ_π as function of the number of layers with a hit associated to a given track, further on referred to as tracklet, is given in the right panel of figure 6.1. A similar decrease of ϵ_π with the increase of the number of tracklets is observed for all presented methods. For the 2D likelihood method ϵ_π below 10% is achieved with three and more tracklets associated to a track. To ensure a lower limit of the achieved purity of the electron sample selected with the TRD, the TRD PID information is only used for tracks with at least three associated tracklets:

$$N_{\text{trkl}}^{\text{TRD}} \geq 3. \tag{6.1}$$

This criterion corresponds to a pion-rejection factor of at least 10. Additionally, before the TRD information is utilized, it is required by a selection on the χ^2 that the reconstructed track from the global tracking algorithm is well matched to the TRD tracklets:

$$0 \leq \frac{\chi^2_{\text{TRD}}}{N_{\text{trkl}}^{\text{TRD}}} \leq 5. \tag{6.2}$$

In the left panel of figure 6.2 the electron candidates selected by the TPC (black crosses) and those of them that satisfy the TRD track quality criteria (blue circles) as function of their momentum are given. In the bottom pane of the left panel the ratio of the two electron samples is presented. About 45% of the TPC electron candidates meet the TRD track quality criteria. The right panel of the figure shows the average number of tracklets per track as function of the tracks η and φ orientation. Along φ the structures of the 18 TRD supermodules and along η the segmentation into five

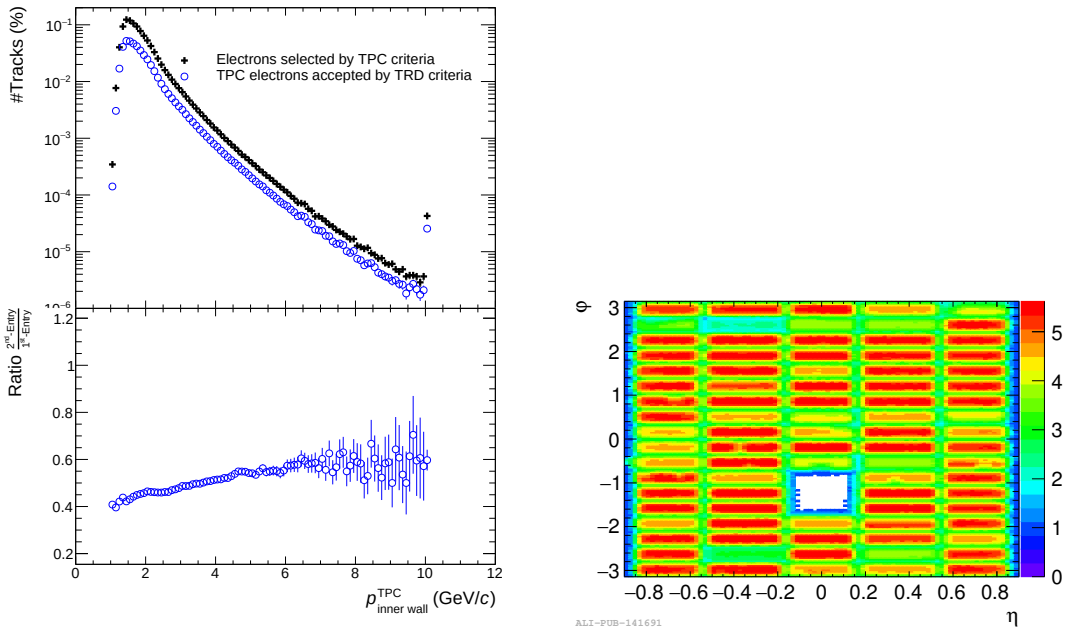

Figure 6.2: Left panel: number of electron track candidates selected with the TPC (black crosses) as function of the track momentum and those electron track candidates fullfilling the TRD track quality criteria given by the equations 6.1 and 6.2. The bottom part shows the ratio of both track samples. Right panel: average number of TRD tracklets for a general track sample as function of η and φ [75].

stacks per supermodule are visible. The gap around $\eta \sim 0$ and $\varphi \sim -1$ corresponds to the so-called "PHOS hole", where no TRD chambers are installed to increase the data quality of the ALICE PHOS detector. Large variations between the average number of tracklets are visible between the stacks and supermodules. For some stacks the average number of tracklets, even in the center of the stack, is already below four. The figure in the right panel partly explains the low number of tracks satisfying the TRD track quality criteria, compared to the TPC-only track sample in the left panel. The rather low efficiency is not a principle problem of the TRD, but strongly effected by local inefficiencies, i.e. single chambers not working properly. Obviously, the low track efficiency is an issue which has to be taken into account by any method including the TRD into the particle identification for $J/\psi \rightarrow e^+e^-$ analyses.

To ensure that no electron candidate selected by the TPC is lost due to the TRD, an approach was developed which does not apply any TRD selection on the track sample selected with TPC information. Tracks within the 3σ electron band of the TPC, but rejected due to the hadron exclusion criteria of the TPC (see section 4.6.1 and equations 4.35 and 4.36), are reevaluated taking the TRD PID information into consideration. Therefore, the probability for a track to be an electron as calculated from the TRD 2D likelihood ($P(\mathrm{TRD}^{e^\pm}_{2\mathrm{D}})$), based on the $\mathrm{d}E/\mathrm{d}x$ of the particle deposited in the TRD, is utilized. The distribution of $P(\mathrm{TRD}^{e^\pm}_{2\mathrm{D}})$, for the electron candidate sample selected with the TPC, as function of the track momentum (left panel) and the number of tracklets in the TRD (right panel) is given in figure 6.3. First of all, the peak at an electron probability of 0.2 corresponds to the fact that tracks without TRD PID information are set per default to a probability

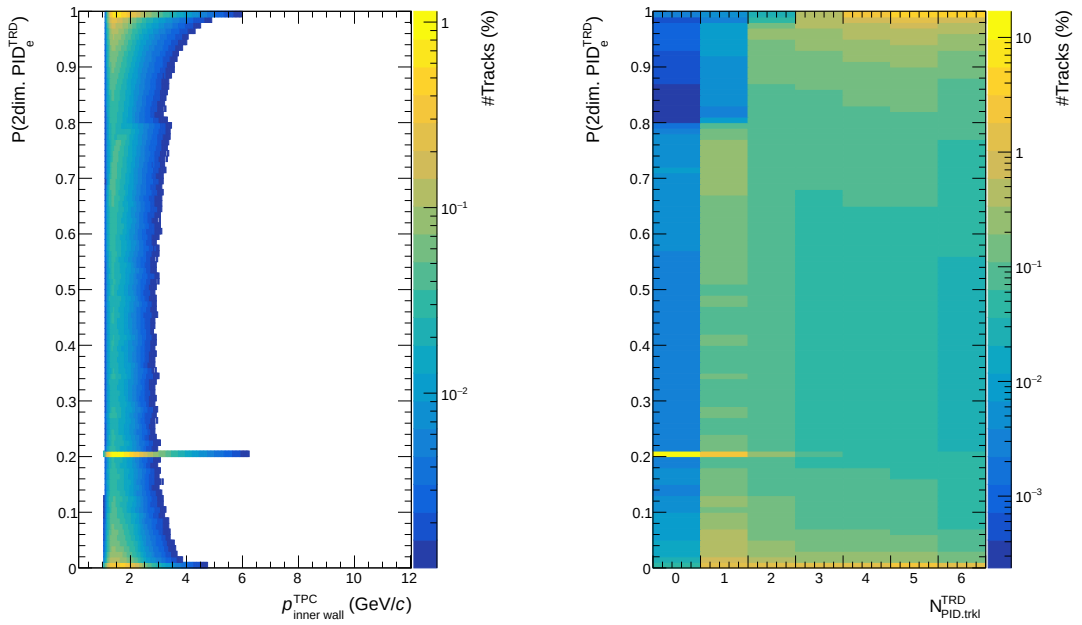

Figure 6.3: Percentage of tracks of the electron sample selected with the Time Projection Chamber (TPC) as function of the momentum and the TRD 2D likelihood electron probability (left panel) and number of TRD tracklets and the TRD 2D likelihood electron probability (right panel).

of 0.2. Over the full momentum range, the TRD primarily measures tracks with $P(\mathrm{TRD}^{e^\pm}_{\mathrm{2D}})$ either close to 1 or close to 0. Thus, a selection criterion based on the electron probability close to 1 should lead to a clean electron sample without loosing many electrons. With more associated tracklets the separation power of the TRD improves. Less tracks are measured with vague PID information, i.e. either a track is measured with $P(\mathrm{TRD}^{e^\pm}_{\mathrm{2D}}) \approx 1$ or $P(\mathrm{TRD}^{e^\pm}_{\mathrm{2D}}) \approx 0$. This observation is in full agreement with the measurement of the pion efficiency as function of the number of TRD layers (see figure 6.1) and supports the requirement of at least three tracklets associated to track for the utilization of TRD PID. Depicted in the three panels of figure 6.4 are the tracks with:

$$P(\mathrm{TRD}^{e^\pm}_{\mathrm{2D}}) \geq 0.99 \tag{6.3}$$

for different TPC selection and rejection criteria. The left panel shows all tracks satisfying equation 6.3, the TRD electron track sample. Based on the TPC measurement, it has to contain a relevant amount of misidentified particles which are found outside the black dashed lines, indicating a three sigma selection of $n\sigma^{\mathrm{TPC}}_{\mathrm{e}^\pm}$. Thus, a high value of $P(\mathrm{TRD}^{e^\pm}_{\mathrm{2D}})$ is required to achieve a clean enough electron sample from the TRD. As a baseline for the analysis, the criteria given in equation 6.3 is used. However, due to the potential contamination, not all tracks fulfilling this criteria are kept, only those tracks within $n\sigma^{\mathrm{TPC}}_{\mathrm{e}^\pm} < \pm 3$ are used for further analyses. Their distribution is given in the center panel. The composition of the standard TPC selected track sample and those tracks in principle rejected by the hadron exclusion of the TPC, but recovered by the TRD, represents the complete track sample and is shown in the right panel of figure 6.4. To summarize the track selection with additional TRD information:

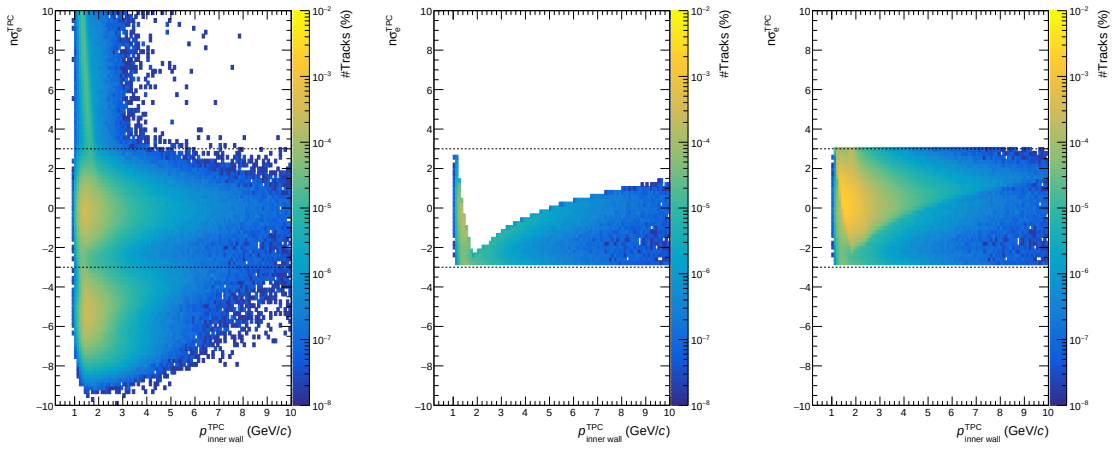

Figure 6.4: Track distributions as function of parametrized specific energy loss for electrons ($n\sigma_{e^\pm}^{TPC}$) and the track momentum, for all tracks with $P(\mathrm{TRD}_{2D}^{e^\pm}) \geq 0.99$ (left), all tracks previously excluded by the TPC with $P(\mathrm{TRD}_{2D}^{e^\pm}) \geq 0.99$ and $|n\sigma_{e^\pm}^{TPC}| \leq 3$ (center) and these tracks combined with the standard TPC electron track sample (right).

- All tracks have to satisfy the track selection criteria given in section 4.5.
- All tracks satisfying the particle identification criteria of the TPC (see section 4.6.1) are selected.
- All tracks within $|n\sigma_{e^\pm}^{TPC}| \leq 3$ and $P(\mathrm{TRD}_{2D}^{e^\pm}) \geq 0.99$ are selected.

In a logical description:

$$\text{Track selection :} \tag{6.4}$$
$$p_T \geq 1\ \mathrm{GeV}/c \wedge 0.9 \leq |\eta| \wedge$$
$$-1.0\ \mathrm{cm} \leq dca_{xy} \leq 1.0\ \mathrm{cm} \wedge -3.0\ \mathrm{cm} \leq dca_{xy} \leq 3.0\ \mathrm{cm} \wedge$$
$$\frac{N_{ITS}^{\text{Shar. cls}}}{N_{ITS}^{cls}} < 0.4 \wedge N_{TPC}^{cls} > 70 \wedge$$
$$0 \leq \frac{\chi^2_{ITS}}{N_{ITS}^{cls}} \leq 5 \wedge 0 \leq \frac{\chi^2_{TPC}}{N_{TPC}^{cls}} \leq 2.75,$$
$$\text{Particle identification :} \tag{6.5}$$
$$\left(-2.5 \leq n\sigma_e^{TPC} \leq 3 \wedge n\sigma_p^{TPC} \geq 3.5 \wedge n\sigma_\pi^{TPC} \geq 3.5\right)$$
$$\vee$$
$$\left(|n\sigma_e^{TPC}| \leq 3 \wedge N_{trkl}^{TRD} \geq 3 \wedge 0 \leq \frac{\chi^2_{TRD}}{N_{trkl}^{TRD}} \leq 5 \wedge P(\mathrm{TRD}_{2D}^{e^\pm}) \geq 0.99\right).$$

A comparison of the resulting electron candidate sample with the TPC-only standard electron candidate sample as function of the track momentum is given in figure 6.5. In both panels of the figure, the distributions of the black crosses represent the TPC-only track sample as reference. The steep increase at low momenta is due to the proton exclusion criteria which has a strong influence at low momenta. The small kink at $p \sim 2$ GeV/c is a result of the deuteron band which is not excluded, crossing the electron band. Also, for both panels, the bottom pane represents the

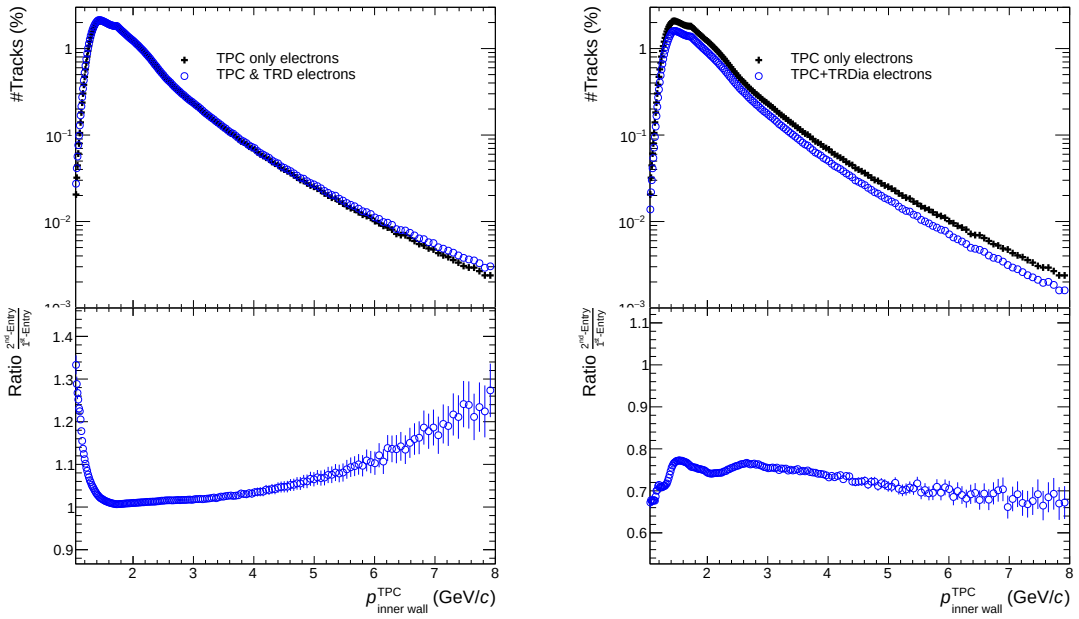

Figure 6.5: Electron candidate distribution as function of the track momentum. In the left panel, the black crosses represent the electron sample selected with the TPC PID, and the blue circles additionally contain those electrons "recovered" by the TRD. The bottom part shows the ratio of the combined sample over the TPC-only sample. In the right panel, the black crosses are again the electron sample selected by the TPC, and the blue circles represent those electrons satisfying the TPC criteria and if they fulfill the conditions of $N^{\mathrm{TRD}}_{\mathrm{trkl}} \geq 3$ and $0 \leq \frac{\chi^2_{\mathrm{TRD}}}{N^{\mathrm{TRD}}_{\mathrm{trkl}}} \leq 5$, they have to satisfy $P(\mathrm{TRD}^{e^{\pm}}_{\mathrm{2D}}) \geq 0.99$.

ratio of the candidate sample variation over the TPC electron sample. In the left panel, the track distribution shown with blue circles represents the result of the application of the selection criteria shown in equation 6.1. The rise of the ratio above one corresponds to the recovery of previously excluded tracks based on the TRD PID information. Due to the principles of the approach, the electron candidates are recovered in the region of the proton and pion exclusion criteria of the TPC. Thus, a clear excess at $p \sim 1$ GeV/c (proton exclusion) and an increasing rise with momentum from $p \sim 3$ GeV/c (pion exclusion) of the ratio is visible. As a reference, the right panel of the figure shows with blue circles a candidate sample, of which the tracks satisfy the combination of the standard TPC selection requirements, and if the tracks satisfy equations 6.1 and 6.2, they also have to fulfill $P(\mathrm{TRD}^{e^{\pm}}_{\mathrm{2D}}) \geq 0.99$. Here, the introduction of the TRD reduces the sample over the full momentum range by about 25%. The dip at $p \sim 1$ GeV/c is due to the worse performance of the TRD in this area which leads to a smaller amount of electrons achieving high electron probabilities in the likelihood calculation. Around $p \sim 2$ GeV/c the rejection of deuterons by the TRD leads to the small dip. Hence, in this small region, it is ensured that the addition of the TRD selection purifies the electron candidate sample. However, since the TPC-only sample does not indicate issues due to a high contamination by particles misidentified as electrons, a loss of 25% is too large compared to the gained purity.

6.2 J/ψ signal extraction

The electron candidate sample, collected by the selection criteria described in the previous section, is passed to the same signal extraction mechanisms as introduced in section 4.7.2. In figure 6.6, invariant mass spectra for two different TPC

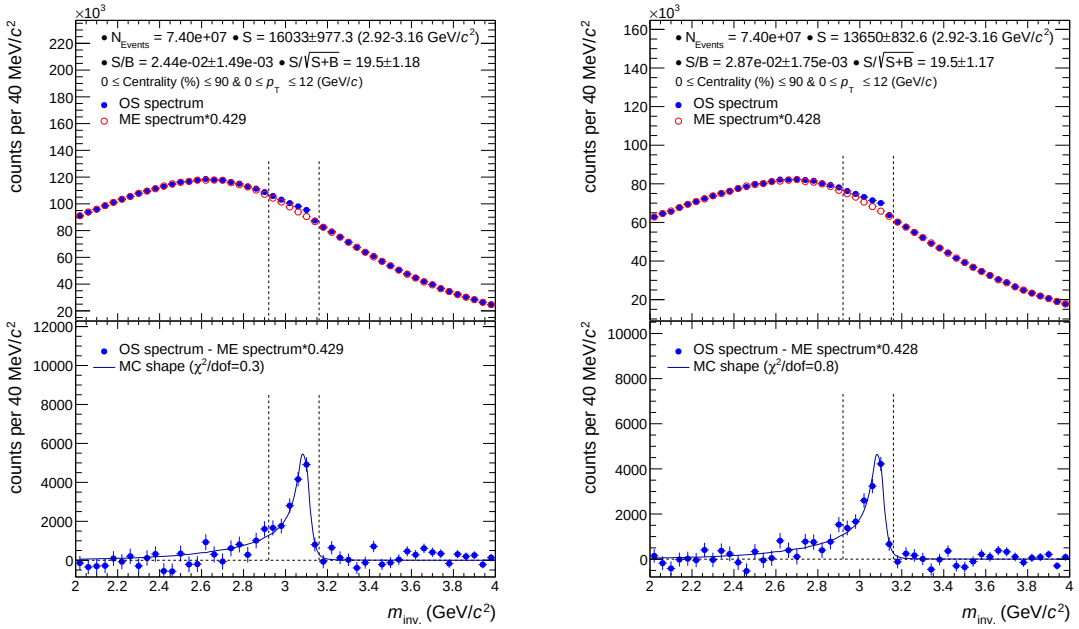

Figure 6.6: Dielectron invariant mass ($m_{\text{inv.}}$) spectra, based on electron candidate samples, containing candidates recovered by the TRD. Left panel: loose TPC proton and pion rejection ($n\sigma_{\text{p}}^{\text{TPC}} \geq 3.5$ & $n\sigma_{\pi}^{\text{TPC}} \geq 3.5$). Right panel: tighter TPC proton and pion rejection ($n\sigma_{\text{p}}^{\text{TPC}} \geq 4$ & $n\sigma_{\pi}^{\text{TPC}} \geq 4$).

hadron exclusion criteria of the TPC (left: $n\sigma_{\text{p}}^{\text{TPC}} \geq 3.5$ & $n\sigma_{\pi}^{\text{TPC}} \geq 3.5$, right: $n\sigma_{\text{p}}^{\text{TPC}} \geq 4$ & $n\sigma_{\pi}^{\text{TPC}} \geq 4$) are depicted. Both are based on electron candidate samples that include tracks recovered by the TRD PID information, which where previously not selected by the TPC. The backgrounds are well described by the mixed-event spectra, and the Monte Carlo signal shape fits well to the extracted signal. Both spectra enable a reconstruction of the J/ψ resonance with a significance of $\sigma = 19.5$ which is 5% larger than for the measurement without the recovered electrons (see figure 4.16). The looser hadron exclusion criteria provide a larger amount of reconstructed signal pairs, but also worsen the signal over background ratio compared to the tighter criteria. No indication is visible that the signal extraction is systematically influenced by the inclusion of the TRD PID information.

6.2.1 Comparison with and without TRD

An increased significance of the inclusive measurement of the J/ψ resonance was achieved by including the TRD PID information. However, more relevant is the investigation of the performance in terms of differential spectra, e.g. the significance as function of the collision centrality or the transverse momentum (p_{T}). Comparisons of S, B and the resulting significance as function of the collision centrality and J/ψ p_{T} are presented in the figures 6.7, 6.8 and 6.9. The ratio of all variations over

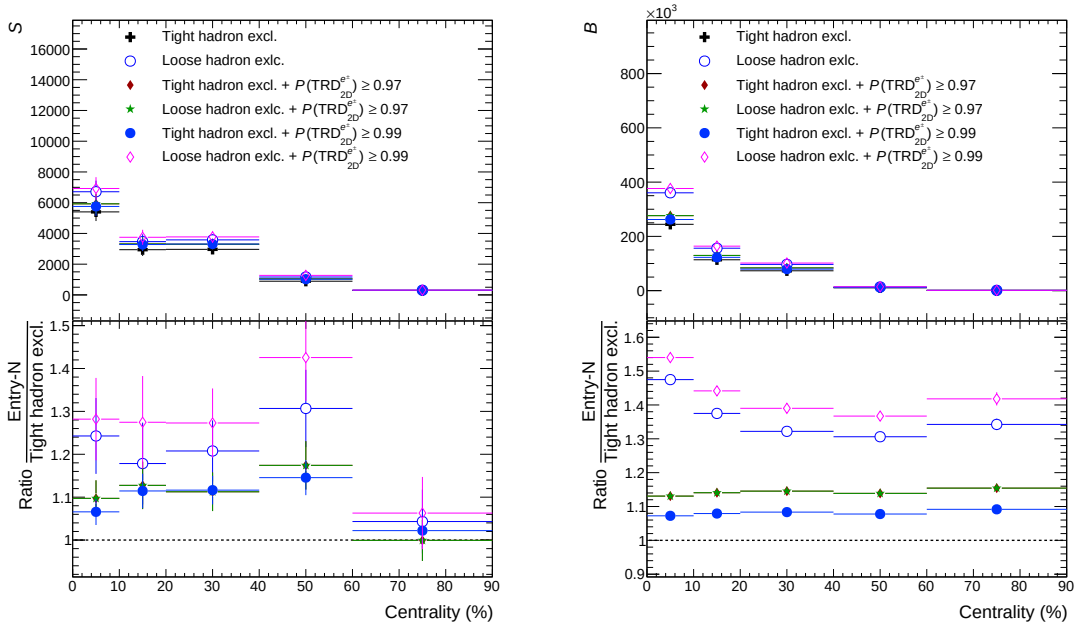

Figure 6.7: Number of signal pairs (S)(left) and number of background pairs (B) (right) as function of the collision centrality, for different Particle IDentification (PID) setups.

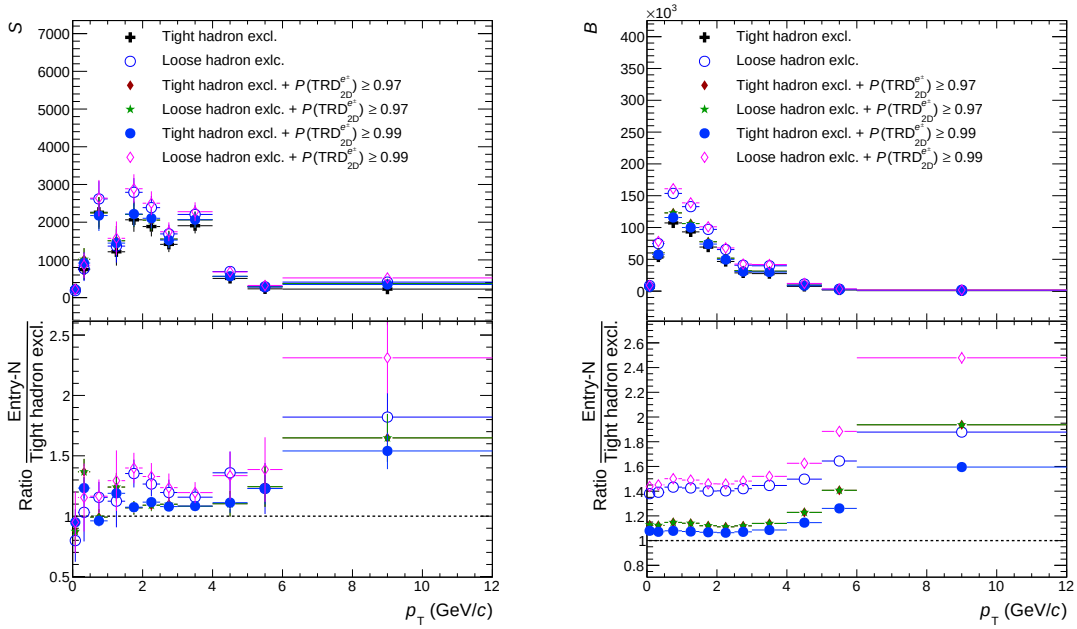

Figure 6.8: Number of signal pairs (S)(left) and number of background pairs (B) (right) as function of the J/ψ transverse momentum (p_{T}), for different Particle IDentification (PID) setups.

the tight hadron exclusion setting without recovered electron candidates is given in the bottom part of each figure. For almost every collision centrality and p_{T} region, the largest S and B yield is observed with the loose hadron exclusion setting and $P(\mathrm{TRD}^{e^{\pm}}_{\mathrm{2D}}) \geq 0.99$ required for the recovery of electron candidates. A similar

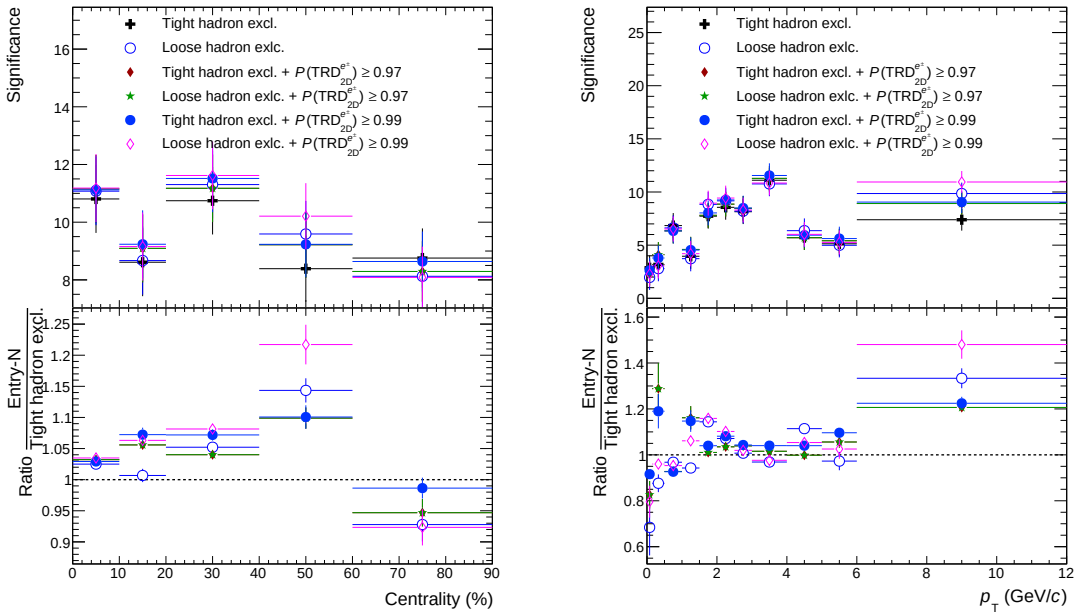

Figure 6.9: J/ψ resonance extraction significance as function of the collision centrality (left) and the J/ψ transverse momentum (p_{T}) (right) for different Particle IDentification (PID) setups.

behavior is visible in the comparison of the results with and without recovered electrons, independent of the detailed setting. Whether the increased signal also leads to an increased significance can be extracted from figure 6.9. The left figure presents the significance as function of the collision centrality and the right figure as function of p_{T}. As function of the collision centrality, the highest significances are achieved in all bins, except for the most peripheral region, with a setting including the TRD. In central and semi-central collisions the "best" results are observed with an electron probability requirement of $P(\mathrm{TRD}^{e^\pm}_{2\mathrm{D}}) \geq 0.99$, the "best" hadron exclusion criteria vary from bin to bin. For the most peripheral collisions, the highest significance is observed without electron candidates recovered by the TRD. However, almost no loss in significance is observed when recovered candidates satisfying the $P(\mathrm{TRD}^{e^\pm}_{2\mathrm{D}}) \geq 0.99$ requirement are added to the track sample. As function of p_{T}, the results are not as significant as for the collision centrality dependent signal extraction. Still, for most of the p_{T} intervals, a gain in significance is observed when the TRD is included. A p_{T}-dependence of the gain in significance is expected, since the recovery of electrons with the TRD has several aspects inducing a track p_{T}-dependence. The results point to the fact that further tuning of the application of the electron recovery with the TRD as function of p_{T} could increase the performance, e.g. by excluding the low track momentum region where the TRD is not able to provide an optimal separation between electrons and protons.

6.3 Monte Carlo simulations

6.3.1 Quality assurance

For the measurement of $R_{\mathrm{AA}}^{\mathrm{J}/\psi}$ a complete efficiency correction of the J/ψ yield is required. A standard approach to extract the J/ψ reconstruction efficiency is based on Monte Carlo simulations. To ensure that the Monte Carlo simulations reproduce the real data well enough, the behavior of low-level variables, like track quality variables, is compared between the simulations and the data. Therefore, the distri-

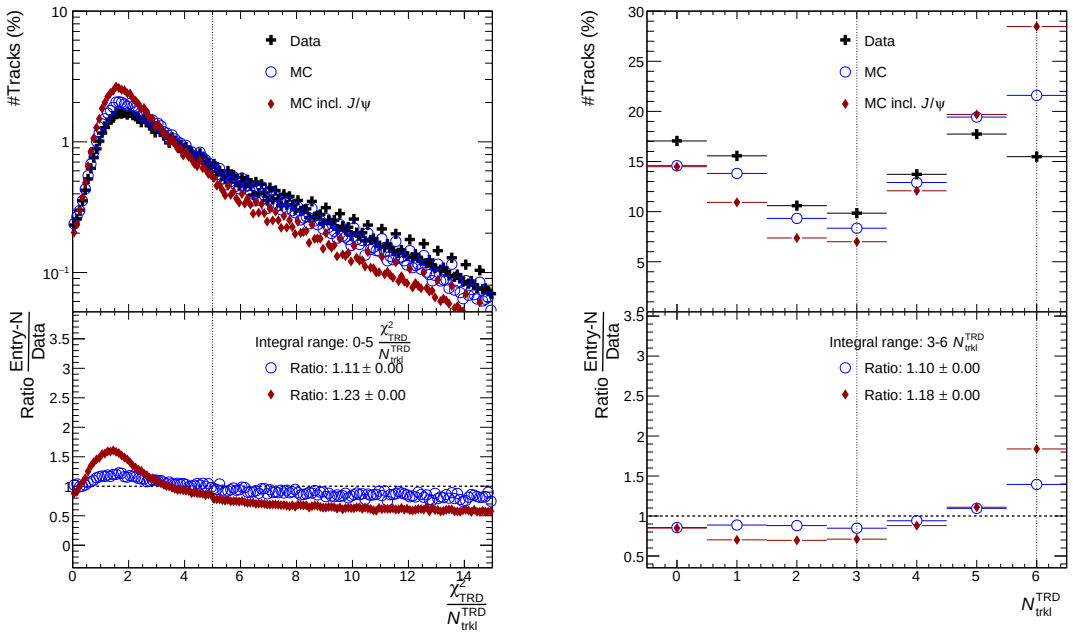

Figure 6.10: $\chi^2_{\mathrm{TRD}}/N^{\mathrm{TRD}}_{\mathrm{trkl}}$ (left panel) and $N^{\mathrm{TRD}}_{\mathrm{trkl}}$ (right panel) distributions measured in real data (black crosses), Monte Carlo (blue circles) and selected Monte Carlo J/ψ electrons (red diamonds).

butions for real data and Monte Carlo of both variables used to ensure the track and PID quality of the TRD measurements are compared. Depicted in the left panel of figure 6.10 are the distributions of $\chi^2_{\mathrm{TRD}}/N^{\mathrm{TRD}}_{\mathrm{trkl}}$ in real data (black crosses), Monte Carlo (blue circles) and selected Monte Carlo J/ψ electrons (red diamonds). The bottom part shows the ratio of the Monte Carlo distributions over the data distribution. A steeper evolution of the distribution is observed in Monte Carlo simulations compared to real data. In the Monte Carlo simulations for inclusive J/ψ, the spectrum peaks around $\chi^2_{\mathrm{TRD}}/N^{\mathrm{TRD}}_{\mathrm{trkl}} \approx 2$ which supports a selection criterion rejecting tracks with large values. Compared to all reconstructed tracks, the Monte Carlo spectrum contains $\sim 10\%$ more tracks in the region below the applied selection criterion of $\chi^2_{\mathrm{TRD}}/N^{\mathrm{TRD}}_{\mathrm{trkl}} \leq 5$. The steps visible in all three distributions towards larger values are a result of the finite number of tracklets that can be assigned to a track. In combination with the correlation between the number of tracklets assigned to a track and the $\chi^2_{\mathrm{TRD}}/N^{\mathrm{TRD}}_{\mathrm{trkl}}$, it is more likely for certain tracks to have higher $\chi^2_{\mathrm{TRD}}/N^{\mathrm{TRD}}_{\mathrm{trkl}}$ than others. The right panel of the figure shows the distributions of $N^{\mathrm{TRD}}_{\mathrm{trkl}}$ for real data (black crosses), Monte Carlo (blue circles) and selected Monte Carlo J/ψ electrons (red diamonds). In Monte Carlo, a significantly larger amount of tracks is reconstructed with six TRD tracklets. In the interval of $N^{\mathrm{TRD}}_{\mathrm{trkl}} \geq 3$,

corresponding to the applied the selection criterion, again $\sim 10\%$ more tracks are observed in Monte Carlo than in real data, with respect to the complete track samples. The electrons from inclusive J/ψ, identified with Monte Carlo informations, are dominantly reconstructed with three and more TRD tracklets. For both distributions it seems that in Monte Carlo $\sim 10\%$ more tracks are measured with a high TRD track quality compared to data. This might hint to the fact that some inefficiencies of the TRD are not included in the Monte Carlo simulation. An analysis of the TPC track variables can be found in [100].

Assuming that the efficiencies of the TPC electron sample are well enough measured, only the representation in Monte Carlo of those electrons recovered with the TRD PID information has to be additionally checked. Given in the left panel

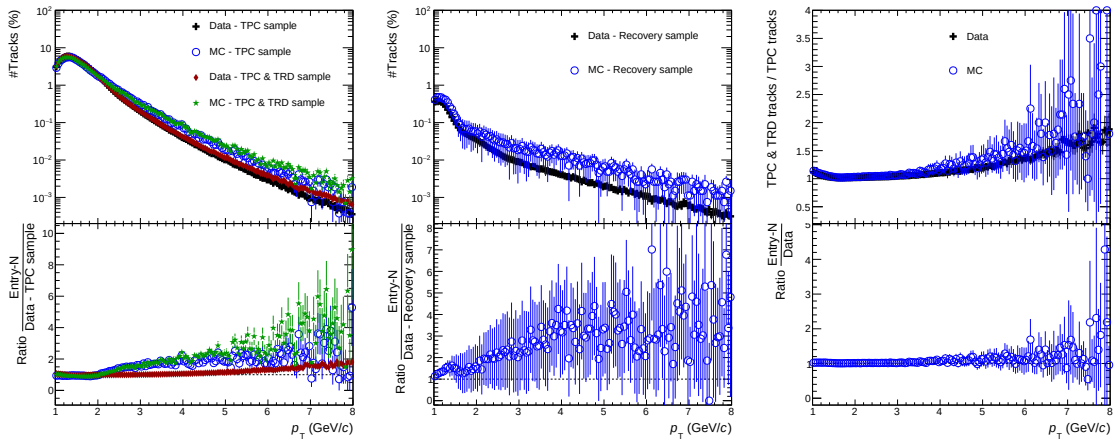

Figure 6.11: Data and Monte Carlo track samples (left and center panel) as function the transverse momentum (p_T). Ratio of the TPC & TRD sample over the TPC measured in real data and Monte Carlo as function of p_T (right panel).

of figure 6.11 are the track distributions with (red diamonds and green stars) and without (black crosses and blue circles) recovered electron candidates as function of p_T, measured in real data (black crosses and red diamonds) and Monte Carlo (blue circles and green stars). Both Monte Carlo samples show a comparable behavior, they slightly undershoot the data at lower p_T and overshoot it at larger p_T. The center panel of the figure shows the comparison between the data (black crosses) and Monte Carlo (blue circles) distribution of the recovered electrons as function of p_T. Both distributions are separately scaled to the number of electrons in the standard TPC sample in real data and Monte Carlo. Within the statistical uncertainties the distribution are in agreement. However, with increasing p_T, more electrons are recovered in the Monte Carlo sample which is in agreement with the observation that $\sim 10\%$ more electron candidates fulfill the TRD selection criteria in Monte Carlo than in real data. The right panel of the figure presents the ratio of the TPC & TRD electron candidates over the TPC-only electron candidates as function of p_T, for data (black crosses) and Monte Carlo (blue circles). The ratio of data and Monte Carlo is in good agreement with unity although, towards larger p_T, the Monte Carlo results start to overshoot the data slightly. The given ratios represent the influence of the recovered electrons on the complete track sample. The good agreement between real data and Monte Carlo supports the assumption that

the recovered electrons are reproduced well enough in Monte Carlo, with respect to their statistical relevance in the full electron candidate sample. Due to the good representation of the ratio of recovered electrons over the standard TPC sample, it is feasible to perform a data-driven efficiency correction for the recovered electron candidates in future analyses, based on the calculation of the efficiencies of the standard TPC sample with Monte Carlo simulations.

6.3.2 Acceptance × efficiency estimation

To calculate the J/ψ reconstruction efficiencies an iterative process was employed, giving access to the efficiencies of several more or less independent selection steps:

- Kinematic selection (J/ψ p_{T} and y),
- Track selection (section 4.5),
- Particle identification (section 6.1),
- Mass window for the yield extraction.

Since the analysis is performed on an AOD data sample, the accessible track sample has already passed a preselection, based on loose track selection criteria. The influence of these criteria on the efficiency is part of the kinematic efficiency calculation, because it is the first selection applied in the iterative process. The reconstruc-

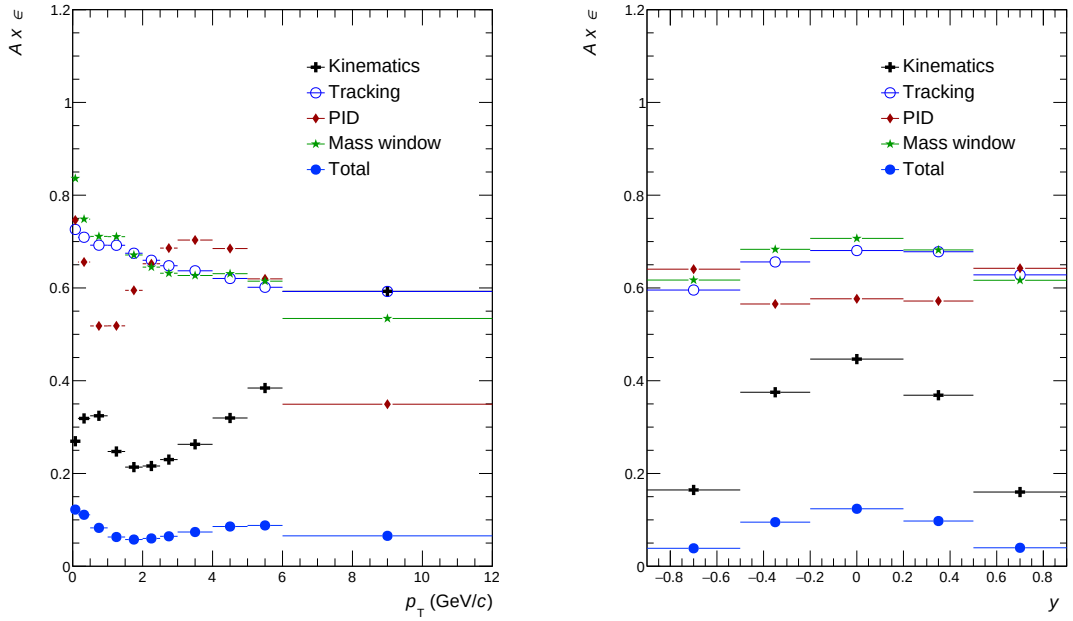

Figure 6.12: J/ψ reconstruction efficiency as function of the transverse momentum (p_{T}) (left) and the rapidity (y) (right).

tion efficiencies as function of p_{T} (left panel) and y (right panel), separated for the kinematic selection (black crosses), track selection (blue open circles), PID (red diamonds), mass window range (green stars) and the corresponding total efficiency (blue full circles) are illustrated in figure 6.12. The dependence on p_{T} and y of the extracted efficiencies including recovered electrons is compatible with the behavior

of the standard TPC sample (see [100]). Since the Monte Carlo simulation does not contain a realistic J/ψ-p_{T} distribution, the extraction of the acceptance times efficiency ($\mathcal{A} \times \epsilon$) as function of the collision centrality has to be based on $\mathcal{A} \times \epsilon$ as function of the collision centrality and p_{T}. In a second step, the p_{T} bins are merged, weighted by a function previously fitted to the measured J/ψ-p_{T} spectrum at forward rapidity. Here the spectrum measured at forward rapidity is used due to the higher statistical precision of the measurement. Depicted in figure 6.13 is

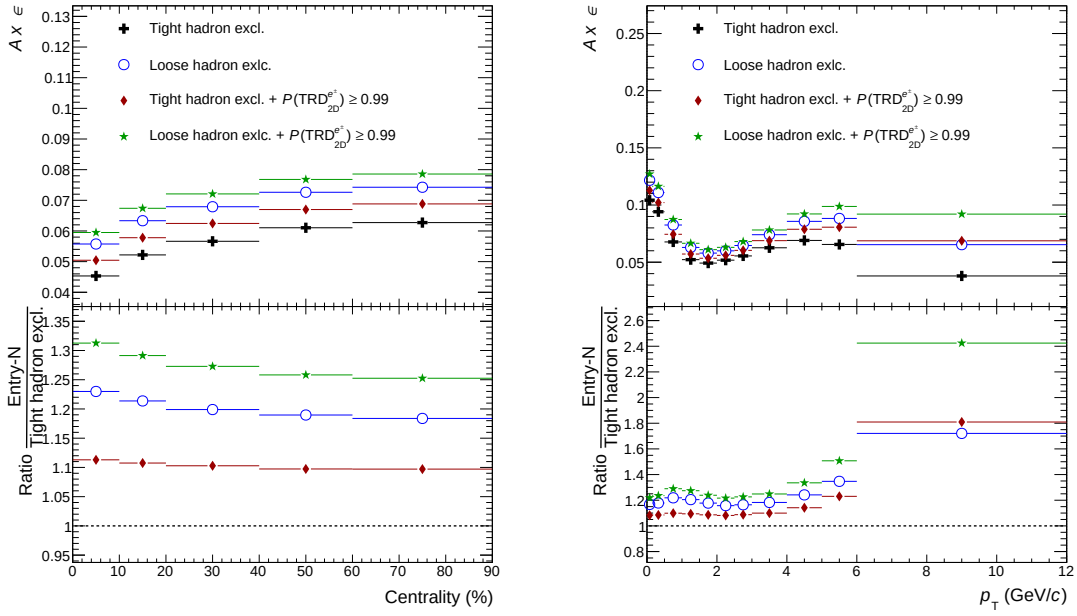

Figure 6.13: Acceptance times efficiency ($\mathcal{A} \times \epsilon$) as function of the collision centrality (left) and the transverse momentum (p_{T}) (right).

$\mathcal{A} \times \epsilon$ as function of the collision centrality (left panel) and p_{T} (right panel), for the previously introduced tight and loose hadron exclusion settings and with and without electrons recovered via TRD information, respectively. As expected from the comparisons of the measured raw yield (see figures 6.7 and 6.8), the highest $\mathcal{A} \times \epsilon$ is observed for the loose hadron exclusion setting together with the TRD-based candidate recovery. The bottom parts of both figures show the ratio using the tight hadron exclusion setting as denominator. For $\mathcal{A} \times \epsilon$ as function of p_{T}, a rise of the ratios with increasing p_{T} is observed. At highest p_{T}, the combination of a tight hadron exclusion and recovered candidates surpasses the loose hadron exclusion setting in terms of $\mathcal{A} \times \epsilon$. This is compatible with the fact that preferably electrons with higher momenta are correctly identified by the TRD and recovered. Hence, more electrons from J/$\psi \rightarrow e^+e^-$ decays are recovered by the TRD than lost due to the stronger pion rejection criterion.

Centrality	0-10%	10-20%	20-40%	40-60%	60-90%
$\langle T_{\mathrm{AA}} \rangle$ (mb^{-1})	23.26	14.4	6.927	2.049	0.3072
$\langle N_{\mathrm{part}} \rangle$	357.3	262.0	159.4	70.74	17.88

Table 6.1: Mean nuclear overlap $\langle T_{\mathrm{AA}} \rangle$ and mean number of collision participants $\langle N_{\mathrm{part}} \rangle$ for a given collision centrality range.

6.4 $R_{\mathrm{AA}}^{\mathrm{J}/\psi}$ as function of N_{part}

The calculation of $R_{\mathrm{AA}}^{\mathrm{J}/\psi}$ is based on equation 2.3 and expanded with the values relevant for the J/$\psi \to e^+e^-$ decay as follows:

$$R_{\mathrm{AA}}^{\mathrm{J}/\psi} = \frac{S}{\left(\mathcal{A} \times \epsilon \cdot N_{\mathrm{Events}} \cdot \Delta y \cdot B.R._{\mathrm{J}/\psi \to e^+e^-}\right) \cdot \left(\langle T_{\mathrm{AA}} \rangle \times \mathrm{d}\sigma_{\mathrm{pp}}^{\mathrm{J}/\psi}/\mathrm{d}y\right)}. \tag{6.6}$$

To extract $R_{\mathrm{AA}}^{\mathrm{J}/\psi}$ as function of N_{part}, the signal as function of the collision centrality, as given in figure 6.7, is used. For $\mathcal{A} \times \epsilon$ as function of the collision centrality the values presented in figure 6.13 are utilized. The rapidity range is $\Delta y = 1.8$ and the used value for the branching ratio is $B.R. = 5.971\%$ [11]. $\langle T_{\mathrm{AA}} \rangle$ denotes the mean nuclear overlap. The values for $\langle T_{\mathrm{AA}} \rangle$ are taken from [89] and summarized in table 6.1 together with the corresponding values for the mean number of collision participants $\langle N_{\mathrm{part}} \rangle$. Both variables are extracted with Monte Carlo Glauber calculations, based on the collision multiplicity. For the J/ψ production cross section in pp collisions $\mathrm{d}\sigma_{\mathrm{pp}}^{\mathrm{J}/\psi}/\mathrm{d}y = 5.64 \pm 0.22$ μb is used [110].

Finally, $R_{\mathrm{AA}}^{\mathrm{J}/\psi}$ (left panel) and the according statistical uncertainty (right panel) as function of $\langle N_{\mathrm{part}} \rangle$ is presented in figure 6.14 for the previously introduced different PID settings. Within the statistical uncertainties the results for the different PID settings agree well. A slight systematic variation between the tight and loose hadron exclusion settings is visible in the first two $\langle N_{\mathrm{part}} \rangle$ intervals ($\langle N_{\mathrm{part}} \rangle < 100$). Whereas in the most peripheral collisions a higher $R_{\mathrm{AA}}^{\mathrm{J}/\psi}$ is observed with the tight setting, in the next $\langle N_{\mathrm{part}} \rangle$ interval the loose setting is systematically higher. Concerning the usage of the TRD, no significant systematic difference is visible between the results with and without the TRD. In the right panel of the figure, an explicit comparison of the statistical uncertainties as function of $\langle N_{\mathrm{part}} \rangle$ for the different PID settings is given. The bottom part depicts the ratio of a given setting with respect to the tight hadron exclusion setting. All three variations of the PID criteria decrease the statistical uncertainty of the $R_{\mathrm{AA}}^{\mathrm{J}/\psi}$ measurement in all bins. Except for the most peripheral bin, the statistical precision of both settings including the TRD succeeds the precision without the TRD. Especially in the most central collisions, the electrons recovered with the TRD increase the statistical precision. Over the full $\langle N_{\mathrm{part}} \rangle$ range, about 5% smaller statistical uncertainties are achieved by including the TRD to recover electrons that were previously excluded by the hadron rejection criteria of the TPC.

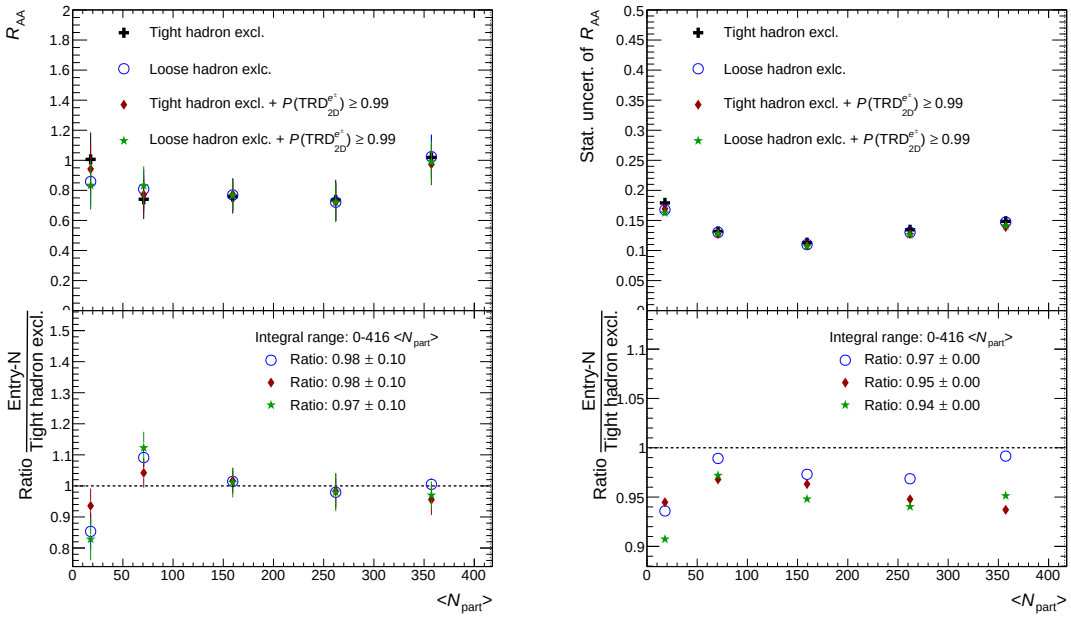

Figure 6.14: $R_{\mathrm{AA}}^{\mathrm{J}/\psi}$ (left) and the statistical uncertainty of $R_{\mathrm{AA}}^{\mathrm{J}/\psi}$ (right) as function of the collision centrality, for different particle identification settings with and without the utilization of TRD information.

7 Summary and outlook

More than 30 years after Matsui and Satz published their idea of "J/ψ suppression by a quark-gluon plasma formation", understanding the J/ψ production in high-energy heavy-ion collisions is still a topic of high interest. It is able to grant access to the behavior of matter under extreme conditions. The second running period of the LHC provided Pb−Pb collisions at an unprecedented collision energy of $\sqrt{s_{\mathrm{NN}}} = 5.02$ TeV. ALICE, the dedicated heavy-ion experiment at the LHC, was able to collect data of about $\mathcal{L}_{\mathrm{int}} \approx 17\ \mu\mathrm{b}^{-1}$ in MB Pb−Pb collisions at mid-rapidity, which provides the possibility to explore J/ψ production mechanisms with unequalled precision.

In this thesis, the current status of the experimental and theoretical knowledge about charmonium production in heavy-ion collisions is summarized in chapter 2. The so-called regeneration mechanism which describes J/ψ production at later collision stages via (re)combination of previously (un)correlated c$\bar{\mathrm{c}}$ quarks seems to play an important role at collision energies in the LHC regime. An observable able to put more constraints on the theoretical models is the elliptic flow of J/ψ. In chapter 3 and 4 the basic principles of J/ψ measurements at mid-rapidity with the ALICE experiment, together with those specific for the 2015 Pb−Pb data sample, are described. Followed by the presentation of the measurement of the elliptic flow of J/ψ in $\sqrt{s_{\mathrm{NN}}} = 5.02$ TeV Pb−Pb collisions at mid-rapidity in chapter 5. In the J/ψ p_{T} range of $2 \leq p_{\mathrm{T}}^{\mathrm{J}/\psi} \leq 6$ GeV/c a non-zero elliptic flow is observed with a significance of 2.7 σ at mid-rapidity. This corresponds to the first observation of a hint that J/ψ produced at mid-rapidity in $\sqrt{s_{\mathrm{NN}}} = 5.02$ TeV Pb−Pb collision are subject to elliptic flow. Predictions of transport models, containing a regeneration component, are in agreement with the observation of a non-zero J/ψ elliptic flow. Nevertheless, the measurements at forward rapidity diverge from the model predictions towards larger p_{T}. Hence, the transport models might not contain all production mechanisms. In chapter 6 a fully corrected, centrality dependent measurement of R_{AA} of J/ψ is presented. The analysis is based on a PID scheme that additionally utilizes information from the TRD to further increase the statistical precision of the measurement. An improvement of the statistical precision of about 5% is observed. With further investigations and a detailed tuning of the application of the TRD information an even larger improvement can be expected.

A measurement of the elliptic flow at mid-rapidity, with enlarged statistical precision, should be able to put strong constraints on the theoretical model descriptions. Thus, it contains the potential to shed further light on the J/ψ production in heavy-ion collisions. Already the Pb−Pb collision data sample recorded in 2018 should provide, due to the applied trigger conditions, enough statistical precision to reduce the statistical uncertainties of the $v_2^{\mathrm{J}/\psi}$ measurement by a factor ~ 2. Also the inclusion of the TRD in the PID scheme of the elliptic flow measurement can improve the statistical precision.

Currently the preparation for the next data taking period with the LHC, the so-called Run3, is ongoing. Several supermodules of the TRD are being reworked to increase the stability of the high voltage. This rework will increase the acceptance and performance of the TRD and thus, reduce the loss of electrons from J/$\psi \rightarrow e^+e^-$ de-

cays. Independent of the performance of the TRD, the new data taking approaches, using a free-streaming concept developed for Run3, should be able to record data samples from Pb−Pb collisions by a factor 50-100 larger than those recorded during Run2. The difference in luminosity between the Run2 forward and mid-rapidity data sample is approximately of the size of: $\sim$ 10: $\mathcal{L}^{\mathrm{fwd}}_{\mathrm{J}/\psi\to\mu\mu} = 10 \times \mathcal{L}^{\mathrm{mid-rapidity}}_{\mathrm{J}/\psi\to ee}$. Hence, the Run3 data sample should allow a high precision measurement of the elliptic flow of J/ψ at mid-rapidity. Based on the measurement at forward rapidity with the Run2 data sample, this should allow a measurement with more than five p_{T} bins in several centrality ranges.

Next to the developments in the high energy regime, many developments are ongoing in the high baryon-density area of the QCD phase diagram. Projects focussing on high baryon-densities in heavy-ion collisions, like the ***Compressed Baryonic Matter*** experiment (CBM) at the future ***Facility for Antiproton and Ion Research*** (FAIR), are able to deliver plenty of important measurements. Subthreshold J/ψ measurements at the SIS-100, possible at the first expansion phase of the FAIR accelerator facilities, have not been performed up to now. In later stages, with larger collision energies, may be even measurements of the J/ψ elliptic flow at high net-baryon densities can be extracted. Such measurements in high precision are important pieces needed to solve the puzzle of quarkonium production in heavy-ion collisions [111, 112].

Appendix A

Statistical uncertainty and significance of the signal

Statistical uncertainty of the signal yield: the quoted statistical uncertainty is calculated from the bin-by-bin uncertainties of the background-subtracted signal spectrum. For each bin, the statistical uncertainty is calculated via Gaussian error propagation from the uncertainties of the opposite-sign and the background spectrum:

$$\Delta S(m_{\text{inv}}^{\text{bin-}i}) = \sqrt{(\Delta N_{+-}(m_{\text{inv}}^{\text{bin-}i}))^2 + (\Delta B(m_{\text{inv}}^{\text{bin-}i}))^2}. \tag{A.1}$$

Within equation A.1 ΔN_{+-} denotes the statistical uncertainty of the opposite-sign spectrum. It is calculated via $\Delta N_{+-} = \sqrt{N_{+-}}$. In similar manner the statistical uncertainty for the background (ΔB) is calculated. However, it is important to note that the calculation is based on the unscaled background spectrum $\Delta B = \sqrt{N_B^{\text{pairs}}} \cdot f_{\text{scale}}^{-1}$. Hence, for the mixed-event technique $\Delta B < \sqrt{B}$. The statistical uncertainty of the integrated signal (ΔS) is calculated from the quadratic sum of the single-bin uncertainties [113]:

$$\Delta S = \sqrt{\sum_{m_{\text{inv.}}\ \text{range}} (\Delta S(m_{\text{inv}}^{\text{bin-}i}))^2}. \tag{A.2}$$

Hence, the uncertainty of the yield is independent of the method utilized for the signal extraction, i.e. "bin counting" or integration of a fitted Monte Carlo J/ψ signal shape.

Significance of the signal: the significance is suppose to evaluate the statistical certainty of a given hypothesis. In the concept of ***hypothesis testing***, the so-called p-value gives a measure that the difference of a given result from the defined null hypothesis is statistically reliable [114]. The significance (Z) is than defined as:

$$Z = \Phi^{-1}(1-p), \tag{A.3}$$

where Φ^{-1} denotes the cumulative distribution function of the unit Gaussian [114]. Hence, the definition of significance is coupled to the definition of the hypotheses tested. Based on a test statistic that follows a Gaussian distribution and can be described with a likelihood ratio Q, the significance can be estimated as:

$$Z = \sqrt{-2\ln Q}. \tag{A.4}$$

In the high-energy physics community a view different hypotheses are utilized to test against [115, 116]. For J/$\psi \to e^+e^-$ analyses within ALICE it is common, to test the signal yield against fluctuations of the inclusive dielectron spectrum. In

other words, the significance gives a measure how certain the signal is not a result of a fluctuation of the dielectron spectrum. A simple approximation of the signal significance, which is used by $J/\psi \to e^+e^-$ analyses within ALICE, is than given by:

$$Z = S/\sqrt{S+B}. \tag{A.5}$$

This and similar approaches, e.g. $Z = S/\sqrt{B}$ or $Z = S/\sqrt{S+2B}$, simplifying the estimation of the significance are also often referred to as *pseudosignificances* [116]. They allow an easy estimation whether the signal extraction was successful and the results of it can be trusted for further analyses. A more sophisticated approach is to plug in the likelihood ratio of a given test scenario into equation A.4. In the case of a test against fluctuations of the dielectron spectrum where $Q = L_{S\ B}/L_B$ this results in:

$$Z = \sqrt{2(S+B)\ln(1+S/B) - 2S}. \tag{A.6}$$

However, to keep the comparability with previous results, it is favorable to stick to the definition from equation A.5.

A discussion of the different behaviors of the definitions for the significance at given signal and background yields can be found in [116]. It is important to note, that neither of the definitions takes the variations of the statistical uncertainties due to different background and signal extraction methods into account, e.g. even though the mixed-event technique leads to a smaller ΔS than the like-sign technique, it will result in the same significance. Also, for a more realistic significance estimation want would need to account for the systematic uncertainties within the signal and background yield extractions.

List of Figures

List of Tables

List of Abbreviations

ALICE A Large Ion Collider Experiment 18

A−A nucleus-nucleus 18

B.R. Branching Ratio 19

CERN Conseil Européen pour la Recherche Nucléaire 11

CGC Color Glass Condensate 23

CIM Comover Interaction Model 28

CNM Cold-Nuclear-Matter 18

CP critical point 16

EoS Equation of State 15

FEE Front-End Electronics 42

ITS Inner Tracking System 36

LEGO Lightweight Environment for Grid Operators 43

LHC Large Hadron Collider 11

LINAC LINear ACcelerator 33

LS like-sign 64

MB Minimum-Bias 42

MC Monte Carlo 45

ME event-mixing 64

mip minimum ionizing particle 40

MRPC Multi-gap Resistive-Plate Chamber 41

MWPC MultiWire Proportional Chamber 36

OS opposite sign 63

p−A nucleon-nucleus 18

PDF Parton Distribution Function 18

PID Particle IDentification 18

pp nucleon-nucleon 17

QA quality assurance 45

QCD Quantum Chromodynamics 11

QED Quantum Electrodynamics 14

QGP Quark-Gluon Plasma 15

RHIC Relativistic Heavy-Ion Collider 21

SBS strong-binding scenario 28

SDD Silicon Drift Detector 36

SHM Statistical Hadronization Model 27

SPD Silicon Pixel Detector 36

SPS Super Proton Synchrotron 17

SSD Silicon Strip Detector 36

TOF Time-Of-Flight detector 41

TPC Time Projection Chamber 35

TRD Transition Radiation Detector 18

UrQMD Ultrarelativistic Quantum Molecular Dynamics 50

WBS weak-binding scenario 28

WLCG Worldwide LHC Computing Grid 43

ZDC Zero Degree Calorimeter 42

ZEM Zero degree Electromagnetic calorimeter 42

ZN Zero degree Neutron calorimeter 42

ZP Zero degree Proton calorimeter 42

List of Variables

Bibliography

[1] X. Du and R. Rapp, "Sequential Regeneration of Charmonia in Heavy-Ion Collisions", Nucl. Phys. **A943**, 147 (2015) 10.1016/j.nuclphysa.2015.09.006, arXiv:1504.00670 [hep-ph].

[2] G. Lemaître, "The beginning of the world from the point of view of quantum theory", Nature **127**, 706 (1931), http://dx.doi.org/10.1038/127706b0.

[3] F. Hoyle, ***The nature of the universe*** (Harper & Brothers, 1960, 1960).

[4] A. I. Eremeeva, "Ancient prototypes of the big bang and the hot universe (to the prehistory of some fundamental ideas in cosmology)", Astronomical & Astrophysical Transactions **11**, 193 (1996) 10.1080/10556799608205465, https://doi.org/10.1080/10556799608205465.

[5] "Evian debut", CERN Courier **32**, 1 (1992), https://cds.cern.ch/record/1732019.

[6] "LHC begins physics with lead ions", CERN Courier **50**, 5 (2010), https://cds.cern.ch/record/1734479.

[7] P. M. Zerwas and H. A. Kastrup, ***QCD — 20 Years Later*** (WORLD SCIENTIFIC, 1993), 10.1142/1755, eprint: https://www.worldscientific.com/doi/pdf/10.1142/1755, https://www.worldscientific.com/doi/abs/10.1142/1755.

[8] J. Book, "J/ψ Production in Pb-Pb Collisions with ALICE at the LHC", PhD thesis (Johann Wolfgang Goethe-Universität, 2014).

[9] W. N. Cottingham and D. A. Greenwood, ***An introduction to the standard model of particle physics***, 2nd ed. (Cambridge University Press, 2007), 10.1017/CBO9780511791406.

[10] D. H. Perkins, ***Introduction to high energy physics***, 4th ed. (Cambridge University Press, 2000), 10.1017/CBO9780511809040.

[11] M. Tanabashi et al. (Particle Data Group Collaboration), "Review of particle physics", Phys. Rev. D **98**, 030001 (2018) 10.1103/PhysRevD.98.030001, https://link.aps.org/doi/10.1103/PhysRevD.98.030001.

[12] E. Noether, "Invariante Variationsprobleme", ger, Nachrichten von der Gesellschaft der Wissenschaften zu Göttingen, Mathematisch-Physikalische Klasse **1918**, 235 (1918), http://eudml.org/doc/59024.

[13] H. L. Anderson et al., "Angular distribution of pions scattered by hydrogen", Phys. Rev. **91**, 155 (1953) 10.1103/PhysRev.91.155, https://link.aps.org/doi/10.1103/PhysRev.91.155.

[14] O. W. Greenberg, "Color: From baryon spectroscopy to QCD", in International Conference on the Structure of Baryons and Related Mesons (Baryons '92) New Haven, Connecticut, June 1-4, 1992 (1992), pp. 130–139, arXiv:hep-ph/9301207 [hep-ph].

[15] V. Khachatryan et al. (CMS Collaboration), "Measurement and QCD analysis of double-differential inclusive jet cross sections in pp collisions at $\sqrt{s} = 8$ TeV and cross section ratios to 2.76 and 7 TeV", JHEP **03**, 156 (2017) 10.1007/JHEP03(2017)156, arXiv:1609.05331 [hep-ex].

[16] U. W. Heinz and M. Jacob, "Evidence for a new state of matter: An Assessment of the results from the CERN lead beam program", (2000), arXiv:nucl-th/0002042 [nucl-th].

[17] I. Arsene et al., "Quark–gluon plasma and color glass condensate at rhic? the perspective from the brahms experiment", Nuclear Physics A **757**, First Three Years of Operation of RHIC, 1 (2005) https://doi.org/10.1016/j.nuclphysa.2005.02.130, http://www.sciencedirect.com/science/article/pii/S0375947405002770.

[18] R. Stock, ed., ***Encyclopedia of applied high energy and particle physics*** (2009), http://www.wiley-vch.de/publish/dt/books/bySubjectPH00/ISBN3-527-40691-3.

[19] B. Friman et al., "The CBM physics book: Compressed baryonic matter in laboratory experiments", Lect. Notes Phys. **814**, pp.1 (2011) 10.1007/978-3-642-13293-3.

[20] J. Adam et al. (ALICE Collaboration), "Direct photon production in Pb-Pb collisions at $\sqrt{s_{\rm NN}} = 2.76$ TeV", Phys. Lett. **B754**, 235 (2016) 10.1016/j.physletb.2016.01.020, arXiv:1509.07324 [nucl-ex].

[21] ***Nupecc long range plan 2017 - perspectives in nuclear physics*** (2016), http://www.nupecc.org/lrp2016/Documents/lrp2017.pdf.

[22] J. Cleymans, "Status of the Thermal Model and Chemical Freeze-Out", EPJ Web Conf. **95**, 03004 (2015) 10.1051/epjconf/20159503004, arXiv:1412.7045 [hep-ph].

[23] M. L. Miller et al., "Glauber modeling in high energy nuclear collisions", Ann. Rev. Nucl. Part. Sci. **57**, 205 (2007) 10.1146/annurev.nucl.57.090506.123020, arXiv:nucl-ex/0701025 [nucl-ex].

[24] K. J. Eskola, H. Paukkunen, and C. A. Salgado, "EPS09: A New Generation of NLO and LO Nuclear Parton Distribution Functions", JHEP **04**, 065 (2009) 10.1088/1126-6708/2009/04/065, arXiv:0902.4154 [hep-ph].

[25] S. Sarkar, H. Satz, and B. Sinha, "The physics of the quark-gluon plasma", Lect. Notes Phys. **785**, pp.1 (2010) 10.1007/978-3-642-02286-9.

[26] T. Matsui and H. Satz, "J/ψ Suppression by Quark-Gluon Plasma Formation", Phys. Lett. **B178**, 416 (1986) 10.1016/0370-2693(86)91404-8.

[27] J. J. Aubert et al., "Experimental Observation of a Heavy Particle J", Phys. Rev. Lett. **33**, 1404 (1974) 10.1103/PhysRevLett.33.1404, https://link.aps.org/doi/10.1103/PhysRevLett.33.1404.

[28] J.-E. Augustin et al., "Discovery of a Narrow Resonance in e^+e^- Annihilation", Phys. Rev. Lett. **33**, 1406 (1974) 10.1103/PhysRevLett.33.1406, https://link.aps.org/doi/10.1103/PhysRevLett.33.1406.

[29] H. Satz, "Charm and beauty in a hot environment", in Sense of Beauty in Physics: Miniconference in Honor of Adriano Di Giacomo on his 70th Birthday Pisa, Italy, January 26-27, 2006 (2006), arXiv:hep-ph/0602245 [hep-ph].

[30] S. Okubo, "Consequences of Quark Line (Okubo-Zweig-Iizuka) Rule", Phys. Rev. **D16**, 2336 (1977) 10.1103/PhysRevD.16.2336.

[31] A. Andronic et al., "Heavy-flavour and quarkonium production in the LHC era: from proton–proton to heavy-ion collisions", Eur. Phys. J. **C76**, 107 (2016) 10.1140/epjc/s10052-015-3819-5, arXiv:1506.03981 [nucl-ex].

[32] H. Satz, "Colour deconfinement and quarkonium binding", J. Phys. **G32**, R25 (2006) 10.1088/0954-3899/32/3/R01, arXiv:hep-ph/0512217 [hep-ph].

[33] R. Vogt, "Cold Nuclear Matter Effects on J/ψ and Υ Production at the LHC", Phys. Rev. **C81**, 044903 (2010) 10.1103/PhysRevC.81.044903, arXiv:1003.3497 [hep-ph].

[34] H. Fujii and K. Watanabe, "Heavy quark pair production in high energy pA collisions: Quarkonium", Nucl. Phys. **A915**, 1 (2013) 10.1016/j.nuclphysa.2013.06.011, arXiv:1304.2221 [hep-ph].

[35] R. Sharma and I. Vitev, "High transverse momentum quarkonium production and dissociation in heavy ion collisions", Phys. Rev. **C87**, 044905 (2013) 10.1103/PhysRevC.87.044905, arXiv:1203.0329 [hep-ph].

[36] J. W. Cronin et al., "Production of hadrons with large transverse momentum at 200, 300, and 400 GeV", Phys. Rev. **D11**, 3105 (1975) 10.1103/PhysRevD.11.3105.

[37] N. Armesto, A. Capella, and E. G. Ferreiro, "Charmonium suppression in lead-lead collisions: Is there a break in the J / psi cross-section?", Phys. Rev. **C59**, 395 (1999) 10.1103/PhysRevC.59.395, arXiv:hep-ph/9807258 [hep-ph].

[38] E. G. Ferreiro, "Excited charmonium suppression in proton–nucleus collisions as a consequence of comovers", Phys. Lett. **B749**, 98 (2015) 10.1016/j.physletb.2015.07.066, arXiv:1411.0549 [hep-ph].

[39] C. Lourenco, R. Vogt, and H. K. Woehri, "Energy dependence of J/ψ absorption in proton-nucleus collisions", JHEP **02**, 014 (2009) 10.1088/1126-6708/2009/02/014, arXiv:0901.3054 [hep-ph].

[40] B. Alessandro et al. (NA50 Collaboration), "J/psi and psi-prime production and their normal nuclear absorption in proton-nucleus collisions at 400-GeV", Eur. Phys. J. **C48**, 329 (2006) 10.1140/epjc/s10052-006-0079-4, arXiv:nucl-ex/0612012 [nucl-ex].

[41] ALICE Collaboration, "Preliminary Physics Summary: Transverse momentum and centrality dependence of inclusive J/ψ production in p-Pb collisions at $\sqrt{s_{\rm NN}} = 5.02$ TeV", (2018), https://cds.cern.ch/record/2317188.

[42] N. Brambilla et al., "Heavy quarkonium: progress, puzzles, and opportunities", Eur. Phys. J. **C71**, 1534 (2011) 10.1140/epjc/s10052-010-1534-9, arXiv:1010.5827 [hep-ph].

[43] A. Adare et al. (PHENIX Collaboration), "J/ψ suppression at forward rapidity in Au+Au collisions at $\sqrt{s_{NN}} = 200$ GeV", Phys. Rev. **C84**, 054912 (2011) 10.1103/PhysRevC.84.054912, arXiv:1103.6269 [nucl-ex].

[44] B. B. Abelev et al. (ALICE Collaboration), "Centrality, rapidity and transverse momentum dependence of J/ψ suppression in Pb-Pb collisions at $\sqrt{s_{\rm NN}}$=2.76 TeV", Phys. Lett. **B734**, 314 (2014) 10.1016/j.physletb.2014.05.064, arXiv:1311.0214 [nucl-ex].

[45] J. Book (ALICE Collaboration), "J/ψ production in Pb–Pb collisions at $\sqrt{s_{NN}} = 2.76$ TeV", Nucl. Phys. **A931**, 591 (2014) 10.1016/j.nuclphysa.2014.09.082.

[46] P. Braun-Munzinger and J. Stachel, "(Non)thermal aspects of charmonium production and a new look at J / ψ suppression", Phys. Lett. **B490**, 196 (2000) 10.1016/S0370-2693(00)00991-6, arXiv:nucl-th/0007059 [nucl-th].

[47] R. L. Thews, M. Schroedter, and J. Rafelski, "Enhanced J/ψ production in deconfined quark matter", Phys. Rev. **C63**, 054905 (2001) 10.1103/PhysRevC.63.054905, arXiv:hep-ph/0007323 [hep-ph].

[48] R. L. Thews, "Quarkonium formation at high-energy", Nucl. Phys. **A702**, 341 (2002) 10.1016/S0375-9474(02)00721-2, arXiv:hep-ph/0111015 [hep-ph].

[49] P. Braun-Munzinger, I. Heppe, and J. Stachel, "Chemical equilibration in Pb + Pb collisions at the SPS", Phys. Lett. **B465**, 15 (1999) 10.1016/S0370-2693(99)01076-X, arXiv:nucl-th/9903010 [nucl-th].

[50] A. Andronic et al., "The statistical model in Pb-Pb collisions at the LHC", Nucl. Phys. **A904-905**, 535c (2013) 10.1016/j.nuclphysa.2013.02.070, arXiv:1210.7724 [nucl-th].

[51] P. Braun-Munzinger and J. Stachel, "On charm production near the phase boundary", Nucl. Phys. **A690**, 119 (2001) 10.1016/S0375-9474(01)00936-8, arXiv:nucl-th/0012064 [nucl-th].

[52] A. Andronic et al., "Transverse momentum distributions of charmonium states with the statistical hadronization model", (2019), arXiv:1901.09200 [nucl-th].

[53] X. Zhao and R. Rapp, "Charmonium in Medium: From Correlators to Experiment", Phys. Rev. **C82**, 064905 (2010) 10.1103/PhysRevC.82.064905, arXiv:1008.5328 [hep-ph].

[54] X. Zhao and R. Rapp, "Medium Modifications and Production of Charmonia at LHC", Nucl. Phys. **A859**, 114 (2011) 10.1016/j.nuclphysa.2011.05.001, arXiv:1102.2194 [hep-ph].

[55] K. Zhou et al., "Medium effects on charmonium production at ultrarelativistic energies available at the CERN Large Hadron Collider", Phys. Rev. **C89**, 054911 (2014) 10.1103/PhysRevC.89.054911, arXiv:1401.5845 [nucl-th].

[56] E. G. Ferreiro, "Charmonium dissociation and recombination at LHC: Revisiting comovers", Phys. Lett. **B731**, 57 (2014) 10.1016/j.physletb.2014.02.011, arXiv:1210.3209 [hep-ph].

[57] J. Adam et al. (ALICE Collaboration), "J/ψ suppression at forward rapidity in Pb-Pb collisions at $\sqrt{\mathbf{s_{NN}}} = \mathbf{5.02}$ TeV", Phys. Lett. **B766**, 212 (2017) 10.1016/j.physletb.2016.12.064, arXiv:1606.08197 [nucl-ex].

[58] M. K. Köhler (ALICE Collaboration), "Quarkonium production in Pb–Pb and Xe–Xe collisions with ALICE at the LHC", in 9th International Conference on Hard and Electromagnetic Probes of High-Energy Nuclear Collisions: Hard Probes 2018 (HP2018) Aix-Les-Bains, Savoie, France, October 1-5, 2018 (2018), arXiv:1811.10881 [nucl-ex].

[59] S. Acharya et al. (ALICE Collaboration), "Inclusive J/ψ production in Xe–Xe collisions at $\sqrt{s_{\rm NN}} = 5.44$ TeV", Phys. Lett. **B785**, 419 (2018) 10.1016/j.physletb.2018.08.047, arXiv:1805.04383 [nucl-ex].

[60] P. Dillenseger (ALICE Collaboration), "Quarkonium measurements in nucleus–nucleus collisions with ALICE", Nucl. Phys. **A982**, 703 (2019) 10.1016/j.nuclphysa.2018.09.024, arXiv:1807.07757 [hep-ex].

[61] H. Hushnud for the ALICE Collaboration, "Multi-differential study of J/ψ yield at forward rapidity in Pb-Pb collisions at $\sqrt{s_{\mathrm{NN}}}$ = 5.02 TeV with ALICE", Poster Quark Matter Conference 2018 (2018), https://indico.cern.ch/event/656452/contributions/2859764/.

[62] E. Mobs, "The CERN accelerator complex - August 2018. Complexe des accélérateurs du CERN - Août 2018", General Photo (2018), http://cds.cern.ch/record/2636343.

[63] L. R. Evans and P. Bryant, "LHC Machine", JINST **3**, This report is an abridged version of the LHC Design Report (CERN-2004-003), S08001. 164 p (2008), http://cds.cern.ch/record/1129806.

[64] R. Vogt, ***Ultrarelativistic heavy-ion collisions*** (Elsevier, Amsterdam, 2007).

[65] K. Aamodt et al. (ALICE Collaboration), "The ALICE experiment at the CERN LHC", JINST **3**, S08002 (2008) 10.1088/1748-0221/3/08/S08002.

[66] B. B. Abelev et al. (ALICE Collaboration), "Performance of the ALICE Experiment at the CERN LHC", Int. J. Mod. Phys. **A29**, 1430044 (2014) 10.1142/S0217751X14300440, arXiv:1402.4476 [nucl-ex].

[67] A. Tauro, "ALICE detector schematic after LS2", Jan. 2017, https://cds.cern.ch/record/2242939.

[68] Y. Belikov et al., "TPC tracking and particle identification in high density environment", eConf **C0303241**, TULT011 (2003), arXiv:physics/0306108 [physics].

[69] A. Maire and D. Dobrigkeit Chinellato, "ALICE sub-detectors highlighted (LHC runs 1+2 // runs 3+4)", General Photo, May 2017, https://cds.cern.ch/record/2302924.

[70] J. Alme et al., "The ALICE TPC, a large 3-dimensional tracking device with fast readout for ultra-high multiplicity events", Nucl. Instrum. Meth. **A622**, 316 (2010) 10.1016/j.nima.2010.04.042, arXiv:1001.1950 [physics.ins-det].

[71] U. Fano, "Penetration of protons, alpha particles, and mesons", Annual Review of Nuclear Science **13**, 1 (1963) 10.1146/annurev.ns.13.120163.000245, eprint: https://doi.org/10.1146/annurev.ns.13.120163.000245, https://doi.org/10.1146/annurev.ns.13.120163.000245.

[72] M. Kleiner, "Integration kosmischer myonen in die parametrisierung des spezifischen energieverlustes für die alice spurendriftkammer", MA thesis (Goethe-University, 2019).

[73] E. Botta (ALICE Collaboration), "Particle identification performance at ALICE", in 5th Large Hadron Collider Physics Conference (LHCP 2017) Shanghai, China, May 15-20, 2017 (2017), arXiv:1709.00288 [nucl-ex].

[74] M. L. Cherry et al., "Transition radiation from relativistic electrons in periodic radiators", Phys. Rev. **D10**, 3594 (1974) 10.1103/PhysRevD.10.3594.

[75] S. Acharya et al. (ALICE Collaboration), "The alice transition radiation detector: construction, operation, and performance", Nucl. Instrum. Meth. **A881**, 88 (2018) 10.1016/j.nima.2017.09.028, arXiv:1709.02743 [physics.ins-det].

[76] A. Akindinov et al., "Performance of the ALICE Time-Of-Flight detector at the LHC", Eur. Phys. J. Plus **128**, 44 (2013) 10.1140/epjp/i2013-13044-x.

[77] B. Abelev et al. (ALICE Collaboration), "Centrality determination of Pb−Pb collisions at $\sqrt{s_{\rm NN}} = 2.76$ TeV with ALICE", Phys. Rev. **C88**, 044909 (2013) 10.1103/PhysRevC.88.044909, arXiv:1301.4361 [nucl-ex].

[78] J. Adam et al. (ALICE Collaboration), "Centrality dependence of the charged-particle multiplicity density at midrapidity in Pb−Pb collisions at $\sqrt{s_{\rm NN}} = 5.02$ TeV", Phys. Rev. Lett. **116**, 222302 (2016) 10.1103/PhysRevLett.116.222302, arXiv:1512.06104 [nucl-ex].

[79] I. Antcheva et al., "ROOT: A C++ framework for petabyte data storage, statistical analysis and visualization", Comput. Phys. Commun. **180**, 2499 (2009) 10.1016/j.cpc.2009.08.005, arXiv:1508.07749 [physics.data-an].

[80] R. Brun and F. Rademakers, "ROOT: An object oriented data analysis framework", Nucl. Instrum. Meth. **A389**, 81 (1997) 10.1016/S0168-9002(97)00048-X.

[81] I. Bird, "Computing for the Large Hadron Collider", Ann. Rev. Nucl. Part. Sci. **61**, 99 (2011) 10.1146/annurev-nucl-102010-130059.

[82] S. Bagnasco et al., "AliEn: ALICE environment on the GRID", Journal of Physics: Conference Series **119**, 062012 (2008) 10.1088/1742-6596/119/6/062012, https://doi.org/10.1088%2F1742-6596%2F119%2F6%2F062012.

[83] ***ALICE analysis tutorial*** (May 2019), https://alice-doc.github.io/alice-analysis-tutorial/.

[84] M. Zimmermann (ALICE Collaboration), "The ALICE analysis train system", J. Phys. Conf. Ser. **608**, 012019 (2015) 10.1088/1742-6596/608/1/012019, arXiv:1502.06381 [hep-ex].

[85] ***Pro git book*** (May 2019), https://git-scm.com/book/en/v2.

[86] ***Dielectron framework*** (May 2019), https://github.com/alisw/AliPhysics/tree/master/PWGDQ/dielectron.

[87] J. Jowett et al., "The 2015 Heavy-Ion Run of the LHC", in Proceedings, 7th International Particle Accelerator Conference (IPAC 2016): Busan, Korea, May 8-13, 2016 (2016), TUPMW027, 10.18429/JACoW-IPAC2016-TUPMW027.

[88] E. Kryshen, "Luminosity determination for ultra-peripheral triggers in Pb-Pb at $\sqrt{s_{\rm NN}} = 5.02$ TeV ", ALICE analysis note, Jan. 2017.

[89] "Centrality determination in heavy ion collisions", (2018), http://cds.cern.ch/record/2636623.

[90] S. A. Bass et al., "Microscopic models for ultrarelativistic heavy ion collisions", Prog. Part. Nucl. Phys. **41**, [Prog. Part. Nucl. Phys.41,225(1998)], 255 (1998) 10.1016/S0146-6410(98)00058-1, arXiv:nucl-th/9803035 [nucl-th].

[91] M. Bleicher et al., "Relativistic hadron hadron collisions in the ultrarelativistic quantum molecular dynamics model", J. Phys. **G25**, 1859 (1999) 10.1088/0954-3899/25/9/308, arXiv:hep-ph/9909407 [hep-ph].

[92] M. Bleicher, https://urqmd.org/.

[93] R. Snellings, "Elliptic Flow: A Brief Review", New J. Phys. **13**, 055008 (2011) 10.1088/1367-2630/13/5/055008, arXiv:1102.3010 [nucl-ex].

[94] P. F. Kolb and U. W. Heinz, "Hydrodynamic description of ultrarelativistic heavy ion collisions", 634 (2003), arXiv:nucl-th/0305084 [nucl-th].

[95] I. Selyuzhenkov and S. Voloshin, "Effects of non-uniform acceptance in anisotropic flow measurement", Phys. Rev. **C77**, 034904 (2008) 10.1103/PhysRevC.77.034904, arXiv:0707.4672 [nucl-th].

[96] A. M. Poskanzer and S. A. Voloshin, "Methods for analyzing anisotropic flow in relativistic nuclear collisions", Phys. Rev. **C58**, 1671 (1998) 10.1103/PhysRevC.58.1671, arXiv:nucl-ex/9805001 [nucl-ex].

[97] A. Dubla (ALICE Collaboration), "Heavy-flavour hadron decay leptons in Pb-Pb and Xe-Xe collisions at the LHC with ALICE", Nucl. Phys. **A982**, 651 (2019) 10.1016/j.nuclphysa.2018.09.038, arXiv:1807.05382 [hep-ex].

[98] D. Weiser, "Inclusive J/ψ production at mid-rapidity in pp and Pb−Pb collisions with ALICE", PhD thesis (University Heidelberg, 10.11588/heidok.00026115, 2019).

[99] P. Crochet and P. Braun-Munzinger, "Investigation of background subtraction techniques for high mass dilepton physics", Nucl. Instrum. Meth. **A484**, 564 (2002) 10.1016/S0168-9002(01)02005-8, arXiv:nucl-ex/0106008 [nucl-ex].

[100] Jiménez Bustamante, Raúl Tonatiuh, "Inclusive J/ψ production at mid-rapidity in Pb−Pb collisions at $\sqrt{s_{\mathrm{NN}}} = 5.02$ TeV", PhD thesis (University Heidelberg, 10.11588/heidok.00025121, 2018).

[101] J. Adam et al. (ALICE Collaboration), "Anisotropic flow of charged particles in Pb−Pb collisions at $\sqrt{s_{\mathrm{NN}}} = 5.02$ TeV", Phys. Rev. Lett. **116**, 132302 (2016) 10.1103/PhysRevLett.116.132302, arXiv:1602.01119 [nucl-ex].

[102] S. Voloshin and Y. Zhang, "Flow study in relativistic nuclear collisions by Fourier expansion of Azimuthal particle distributions", Z. Phys. **C70**, 665 (1996) 10.1007/s002880050141, arXiv:hep-ph/9407282 [hep-ph].

[103] S. A. Voloshin, A. M. Poskanzer, and R. Snellings, "Collective phenomena in non-central nuclear collisions", Landolt-Bornstein **23**, 293 (2010) 10.1007/978-3-642-01539-7_10, arXiv:0809.2949 [nucl-ex].

[104] N. Borghini and J. Y. Ollitrault, "Azimuthally sensitive correlations in nucleus-nucleus collisions", Phys. Rev. **C70**, 064905 (2004) 10.1103/PhysRevC.70.064905, arXiv:nucl-th/0407041 [nucl-th].

[105] R. Barlow, "Systematic errors: Facts and fictions", in Advanced Statistical Techniques in Particle Physics. Proceedings, Conference, Durham, UK, March 18-22, 2002 (2002), pp. 134–144, arXiv:hep-ex/0207026 [hep-ex], http://www.ippp.dur.ac.uk/Workshops/02/statistics/proceedings//barlow.pdf.

[106] S. Acharya et al. (ALICE Collaboration), "J/ψ elliptic flow in Pb-Pb collisions at $\sqrt{s_{\rm NN}} = 5.02$ TeV", Phys. Rev. Lett. **119**, 242301 (2017) 10.1103/PhysRevLett.119.242301, arXiv:1709.05260 [nucl-ex].

[107] S. Acharya et al. (ALICE Collaboration), "D-meson azimuthal anisotropy in midcentral Pb-Pb collisions at $\sqrt{\mathbf{s}_{\rm NN}} = \mathbf{5.02}$ TeV", Phys. Rev. Lett. **120**, 102301 (2018) 10.1103/PhysRevLett.120.102301, arXiv:1707.01005 [nucl-ex].

[108] S. Acharya et al. (ALICE Collaboration), "Search for collectivity with azimuthal J/ψ-hadron correlations in high multiplicity p-Pb collisions at $\sqrt{s_{\rm NN}}$ = 5.02 and 8.16 TeV", Phys. Lett. **B780**, 7 (2018) 10.1016/j.physletb.2018.02.039, arXiv:1709.06807 [nucl-ex].

[109] B. B. Abelev et al. (ALICE Collaboration), "Long-range angular correlations of π, K and p in p-Pb collisions at $\sqrt{s_{\rm NN}} = 5.02$ TeV", Phys. Lett. **B726**, 164 (2013) 10.1016/j.physletb.2013.08.024, arXiv:1307.3237 [nucl-ex].

[110] S. Acharya et al. (ALICE Collaboration), "Inclusive J/ψ production at midrapidity in pp collisions at $\sqrt{s} = 5.02$ TeV", (2019), arXiv:1905.07211 [nucl-ex].

[111] P. P. Bhaduri, M. Deveaux, and A. Toia, "Charmonium interaction in nuclear matter at FAIR", J. Phys. **G45**, 055103 (2018) 10.1088/1361-6471/aab27e, arXiv:1712.05951 [hep-ph].

[112] J. Steinheimer, A. Botvina, and M. Bleicher, "Sub-threshold charm production in nuclear collisions", Phys. Rev. **C95**, 014911 (2017) 10.1103/PhysRevC.95.014911, arXiv:1605.03439 [nucl-th].

[113] R. J. Barlow, "Practical Statistics for Particle Physics", (2019), arXiv:1905.12362 [physics.data-an].

[114] O. Behnke et al., eds., ***Data analysis in high energy physics*** (Wiley-VCH, Weinheim, Germany, 2013), http://www.wiley-vch.de/publish/dt/books/ISBN3-527-41058-9.

[115] S. I. Bityukov, "Signal significance in the presence of systematic and statistical uncertainties", JHEP **09**, [Nucl. Instrum. Meth.A502,795(2003)], 060 (2002) 10.1088/1126-6708/2002/09/060,10.1016/S0168-9002(03)00586-2, arXiv:hep-ph/0207130 [hep-ph].

[116] P. Vischia, "Pseudosignificances as figures of merit: a systematic study and exploration of Bayesian solutions", PoS **Confinement2018**, 249 (2019) 10.22323/1.336.0249.